UNIVERSITÄT FÜR BODENKULTUR WIEN

Department für Bautechnik und Naturgefahren
Institut für Geotechnik

Dissertation

Hypoplastic constitutive model for debris materials

Xiaogang Guo
October 2012 - September 2016

UNIVERSITÄT FÜR BODENKULTUR WIEN

Institut für Geotechnik

Definition of tasks

Studiengang:	Kulturtechnik und Wasserwirtschaft
Name des Studenten:	Xiaogang Guo

Hypoplastic constitutive model for debris materials

Tasks:

This project aims to develop advanced constitutive model of debris flow for better understanding of the triggering mechanisms, reliable prediction of runout dynamics and rational design of mitigation and protection structures. Debris materials involve solid particles and interstitial fluid, which show solid-like and fluid-like behavior before and after yielding respectively. A constitutive model will be developed covering the solid-like and fluid-like behavior and considering the major factors like plasticity, density, dilatancy and viscosity. Hypoplasticity will be employed for the describing of solid-like behavior of debris materials and combined with rheology to obtain a complete model.

Universität für Bodenkultur Wien
Institut für Geotechnik

Erklärung zur Dissertation

Ich, Xiaogang Guo, bestätige hiermit, dass ich die beiliegende Dissertation selbstständig verfasst habe. Ebenso bestätige ich, dass keine anderen als die angegebenen Quellen und Hilfsmittel benutzt wurden.

Wien, September 2016

Declaration of dissertation

I, Xiaogang Guo, hereby confirm, that I write the enclosed dissertation all by myself. I also confirm, that nothing more than the given sources and auxiliary materials are used.

Vienna, September 2016

Acknowledgment

I would like to express my gratitude to all those who helped me during my PhD studying and the writing of this thesis.

My deepest gratitude goes first and foremost to Prof. Wei Wu, my supervisor, for his constant encouragement and guidance. Without his instructive advice and useful suggestions, this thesis could not have reached its present form.

Second, I would like to express my heartfelt gratitude to Dr. Chong Peng, who gave me invaluable help in the numerical simulations. Our discussions have been inspiring.

I am also greatly indebted to Prof. Yongqi Wang, who helped me a lot during the one-year visit in TU Darmstadt. I also owe a debt of gratitude to all the members in the Institute of Geotechnical Engineering of BOKU and all the supervisors, experienced researchers and early stage researchers in MuMoLaDe project for their direct and indirect help.

Special thanks should go to my family for their selfless love which encouraged me to complete my PhD study.

Finally, I would like to thank the EU Marie Curie actions ITN for the funding , which support my research work for three years.

Abstract

Debris flow is a very common natural hazard that represents the gravity-driven flow of a mixture of various sizes of sediment, water and air, down a steep slope, often initiated by heavy rainfall or snow melting. The mud carrying large items, such as boulders and trees, rushes out the channel and accumulates in a thick deposit that can wreak havoc in developed areas and cause serious casualties and property losses. In order to avoid or mitigate such catastrophic events, research on the initiation mechanism and flow characteristics of debris materials is required. There are mainly two directions about research of debris flows. The first one is focusing on the macroscopic characteristics of debris flows to establish some empirical relationships based on the statistics of a large number of debris flow events. The second direction of debris flow research is focused on the material property and trying to develop more sophisticated constitutive model for numerical simulations. This thesis follows the second direction, which requires better understanding of the initiation and flowing mechanisms of debris flows.

The main factors influencing the initiation of debris flow are, among others, the topography, material properties, water and the initial stress state in the affected slope. Upon initiation of debris flow, debris material shows fluid-like behavior. In these processes, the development of high pore water pressure is regarded as the most significant triggering factor. The water from heavy rainfall or snow melting triggers an upland landslide which may develop into a hillside debris flow when the water in the sliding mass cannot be drained quickly and therefore gives rise to excessive pore water pressure. In addition, excess pore water is also observed during the period of runout and depositing. Numerical simulation is an important tool in the analyses of triggering and runnout distance of debris flows. In the simulations, a competent constitutive model is required to capture the transition between the solid-like and fluid-like behaviors and to describe the pore water pressure (or effective stresses) in the initiation stage and flowing stage.

In the constitutive modelling, debris materials are normally simplified as a mixture of solid spherical particle and viscous fluid and treated as continuum with microstructure. In most conventional models, constitutive equations for the static and dynamic regimes are formulated and applied separately. Although some models for granular-fluid flows take the stress state of the quasi-static stage into account, the employed theories for the static regime still fail to determine the evolving of pore water pressure (or effective stress) from the deformation directly. Effective stress is a concept from soil mechanics in which the constitutive theories for the static regimes of saturated granular materials are well established. Hypoplasticity is one of them, which was originally proposed as an alternative to plasticity for describing the solid-like behavior of granular materials. Effective stress can be directly determined from deformation by hypoplastic models.

In this thesis, we combine the rate-independent constitutive theories of statics and the rate-dependent dynamic theories to develop a unified and multi-scale constitutive model for debris materials. A framework which consists of a static portion for the frictional behavior and a dynamic portion for the viscous behavior is proposed. Bagnold's constitutive theory was then slightly modified and employed as the dynamic portion of the framework. The Mohr-Coulomb criterion is used as the static portion and combined with the modified Bagnold's model to obtain a complete model for simple-shearing. This model is further extended to a three-dimensional constitutive model for granular-fluid flows. Simulations of two annular shear tests verified the capability of the modified Bagnold's model to predict the stress state in the flowing stage and brought out the shortcoming of the Mohr-Coulomb criterion to capture liquefaction in the initiation stage. Then, the applicability of a specific hypoplastic model for describing the quasi-static state of granular-fluid flows is shown by simulating undrained simple shear test of saturated granular materials. A concrete constitutive model for debris materials is obtained by using the hypoplastic model to replace the Mohr-Coulomb criterion in the unified model. In the simulations of the annular shear tests, partial and full liquefaction of the specimens with different densities are well predicted by the hypoplastic portion. The predicted stress-strain curves agree well with the experimental data. Finally, the unified model is implemented in a Smoothed Particle Hydrodynamics (SPH) code and verified by simulating some boundary value problems of granular flows. In the case of granular flow down an inclined plane, steady dense granular flow is observed over a range of inclinations, which is consistent with the theoretical analysis. For the granular pile collapse and the granular flow in the rotating drum, the numerical results show wealth of various behaviors, i.e. quasi-static motion, shear band, flow initiation, fully developed granular flow and granular deposition. The implementation of the unified model in SPH is promising to handle the complex behavior of granular flow in a consistent numerical model. It should be noted that all the numerical simulations by SPH in this thesis are focused on dry granular flows. Since some aspects, such as hydro-mechanical coupling and particle segregation, still need further investigation to be considered in the numerical and constitutive model, applying the unified model to the numerical simulation of debris flow in nature is an interesting challenge in our future work.

Contents

Definiteion of tasks **2**

1 Introduction **1**

1.1 Background 1

1.2 Contents 4

2 The constitutive model for granular-fluid flows **5**

2.1 Bagnold's theory 5

2.2 A constitutive framework for granular-fluid flows 7

2.3 A constitutive model for granular-fluid flows 10

2.3.1 Constitutive relation for the quasi-static state 11

2.3.2 Constitutive relations for the flowing state 12

2.3.3 The three-dimensional form of the simple-shearing model 16

2.4 Performance of the proposed model 17

2.4.1 Dry granular materials 17

2.4.2 Granular-water mixture 19

3 Hypoplastic constitutive model for debirs flows **23**

3.1 Introduction of hypoplasticity 23

3.2 The applicability of hypoplastic models for debris materials 27

3.3 The new constitutive model for debris materials 33

3.4 Performance of the proposed model 36

3.4.1 Dry granular materials 36

3.4.2 Granular-water mixture 38

4 Verification of the new model by smoothed particle hydrodynamics method **42**

4.1 Introduction of SPH method 42

4.2 SPH modelling of granular material 44

4.2.1 The governing equations 45

4.2.2 The SPH formulations 45

4.2.3 The correction of kernel gradient 48

4.2.4 Numerical implementation and boundary conditions 50

4.3 SPH element tests 50

4.3.1 Quasi-static undrained simple shear test 51

4.3.2 Granular sheared in an annular shear cell 52

4.4 Application to boundary value problems 55

4.4.1 Granular flow on an incline 55

4.4.2 Collapse of a granular pile 60

4.4.3 Granular flow in a rotating drum 62

5 Conclusions and outlook **67**

5.1 Conclusion 67

5.2 Outlook 70

Bibliography **79**

List of Figures

2.1 The schematic of a simple shear test. 5

2.2 The result predicted by (2.7) for Bagnold's experimental data of $\lambda = 11$ [5]. . 8

2.3 The schematic of an uniform granular-fluid flow on a slope. 9

2.4 The schematic of a simple shearing granular-fluid flow with a stagnant zone beneath the flowing zone 13

2.5 The predicted curves by (2.40) and (2.41) with $n = 0.2$ for the data from (a) the figure 3 and (b) the figure 4 in [5]. The experimental data are indicated by various symbols. The dashed lines (upper panel) denote the shear stress while the solid lines (lower panel) for the normal stress. 20

2.6 Element test results for the dry granular flow with different solid volume fraction: (a) nondimensional shear rate vs normal stress (b) nondimensional shear rate vs shear stress. The experimental data are indicated by various symbols. The dashed lines (upper panel) denote the normal stress while the solid lines (lower panel) for the shear stress. 21

2.7 Element test results for the granular-water flow with different solid volume fraction: (a) normal stress (b) shear stress. The experimental data are indicated by various symbols. The solid lines denote the normal stress in the upper panel and the shear stress in the lower panel. 22

3.1 Failure surface and flow rule derived from the constitutive equation (3.11): (a) failure surface; (b) flow rule on the π-plane. 28

3.2 Three types of stress-strain behavior observed in undrained triaxial tests and undrained simple shear tests: (a) shear strain vs shear stress (b) mean principal stress vs shear stress. The shear stress q is equal to the difference between the first and the second principal stress. p' is the mean value of the first and the second principal stress. 31

3.3 The simulation results of (3.16) for saturated sand with different initial void ratio in undrained simple shear tests: (a) shear strain vs shear stress (b) mean principal stress vs shear stress 32

3.4 The normal stresses of the specimens with $e = 0.876$ in the undrained simple shear tests with different initial stress state: (a) $\sigma_{11} = \sigma_{22} = \sigma_{33} = 100kPa$, (b) $\sigma_{22} = 100kPa$ and $\sigma_{11} = \sigma_{33} = 1kPa$ 34

3.5 Schematics of the new model (3.24): (a) shear rate vs normal stress (b) shear rate vs shear stress 35

3.6 Element test results for the dry granular flow with different grain linear concentration: (a) shear rate vs normal stress (b) shear rate vs shear stress. The experimental data are indicated by various symbols. The dashed lines denote the normal stresses while the solid lines for the shear stresses. 39

3.7 Element test results for the granular-water flows with different solid volume fraction: (a) shear rate vs normal stress (b) shear rate vs shear stress. The experimental data are indicated by various symbols. The solid lines denote the shear stresses and the dashed lines are the normal stresses. 41

4.1 Computational setup for the undrained simple shear test. Granular particles and boundary particles are marked blue and gray. 51

4.2 Simple shear tests with different initial void ratios:(a) shear strain vs shear stress, (b) mean principal stress vs shear stress. 52

4.3 Dry granular flow with different solid volume fraction: shear rate vs. shear stress. The markers denote experimental data from [74]. 54

4.4 Dry granular flow with different solid volume fraction: shear rate vs. normal stress. The markers denote experimental data from [74]. 54

4.5 Sketch-up of a granular flow on an inclined plate. 55

4.6 Numerical setups for the simulation of steady granular flow. The color scale represents the velocity field in $\theta = 26°$. 57

4.7 Velocity profiles: lines indicate reference solutions calculated from Eq. (4.35) and markers are numerical results. 58

4.8 Normalized analytical and numerical frictional contact (hypoplastic) stress. Normal stress is in the left (negative part) and shear stress in the right (positive part). 59

4.9 Normalized analytical and numerical collisional stress. Normal stress is in the left (negative part) and shear stress in the right (positive part). 59

4.10 Initial geometry and boundary conditions. 60
4.11 The collapse process of the granular pile. The figures are coloured by equivalent viscosity η. 60
4.12 Change in percentage of dynamic stress part in the total stress at three particles. 61
4.13 Evolution of runout distance. 62
4.14 Stress distributions in the final state. 63
4.15 Numerical setups for the simulation of granular in a rotating drum: (a) initial state; (b) steady flow state. 63
4.16 The developing process of steady surface flow in the rotating drum, $\omega = 1.0$ s^{-1}. 64
4.17 Evolution of maximum surface velocity. 64
4.18 Velocity profiles in the flowing layer. 65
4.19 Quasi-static and flowing regions in the drum: (a) $\omega = 0.5$ s^{-1}; (b) $\omega = 1.0$ s^{-1}; (c) $\omega = 2.0$ s^{-1}. The figures are coloured by the apparent viscosity η. . . 66

List of Tables

2.1 Parameters for the shear tests of 1.0 mm beads in [74] 18

2.2 Stress ratios measured in the shear tests of 1.0 mm beads in [74] 18

2.3 Parameters for the shear tests of 1.85 mm beads in [34] 19

2.4 Stress ratios measured in the shear tests of 1.85 mm beads in [34] 19

3.1 Material constants for the model (3.16) in the simulation of the undrained simple shear tests in [101] 30

3.2 Parameters for e_{crt} and a in the simulation of the experiments in [101] 33

3.3 Parameters for the static portion in the simulation of dry granular flows 37

3.4 Parameters for the dynamic portion in the simulation of dry granular flows . . 37

3.5 The residual stresses of the four samples of dry granular flow determined by the hypoplastic model 38

3.6 Parameters for the static portion in the simulation of granular-fluid flows . . . 40

3.7 Parameters for the dynamic portion in the simulation of granular-fluid flows . 40

3.8 The residual stresses of the two samples of ganular-fluid flow determined by the hypoplastic model 41

4.1 List of solid volume fraction C, void ratio e, residual stresses and viscous coefficient K_2 in the four simulations. 53

4.2 Material parameters for the granular on a inclined plate. 58

4.3 Summary of the numerical modelling of rotating drum. 65

Chapter 1

Introduction

1.1 Background

Debris flow is a very common natural hazard in mountainous areas of many countries. It represents the gravity-driven flow of a mixture of various sizes of sediment, water and air, down a steep slope, often initiated by heavy rainfall and landslides [37]. In the general concept of landslides, debris flows including mudflows, mudslides and debris avalanches are classified as high-speed landslides which are destructive due to the great kinetic energy. A typical debris flow usually starts in a hillslope depression where loose debris materials are stored, and retains a scar there after the event. The debris then flows down along an existing stream channel like a viscous fluid and is accelerated to a high speed. The velocity of debris flows can be more than 30 m/s; however, typical velocities are less than 10 m/s [59]. Its volume may grow with significant erosion or combination of debris flows from different sources. When the flow reaches the canyon mouth or a flatter ground, the debris spreads over a broad area to form a fan-shaped deposit. In mountainous areas, people are willing to settle down close to rivers or torrents because these areas are more favorable to urban development. However, these areas are more likely to suffer from debris flows. The mud carrying large items, such as boulders and trees, rushes out the channel and accumulates in a thick deposit that can wreak havoc in developed areas and cause serious casualties and property losses. In recent years, a lot of catastrophic debris flows were registered worldwide. For example, the Zhouqu debris flow on August 7th, 2010, in China destroyed the the Zhouqu County town with a total volume of almost $144.2 \times 10^4 m^3$ and resulted in over 1700 casualties [102]; a series of debris flows took place in the mountainous region of Rio de Janeiro State on January 11th and 12th, 2011, and caused more than 1500 deaths and severe damage to the local infrastructure [4].

In order to avoid or mitigate such catastrophic events, preventive measures need to be taken in the threatened areas. At the same time, research on the initiation mechanism and flow characteristics of debris materials is required for the design of the preventive measures. There are mainly two directions about the research of debris flows. The first one foucses on the macroscopic characteristics of debris flows to establish some empirical relationships based on the statistics of a large number of debris flows, such as the relation between the maximum debris-flow volume and the peak discharge, the mean flow velocity or the runout distance [69], the relation between the triggering of debris flows and the rainfall intensity and duration [91]. These relationships are widely used in practice since numerical methods are not widely used. Thus, the second direction of debris flow research is focusing on the material property and trying to develop more sophisticated constitutive model for numerical simulations. The study in this thesis is along the second direction, which requires deep understanding of initiation and flowing mechanisms of debris flows.

The main factors influencing the initiation of debris flow are, among others, the topography, material parameters, water and the initial stress state in the affected slope [46]. Earth slopes with inclinations ranging from 26° to 45° have been generally identified as most prone to debris flow initiation [91]. The common solid volume fraction of debris materials, defined as the ratio between the solid volume and the total volume of a representative volume element, varies between 30 and 65%. The water from heavy rainfall or snow melting makes the unconsolidated superficial deposit on a steep hillside saturated, which may give rise to reduced shear strength to trigger landslide. Such an upland landslide may develop into hillside debris flow when the water in the sliding mass cannot be drained quickly and therefore gives rise to excessive pore water pressure. In this case, the effective stresses between solid particles will decrease to cause reduction or complete loss of shear strength. Upon initiation of debris flow, debris material shows fluid-like behavior. According to Iverson [41], debris flow can be mobilized by three processes: (i) widespread Coulomb failure along a rupture surface within a saturated soil or sediment mass, (ii) partial or complete liquefaction of a sliding mass due to high pore-fluid pressure, and (iii) conversion of landslide translational energy to internal vibrational energy. In these processes, the development of high pore water pressure is regarded as the most significant triggering factor. In addition, experimental observation [39] shows that an almost constant excess pore water pressure persists during the period of runout and deposition of debris flows. Because of the characteristics of large scale, it is difficult and non-economical to simulate a debris flow with specific terrain and material through physical model tests. Therefore, numerical simulation is often used to analyses the triggering and runnout distance, in which a competent constitutive model is required. As introduced before, debris materials show solid-like behaviors before failure and fluid-like behaviors after failure. A constitutive model which can capture the transition between the solid-like and fluid-like behaviors should has the capability to describe the developing of pore water pressure (or effective stresses) in the initiation stage and flowing stage.

Actually, debris materials are normally simplified as a mixture of solid spherical particle-viscous fluid and treated as a fluid continuum with microstructural effect in the constitutive modelling [24, 25]. Some important material parameters such as solid volume fraction (or void ratio in soil mechanics) and the internal friction coefficient are taken into account. In most conventional models, constitutive equations for the static and dynamic regimes are formulated and applied separately, such as the models for the solid-like behaviors of granular materials [94, 95, 62, 17], and that for the fluid-like behaviors [11, 5, 43]. Although some models for granular-fluid flows have taken the stress state of the quasi-static stage into account, the employed theories for the static regime, such as Mohr-Coulomb criterion [75] and extended von Mises yield criterion [71], fail to determine the evolving of pore water pressure from the deformation directly. Generally, there are three approaches in modelling of granular flows. The first one is that granular flow can be regarded as viscous fluid with an apparent viscosity related to shear rate and material parameters, such as the models developed by Bagnold [5] and Jenkins & Savage [43]. The second idea is that the generalized Coulomb friction law is considered to be satisfied in the entire process from quasi-static state to flowing state of a granular flow, which means the shear stress is proportional to the normal stress with a dynamic friction coefficient that is a function of the confining pressure and shear rate rather than a constant. Typical models based on this idea are the one developed for dry dense granular flows by Jop et al. [45] and the one for granular-fluid flows [13] which is extended from Jop's model. The third notion about constitutive modelling of granular flows is similar with the second one where friction law is always satisfied. In the third one, however, the friction coefficient is regarded as constant while the effective part of the normal stress is considered, which is changing with the evolving of pore-fluid pressure. The details of this idea and the relative hydraulic models are well introduced in the literature [37, 38, 40, 73]. The models based on the last two ideas are normally complete model which can fulfill the description of the stress state in the entire flow process. However, additional theories, such as Darcy' law, are required to capture the evolving of pore-fluid pressure and further determine the solid-solid contact stress (or effective stress) in a granular-fluid flow. Effective stress is a concept from soil mechanics in which the constitutive theories for the static regimes of saturated granular materials are well established. Hypoplasticity is one of the latest constitutive theories, which was originally proposed as an alternative to plasticity for describing the solid-like behavior of granular materials [94, 95]. The distinctive features of hypoplasticity are its simple formulation and capacity to capture some salient features of granular materials, such as nonlinearity, dilatancy and yielding [93]. Effective stress can be directly determined from deformation by hypoplastic models. Therefore, we attempt to combine the rate-independent constitutive theories with the rate-dependent rheological theories in which no contact stresses before failure is taken into account. Since the strain rate in the quasi-static stage is much smaller than that in the flowing stage, the combination will yield a multi-scale constitutive model for debris materials. The combined (or unified) model should be rate-dependent and capable of describing the material behavior from the quasi-static stage to the fast flowing stage.

1.2 Contents

This thesis is organized as follows. Based on Bagnold's constitutive theory for a gravity-free suspension [5] introduced in Section 2.1, a framework which consists of a static portion for the frictional behavior and a dynamic portion for the viscous behavior is proposed in Section 2.2. Bagnold's constitutive model is then slightly modified and employed as the dynamic portion. The Mohr-Coulomb criterion is used as the static portion and combined with the modified Bagnold's model to obtain a complete model for simple shear. This model is further extended to a three-dimensional constitutive model in Section 2.3. The performance of the proposed model is presented in Section 2.4 by verifying the capability of the modified Bagnold's model to predict exact stress state in the flowing stage and pointing out the shortcoming of the Mohr-Coulomb criterion to capture liquefaction in the initiation stage. In Chapter 3, the Mohr-Coulomb criterion is replaced by hypoplasticity for the static portion to obtain a unified model for debris materials. The key features of hypoplasticity are briefly introduced at first. Afterwards, the applicability of a specific hypoplastic model for describing the quasi-static state of granular-fluid flows is studied by simulating undrained simple shear test of saturated granular materials which is important for the initiation of debris flow. In Section 3.3, a complete constitutive model is obtained by combining the hypoplastic model with the modified Bagnold's model. The performance of the new model is demonstrated by some element tests. In Chapter 4, the new model is implemented in a Smoothed Particle Hydrodynamics (SPH) code and verified by simulating some boundary value problems of granular flow. The fundamentals of SPH are introduced at first. The mathematical framework of SPH and the implementation are presented in Section 4.2. The SPH code is used to simulate some element tests and compared with the analytic solutions in Chapter 3 in Section 4.3. Then the SPH code is applied to three boundary value problems to further verify the capability of the unified model. Finally, some conclusions are drawn in Chapter 5, where some perspectives for future work are discussed.

Chapter 2

The constitutive model for granular-fluid flows

2.1 Bagnold's theory

Debris flow is one of the most dangerous and destructive natural hazards in the mountainous area. A reasonable constitutive model for debris materials is the crucial part for the prediction of flow velocity and run-out distance in the numerical simulation. Due to the complexity of the composition of debris materials, it is very difficult to take all the particle-sizes of the solid compositions into account in a constitutive model. Thus, in constitutive modelling, debris material is normally simplified to be a mixture of monosized particles and Newtonian fluid, and can be treated as a fluid continuum with microstructural effect [24, 25].

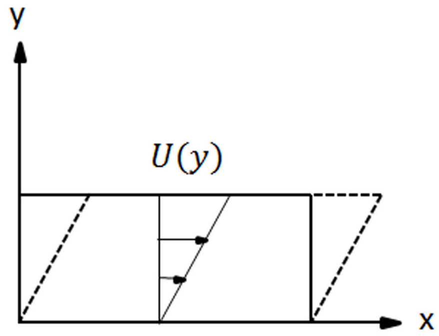

Figure 2.1: The schematic of a simple shear test.

Based on the study about a gravity-free dispersion of solid spheres sheared in Newtonian liquids, which can be treated as an undrained simple shear test shown in Figure 2.1, Bagnold

[5] proposed the following relationship between shear stress and shear strain rate

$$T_v = 2.25\lambda^{\frac{3}{2}}\mu\frac{\mathrm{d}U}{\mathrm{d}y} = k_1\frac{\mathrm{d}U}{\mathrm{d}y} \tag{2.1}$$

in the so-called 'macro-viscous' regime and following relationship

$$T_i = 0.042\rho_s(\lambda d)^2\left(\frac{\mathrm{d}U}{\mathrm{d}y}\right)^2 \sin\alpha_i = k_2\left(\frac{\mathrm{d}U}{\mathrm{d}y}\right)^2 \tag{2.2}$$

in the 'grain-inertia' regime for $\lambda < 12$, respectively. In the above expressions, μ is the dynamic viscosity of the interstitial fluid; ρ_s and d are the material density and the mean diameter of the grains, respectively; $\mathrm{d}U/\mathrm{d}y$ denotes the shear strain rate; the tangent of the angle α_i corresponds to the ratio between the shear and normal stress in the grain-inertia regime; λ is the linear concentration of solid particles defined by

$$\lambda = \frac{d}{s} = \left[\left(\frac{C_0}{C}\right)^{\frac{1}{3}} - 1\right]^{-1} \tag{2.3}$$

where s is the free distance between two particles, C is the mean solid volume fraction, and C_0 is the maximum possible solid volume fraction when $\lambda = \infty$ $(s = 0)$. In Bagnold's experiment [5], an analytical value of C_0 for spheres, 0.74, was used to calculate the linear concentration. In other experiments with different materials and testing devices, the maximum measured solid volume fractions were found related to the size of the particles and the container dimensions. For the applicability of (2.3) in different experiments, C_0 is replaced by the asymptotic limit of the maximum measured solid volume fraction, C_∞, as the container dimensions approach infinity [34].

The Bagnold number defined as

$$B = \frac{\lambda^{\frac{1}{2}}\rho_s d^2(\mathrm{d}U/\mathrm{d}y)}{\mu} \tag{2.4}$$

is used to characterize the flow as macro-viscous ($B < 40$), grain-inertia ($B > 450$) or transitional ($40 \leq B \leq 450$). The drag force of the interstitial fluid and particle collisions are considered to be dominant in the macro-viscous and grain-inertia regime, respectively.

The normal stress P, also termed dispersive pressure, is observed proportional to the shear stress with a constant value of about 0.75 in the macro-viscous region and decrease progressively from this value through the transition region, till it reaches another constant value at about 0.32 in the grain-inertia region. It is formulated as

$$\frac{T_v}{P_v} = \tan\alpha_v \tag{2.5}$$

and

$$\frac{T_i}{P_i} = \tan\alpha_i \tag{2.6}$$

where α_v and α_i correspond to the stress ratio in different regimes and relate to material properties. In Bagnold's experiments, the density of solid particles is equal to that of the interstitial fluids. It is an imaginative arrangement which highlights the effect of the fluid viscosity and particle collisions, eliminates the effect of gravity and makes the analysis of the experimental data easier. However, this setting also eliminates the yield stress, which exists in some debris materials. In addition, the relations (2.1) and (2.2) are developed for particular flow stages rather than the entire flow process. The constitutive relation for the transition region remains unspecified.

2.2 A constitutive framework for granular-fluid flows

During the past decades, much effort has been devoted to examine Bagnold's pioneer work by analysing the experimental procedure and apparatus [36], or using the conservation equations to verify the constitutive relations [8, 61, 75]. Based on these analyses, a framework for the models of solid-fluid flows is developed in this section.

As pointed out before, a shortcoming of Bagnold's model is that the stress-strain rate relations (2.1) and (2.2) are developed for two distinct regimes. There is no specific constitutive relation for the transition region between them. A model that can describe the stresses in the entire shearing process from the macro-viscous regime to the grain-inertia regime is required for the simulation of granular flow from quasi-static state to rapid shearing stage.

Based on the experimental results in [5], we assume that the total rheological shear stress T_r is the sum of T_v and T_i for $\lambda < 12$, i.e.

$$T_r = T_v + T_i. \tag{2.7}$$

Figure 2.2 shows the comparison between (2.7) and the test data with satisfactory agreement.

Similarly, the total rheological normal stress P_r can be described by

$$P_r = P_v + P_i. \tag{2.8}$$

As mentioned before, yield stress was not taken into account in Bagnold's models. However, the quasi-static stress-strain relation is an essential part of a complete model for common granular-fluid mixture in which the effect of gravity cannot be ignored. It was proposed that the

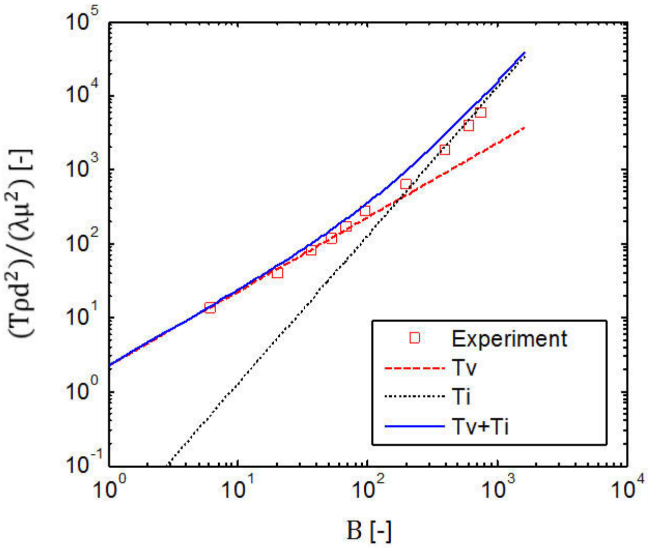

Figure 2.2: The result predicted by (2.7) for Bagnold's experimental data of $\lambda = 11$ [5].

constitutive equations for the flow of granular materials satisfied a generalized Mohr-Coulomb type yield criterion as $dU/dy \to 0$ [20, 70]. Shibata & Mei [75] assumed the following relation

$$T_0 = -fP_0 \operatorname{sgn}\left(\frac{\mathrm{d}U}{\mathrm{d}y}\right) \tag{2.9}$$

where T_0 and P_0 are the shear and normal stresses in the quasi-static state; f is an empirical coefficient of dynamic friction. Apparently, the specific expression of P_0 is the crucial point to determine the yield stress, and will be discussed in the following sections.

By combining the stresses in the quasi-static state with the rheological stresses for simple shear, constitutive model can be written out as follows

$$P = P_0 + P_r \tag{2.10a}$$

$$T = T_0 + T_r. \tag{2.10b}$$

The above simple model implies that the contributions of contact friction, fluid viscosity and particle collisions coexist in the entire flow process. P_0 and T_0 are regarded as the static portion of the framework. T_r and P_r are termed the dynamic portion.

Bagnold's tests [5] for two different interstitial fluids with different viscosities but the same density show significant differences of stresses in the slow shear stage and tend to the same stress-strain relation when the shear velocity is large enough. The explanation for this observation is that, in the rapid shear stage, the bulk behavior and dissipation of the flow kinetic energy are dominated by the inelastic and frictional particle collisions. An impact between two particles in a viscous liquid approximates a dry impact since the fluid effect is insignificant in comparison with the collision force in this stage [99]. Therefore, the linear term T_v

and P_v, rather than the quadratic terms T_i and P_i, help to distinguish granular-fluid mixtures with different interstitial fluid. Dry granular flow can be treated as a particular case where air is the interstitial fluid. However, in this case, the viscous terms T_v is normally much less than the yield stress T_0 in the beginning of the flow since the shear rate is very small in this stage. It is also negligible in the fast shearing stage since the viscous effect of air is insignificant compared to the frictional and collisional effect of particles. Thus, for dry granular flow, the framework (2.10) can be reduced to the following form.

$$P = P_0 + P_i \tag{2.11a}$$

$$T = T_0 + T_i. \tag{2.11b}$$

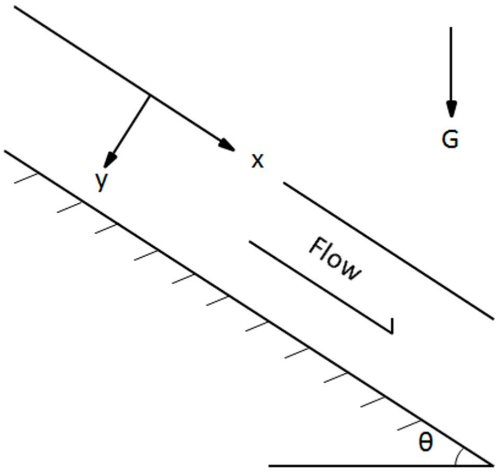

Figure 2.3: The schematic of an uniform granular-fluid flow on a slope.

For a free surface dry granular flow shown in Figure 2.3, as stated in [61], the relation (2.2) and (2.6) predict a steady uniform flow only when the slope θ is equal to the angle α_i. However, experimental results [7] show that such steady flow can be obtained not only at a single slope but over a slope range. This experimental observation can be predicted by the reduced framework (2.11) where a yield stress T_0 and the corresponded confining pressure P_0 are added to the inertial stresses [70, 60]. According to the force balance for a steady uniform flow, the following expressions can be obtained for free surface flow of dry granular material

$$P_0 + P_i = \rho_s C g h \cos\theta \tag{2.12a}$$

$$P_0 \tan\phi + P_i \tan\alpha_i = \rho_s C g h \sin\theta \tag{2.12b}$$

where g is the gravity acceleration; h is the depth along the y axis which is normal to the flow bed; ϕ is the internal friction angle at failure which is termed as residual friction angle or critical friction angle. Then we get the following stress ratio

$$\frac{P_0 \tan\phi + P_i \tan\alpha_i}{P_0 + P_i} = \tan\theta. \tag{2.13}$$

Let us assume that α_i is greater than the residual friction angle ϕ, which is consistent with the experimental observations of dry granular flows [68]. The normal stress P_i is zero in the critical state of flow triggering since the flow velocity is almost null at that time point. Thus, from (2.12) and (2.13), we obtain

$$P_0 = \rho_s C g h \cos\theta_1 \tag{2.14}$$

and

$$\tan\theta_1 = \tan\phi \tag{2.15}$$

where θ_1 is the critical inclination for the granular material start flowing. With increasing inclination, another critical state will be reached. In this state, the component of gravity perpendicular to the flowing bed is totally balanced by P_i since the flow velocity is large enough at this inclination. From (2.13), we get

$$\tan\theta_2 = \tan\alpha_i \tag{2.16}$$

where θ_2 is the maximum inclination for the equation (2.13) holds. It indicates that the framework (2.11), in which the stresses are divided into a static portion and a dynamic portion, can predict steady uniform flows over a slope range $\theta \in [\phi, \alpha_i]$.

For the case that the quasi-static stresses P_0 and T_0 decrease to same magnitude with the drag force T_v due to buoyancy of the interstitial fluid or liquefaction (or gasification) under undrained boundary condition, it is reasonable to speculate that the ratio between shear and normal stresses will vary from the residual friction coefficient $\tan\phi$ to the stress ratio of the 'macro-viscous' stage $\tan\alpha_v$ at first, and then converge to $\tan\alpha_i$ in the fast flow stage.

By taking the effect of the interstitial fluid into account, a constitutive model developed within the framework (2.10) can describe the stress-strain rate relations for both dry granular flows and granular-fluid flows. It is expected that the constitutive models based on this framework can capture the stress state throughout the shearing process from quasi-static to high-speed shearing stage.

2.3 A constitutive model for granular-fluid flows

In this section, a concrete simple-shearing model for granular-fluid flow is developed based on the framework (2.10). The specific expression for the flowing stage is determined by modifying former mentioned Bagnold's models. A conventional approach is employed to determine the yield stresses P_0 and T_0. The shortcoming of this approach is studied for further comparison with a hypoplastic model introduced in next chapter. Inspired by a common structure for some former models [89], the simple-shearing model is then extended to three-dimensional form. Although the static and dynamic portions are formulated in different mechanical framework, both the static and dynamic stresses in the new model are regarded as effective stress since they are stresses of the solid phase. Obviously, the shear stress from model (2.1) will vanish when the solid volume fraction decreases to zero.

2.3.1 Constitutive relation for the quasi-static state

As stated before, the yield stress T_0 is proportional to the normal stress P_0 with a constant friction coefficient. The empirical friction coefficient, f, is considered to be equal to tangent of the residual friction angle ϕ, which can be measured in simple shear tests [74], and is assumed independent of shear rate. From (2.9), the shear stress in the quasi-static stage is expressed as

$$T_0 = -P_0 \operatorname{sgn}\left(\frac{\mathrm{d}U}{\mathrm{d}y}\right)\tan\phi. \tag{2.17}$$

If P_0 is determined, the shear stress T_0 will be obtained consequently. The normal stress P_0 is usually produced by gravity. Take the free surface dry sand flow shown in Figure 2.3 as an example, the normal stress is the component of gravity perpendicular to the flow plane,

$$P_0 = \rho_s C g h \mathrm{cos}\theta. \tag{2.18}$$

For the case of granular-fluid flow with external load on the flow surface and in which no excess pore water pressure is developed, P_0 is easily determined by

$$P_0 = (\rho_s - \rho_f) C g h \cos\theta + P_l \tag{2.19}$$

where ρ_f is the density of the fluid and P_l is the external load component normal to the flowing bed.

The simple relation (2.17) can be easily implemented in numerical calculation. However, the simple treatments of the normal stress, (2.18) and (2.19), are not capable to describe some complex behaviors of granular-fluid mixtures in the quasi-static state, such as liquefaction which means gravity of the solid particles are fully or partially eliminated by the excess pore water pressure. These simple relations for the static stresses are used in the element tests in this chapter for comparison with the more sophisticated theory studied in next chapter.

2.3.2 Constitutive relations for the flowing state

The constitutive relations for the flowing state are developed based on Bagnold's constitutive model for concentrated gravity-free suspension [5]. From (2.1) and (2.2), two dimensionless quantities are obtained as

$$\frac{T_v \rho_s d^2}{\lambda \mu^2} = 2.25B \tag{2.20}$$

and

$$\frac{T_i \rho_s d^2}{\lambda \mu^2} = (0.042 \sin \alpha_i) B^2. \tag{2.21}$$

Both of them depend only on the Bagnold number B. Note that the above relationships are inconsistent with the experimental observation when the linear concentration, λ, is greater than 12 [5, 36]. Note further that the dimensionless quantities are also dependent on the linear concentration. Thus, the stress relations (2.20) and (2.21) are assumed to have the following forms

$$\frac{T_v \rho_s d^2}{\lambda \mu^2} = f_1(\lambda) B \tag{2.22}$$

and

$$\frac{T_i \rho_s d^2}{\lambda \mu^2} = f_2(\lambda) B^2 \tag{2.23}$$

where $f_1(\lambda)$ and $f_2(\lambda)$ are functions of λ to be specified.

(a) Shear stress in the macro-viscous regime

We first investigate the shear stress in the macro-viscous regime and attempt to propose a constitutive model suitable for the whole spectrum of λ in Bagnold's experiments. Actually, Bagnold derived an expression of the total shear stress for the viscous case as

$$\overline{T}_v = (1+\lambda)\left[1 + \frac{1}{2} f(\lambda)\right] \mu \frac{\mathrm{d}U}{\mathrm{d}y}, \tag{2.24}$$

in which $\overline{T}_v$ is the total shear stress composed of the grain and fluid contributions T_v and τ_v; $f(\lambda)$ is a function of linear concentration which determines the amplitude of the shear velocity fluctuation with $f(0) = 0$. The question to be answered is that how to split the total shear stress, $\overline{T}_v$, into T_v and τ_v. Bagnold assumed a simple relation for the fluid contribution to the total shear stress in the grain-inertia regime as [6, 36]

$$\tau_i = \frac{\tau_0}{(1+\lambda)}, \tag{2.25}$$

where τ_0 is the shear stress of pure fluid. The fluid contribution decreases with the increasing of the linear concentration. This relation is assumed also applicable in the macro-viscous regime, i.e.

$$\tau_v = \tau_i = \frac{\mu}{(1+\lambda)} \frac{\mathrm{d}U}{\mathrm{d}y}. \tag{2.26}$$

So, based on (2.24) and (2.26), we obtain the grain contribution of shear stress as

$$T_v = \overline{T}_v - \tau_v = \left\{ (1+\lambda) \left[1 + \frac{1}{2} f(\lambda) \right] - \frac{1}{1+\lambda} \right\} \mu \frac{\mathrm{d}U}{\mathrm{d}y}. \tag{2.27}$$

By introducing Bagnold's assumption that $f(\lambda) = \lambda$ into (2.27), the expression of T_v is preliminarily determined as

$$T_v = \left[(1+\lambda) \left(1 + \frac{1}{2}\lambda \right) - \frac{1}{1+\lambda} \right] \mu \frac{\mathrm{d}U}{\mathrm{d}y}. \tag{2.28}$$

Based on this relation, the dimensionless quantity for the 'macro-viscous' regime can be easily obtained

$$\frac{T_v \rho_s d^2}{\lambda \mu^2} = \left(\lambda^{-\frac{3}{2}} + \frac{3}{2}\lambda^{-\frac{1}{2}} + \frac{1}{2}\lambda^{\frac{1}{2}} + \frac{\lambda^{-\frac{3}{2}}}{1+\lambda} \right) B. \tag{2.29}$$

Obviously, (2.29) is a concrete form of the proposition (2.22) which is applicable for the granular-fluid flows with high granular concentration to some extent. For exact prediction, a further modification is required.

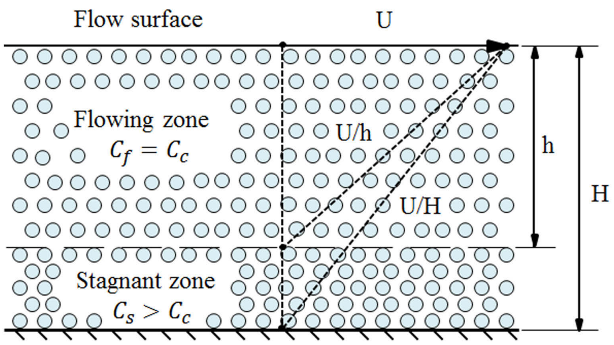

Figure 2.4: The schematic of a simple shearing granular-fluid flow with a stagnant zone beneath the flowing zone

A well-known phenomenon in granular-fluid flows is that the shear stress is relatively insensitive to the solid volume fraction when this parameter is below approximately 0.5, but increase rapidly when it exceeds this critical value [34]. Some previous works [23, 79] used a power series of the volume fraction (or the linear concentration) combined with an exponential term to describe the dynamic viscosity of granular-fluid mixture. These expressions were determined by fitting the shear stress vs shear strain rate curves. An important experimental observation that a stagnant zone exists in the shear tests of a dense granular-fluid mixture was ignored in these analyses. It's recognized that the solid volume fraction must be less than a critical value C_c to assure a full shearing to occur [5, 34]. Bagnold [6, 75] stated that C_c depends on the packing pattern and lies between 0.53 and 0.65. Let us consider a gravity flow shown in Figure 2.4. When the mean solid volume fraction C is greater than C_c, a stagnant zone with thickness $H - h$ appears at the bottom of the specimen. When C reaches the attainable maximum volume fraction in a specific apparatus, C_m, flows cannot happen and $h = 0$. For a uniform flow, such as Bagnold's experiments in 1954, a rational assumption is that $C_c = C_m$. In a steady flow with $C > C_c$, particles exchanging between the flowing and stagnant zone will reach a balance state. We deduce that the mean solid volume fraction in the upper layer, C_f, will keep at the critical value C_c and the mean value in the stagnant zone C_s is greater than C_c. Otherwise solid particles will move from the stagnant zone to the flowing zone till C_f is equal to C_c. For two cases with the solid volume fraction $C_1 < C_c$ and $C_2 > C_c$ respectively, the measured shear stresses with same shear velocity U are ${T_v}^1$ and ${T_v}^2$. Based on the above analysis, we have

$$ {T_v}^1 = \mu(C_1)\frac{\mathrm{d}U}{\mathrm{d}H} \tag{2.30} $$

and

$$ {T_v}^2 = \mu(C_c)\frac{\mathrm{d}U}{\mathrm{d}h} \tag{2.31} $$

where $\mu(\cdot)$ is the dynamic viscosity as a function of the mean solid volume fraction. It is easy to show that

$$ {T_v}^2 > {T_v}^1 \tag{2.32} $$

since

$$ \mu(C_c) > \mu(C_1) \tag{2.33} $$

and

$$ \frac{\mathrm{d}U}{\mathrm{d}h} > \frac{\mathrm{d}U}{\mathrm{d}H}. \tag{2.34} $$

The shear stress demonstrates dramatic increase when the solid volume fraction exceeds the critical value C_c. This is attributed to both the increase of the dynamic viscosity and the decrease of the flowing zone thickness. However, the total thickness H rather than h is normally used in the calculations of the dynamic viscosities, which would underestimate the shear rate $\mathrm{d}U/\mathrm{d}y$. Note that the existence of the stagnation zone is ignored in the constitutive modelling of granular-fluid flows. In other words, the critical value C_c should be taken into account in the constitutive model for granular-fluid mixture. Inspired by [75], we propose the following model for the shear stress in the macro-viscous regime.

$$ T_v = K_1\frac{\mathrm{d}U}{\mathrm{d}y}, \tag{2.35} $$

where

$$K_1 = \left[(1+\lambda)\left(1+\frac{1}{2}\lambda\right) - \frac{1}{1+\lambda}\right]\mu\left(1-\frac{C}{C_c}\right)^{-n} \tag{2.36}$$

is called effective viscosity; n is a fitting parameter. In Shibata & Mei's work [75], it was chosen $n = 1$.

(b) Shear stress in the grain-inertia regime

Bagnold's data [5] show that shear stresses in different regimes deviate as a whole with the varying of the linear concentration λ in the logarithm coordinates of $\rho_s d^2(\mathrm{d}U/\mathrm{d}y)^2$ vs grain shear stress. It is reasonable to assume that the shear stress in the 'grain-inertia' regime T_i changes in the same rate with T_v when λ is the single variable. Based on this assumption, Bagnold's model for the shear stress in the 'grain-inertia' regime, (2.2), is modified to be

$$T_i = \boldsymbol{K}_2\left(\frac{\mathrm{d}U}{\mathrm{d}y}\right)^2 \tag{2.37}$$

where

$$K_2 = 0.042 R_v \rho_s (\lambda d)^2 \sin\alpha_i \tag{2.38}$$

is the modified coefficient and

$$R_v = \frac{K_1}{k_1} = \frac{\left[(1+\lambda)\left(1+\frac{1}{2}\lambda\right) - \frac{1}{1+\lambda}\right]\left(1-\frac{C}{C_c}\right)^{-n}}{2.25\lambda^{\frac{3}{2}}} \tag{2.39}$$

is a correction factor.

(c) A simple shearing model for granular-fluid mixture

Substituting (2.35) and (2.37) into (2.7) yields the expression of shear stress in the flowing state

$$T_r = K_1\frac{\mathrm{d}U}{\mathrm{d}y} + K_2\left(\frac{\mathrm{d}U}{\mathrm{d}y}\right)^2. \tag{2.40}$$

Based on (2.5), (2.6) and (2.8), the normal stress in the flowing state is expressed as

$$P_r = \frac{K_1}{\tan\alpha_v}\frac{\mathrm{d}U}{\mathrm{d}y} + \frac{K_2}{\tan\alpha_\mathrm{i}}\left(\frac{\mathrm{d}U}{\mathrm{d}y}\right)^2. \tag{2.41}$$

The modified models are capable to describe the stress state of a granular-fluid mixture from the 'macro-viscous' regime to the 'grain-inertia' regime even with high solid volume fraction. As shown in Figure 2.5, by choosing $n = 0.2$ and $C_c = 0.65$ [34], (2.40) and (2.41) can reproduce the experimental results in [5].

Furthermore, based on the framework (2.10), the dynamic stresses (2.40) and (2.41) are combined with the static stresses T_0 and P_0, respectively, to obtain a simple-shearing model as

$$P = P_0 + \frac{K_1}{\tan\alpha_v}\frac{\mathrm{d}U}{\mathrm{d}y} + \frac{K_2}{\tan\alpha_i}\left(\frac{\mathrm{d}U}{\mathrm{d}y}\right)^2 \tag{2.42a}$$

$$T = -P_0\,\mathrm{sgn}\left(\frac{\mathrm{d}U}{\mathrm{d}y}\right)\tan\phi + K_1\frac{\mathrm{d}U}{\mathrm{d}y} + K_2\left(\frac{\mathrm{d}U}{\mathrm{d}y}\right)^2 \tag{2.42b}$$

which is applicable to the whole flow process, from the quasi-static state to rapidly flowing stage.

2.3.3 The three-dimensional form of the simple-shearing model

Now we try to extend (2.42) into the general three-dimensional form. A simplest model describing the non-Newtonian fluid (see e.g. [89]) may take the form

$$\mathbf{T} = a_1\mathbf{1} + a_2\mathbf{D} \tag{2.43}$$

where $\mathbf{T}$ is the Cauchy stress tensor; $\mathbf{1}$ and $\mathbf{D}$ denote the unit tensor and the strain rate tensor, respectively. The coefficients

$$a_i = f_i(I_D, II_D, III_D, C, \mathrm{grad}C), \quad (i = 1, 2) \tag{2.44}$$

are functions of the volume fraction C and the invariants of the strain rate tensor

$$\begin{aligned} I_D &= tr\mathbf{D}, \\ II_D &= \frac{1}{2}((tr\mathbf{D})^2 - tr(\mathbf{D}^2)), \\ III_D &= det\mathbf{D}. \end{aligned} \tag{2.45}$$

In the case of isochoric, two-dimensional and fully developed channel flow, a_i depends only on II_D, C and $\mathrm{grad}C$ since I_D and III_D are equal to zero. Savage [70] proposed a tensor form model as

$$\mathbf{T} = s_1 \mid II_D \mid \mathbf{1} + s_2\sqrt{\mid II_D \mid}\mathbf{D} \tag{2.46}$$

where s_1 and s_2 are functions of C; $|\cdot|$ denotes absolute value.
In the extension of the simple shearing model, we keep the assumption of isochoric, which is corresponding to the definition of failure in elastoplasticity, and neglect the effect of the third invariant of the strain rate tensor. Thus, the simple-shearing model is extended to be the three-dimensional form model as

$$
\begin{aligned}
\mathbf{T} = &-\left(P_0 + \frac{2K_1}{\tan\alpha_v}\sqrt{\mid II_D \mid} + \frac{4K_2}{\tan\alpha_i} \mid II_D \mid\right)\mathbf{1} \\
&+ \left(\frac{P_0 \tan\phi}{\sqrt{\mid II_D \mid}} + 2K_1 + 4K_2\sqrt{\mid II_D \mid}\right)\mathbf{D}^*
\end{aligned}
\tag{2.47}
$$

where

$$
\mathbf{D}^* = \mathbf{D} - \frac{\mathrm{tr}(\mathbf{D})}{3}\mathbf{1} \tag{2.48}
$$

is the strain rate deviator tensor which is used to avoid double counting of the normal stresses. It can be easily demonstrated that, for an undrained simple shearing flow shown in Figure 2.1 where the strain rate deviator tensor takes the form

$$
\mathbf{D}^* = \mathbf{D} = \begin{bmatrix} 0 & \frac{1}{2}\mathrm{d}U/\mathrm{d}y & 0 \\ \frac{1}{2}\mathrm{d}U/\mathrm{d}y & 0 & 0 \\ 0 & 0 & 0 \end{bmatrix}, \tag{2.49}
$$

the general three-dimensional model, (2.47), will reduce to the simple-shearing form (2.42).

2.4 Performance of the proposed model

In this section, some element test results are presented to verify the applicability of the model (2.47) in the cases with different materials and experimental apparatus. The new model is used to predict the stress-strain relations obtained in two different granular-fluid flows which can be treated as undrained simple shear tests in the simulations.

2.4.1 Dry granular materials

The experimental data of dry granular materials sheared in a annular shear cell were reported by Savage & Sayed [74]. The data for 1.0 mm spherical polystyrene beads are selected for the element tests. They were measured on the top of the sample where h is equal to 0. As stated in the paper [74], the loads applied by the upper disk, P_l, range from 100 to 1500 N/m^2. However, the exact load for each sample was not reported. By checking the measured normal stress for 1.0 mm beads, we assume that P_0 has a value around 100 N/m^2 which is regarded as the residual stress at the critical point of yielding. As mentioned before, the theoretical maximum value of solid volume fraction, C_0, will be replaced by the asymptotic limit of the maximum measured solid volume fraction, C_∞, in the calculation for a specific experiment. Since the exact value of C_∞ was not reported in Savage & Sayed's work, we use 0.64 which is a typical value for monosized spheres [34, 6]. The critical volume fraction C_c is approximately 0.62 [75]. All the parameters for the new model are listed in Table 3.4 and Table 2.2.

Table 2.1: Parameters for the shear tests of 1.0 mm beads in [74]

d	C_∞	C_c	ρ_s	ρ_f	μ	ϕ	θ
$[mm]$	[-]	[-]	$[kg/m^3]$	$[kg/m^3]$	$[Pa \cdot s]$	[°]	[°]
1.0	0.64	0.62	1095	1.29	1.83×10^{-5}	23	0

Table 2.2: Stress ratios measured in the shear tests of 1.0 mm beads in [74]

C	$\tan \alpha_v$	$\tan \alpha_i$
[-]	[-]	[-]
0.461	0.50	0.51
0.483	0.40	0.51
0.504	0.30	0.51
0.524	0.30	0.51

As shown in Figure 2.6, the predicted curves can fit the data with high shear strain rate very well. The non-quadratic dependence of the stresses on the shear rate in the slow shear stage for dense specimen is also captured by the new model. The slight overestimations for the samples with $C < 0.524$ may be due to the use of inaccurate P_0. The assumed value 100 N/m^2 is greater than the value in the tests with $C < 0.524$. However, 100 N/m^2 is the former stated minimum normal stress applied by the upper disk. The phenomenon that P_0 is less than the minimum value can only be explained by assumption that liquefaction occurs in the relatively loose samples under undrained boundary condition. In Savage & Sayed's tests, the shear velocity was adjusted to keep the height constant and thus keep the volume of the samples unchanged. This is equivalent to undrained boundary condition for saturated granular materials. In this case, the confining pressure P_0 which corresponds to the mean effective stress in soil mechanics would decrease to a residual value to eliminate the tendency of volume compression before yielding. A looser specimen will show lower residual strength. The simple relations (2.17) and (2.19), as the static portion of (2.47), cannot capture the decreasing of P_0.

2.4.2 Granular-water mixture

Another element test is based on Hanes & Inmans laboratory tests [34] about spherical particles sheared in water. The data for particles with diameter 1.85 mm is selected for the element tests since it was stated as good quality data. The maximum measured volume fraction for 1.85 mm particles was reported to be 0.55 in the literature. The asymptotic limit C_∞ is presumed to be approximately 0.61. The critical volume fraction is determined to be 0.52 due to a partially shearing with $C = 0.53$ was reported. The load from the upper disk P_0 is almost 200 N/m^2. The angle α_v is assumed equal to the dynamic angle of repose, 28°. All the parameters are listed in Table 3.7 and Table 2.4.

Table 2.3: Parameters for the shear tests of 1.85 mm beads in [34]

d	C_∞	C_c	ρ_s	ρ_f	μ	ϕ	θ
$[mm]$	[-]	[-]	$[kg/m^3]$	$[kg/m^3]$	$[Pa \cdot s]$	[°]	[°]
1.85	0.61	0.52	2780	1000	1.0×10^{-3}	0.59	0

Table 2.4: Stress ratios measured in the shear tests of 1.85 mm beads in [34]

C	$\tan\alpha_v$	$\tan\alpha_i$
[-]	[-]	[-]
0.49	0.53	0.59
0.51	0.53	0.59

The simulation results are shown in Figure 2.7. The predicted results of $C = 0.51$ show well-fitting with the experimental data. Similar with the element test of dry granular flow, the stresses of the relatively loose sample, $C = 0.49$, are slightly overestimated. The inaccurate prediction of the residual stresses, P_0 and T_0, are considered to be responsible for this result. According to the experimental data, the real residual stresses of the two samples should have different value, and the sample with $C = 0.49$ should have a residual normal stress less than 200 N/m^2. Nevertheless, the dynamic portion of the new model (2.47) shows competent to describe the stress-shear rate relation in the flowing stage. More suitable theory for describing granular-fluid mixture before yielding will be studied in the following chapters.

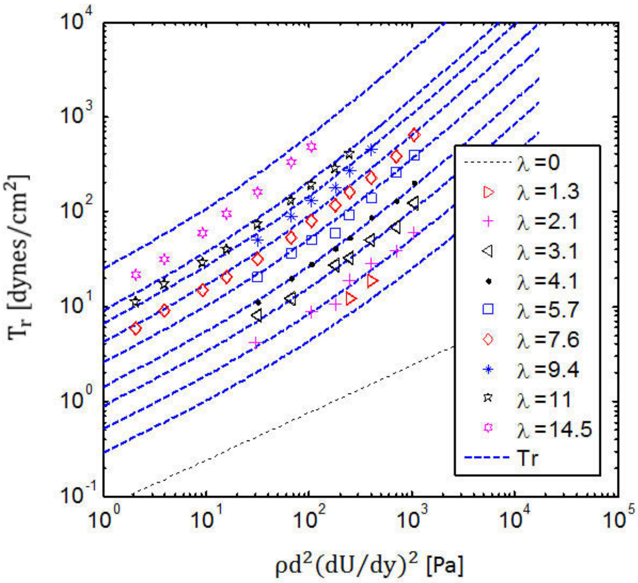

(a)

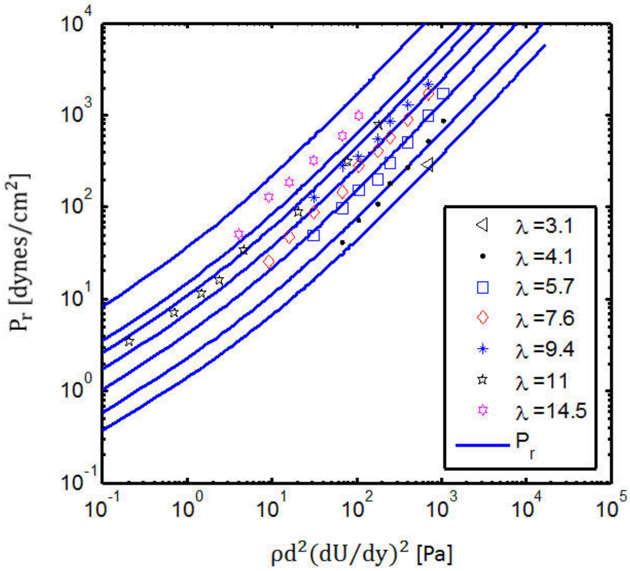

(b)

Figure 2.5: The predicted curves by (2.40) and (2.41) with $n = 0.2$ for the data from (a) the figure 3 and (b) the figure 4 in [5]. The experimental data are indicated by various symbols. The dashed lines (upper panel) denote the shear stress while the solid lines (lower panel) for the normal stress.

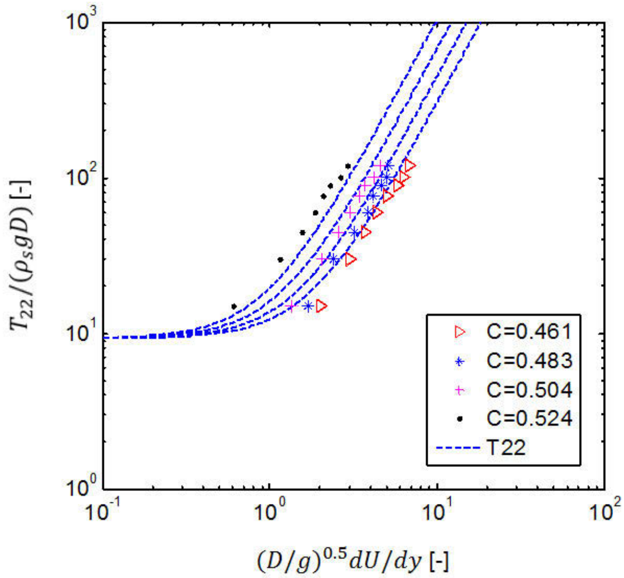

(a)

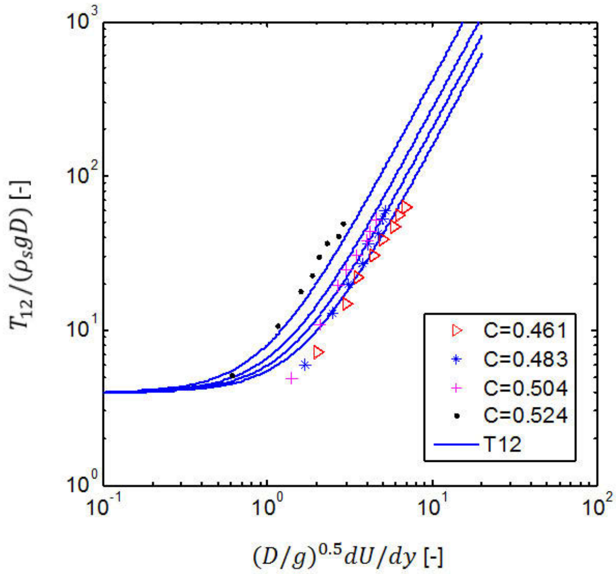

(b)

Figure 2.6: Element test results for the dry granular flow with different solid volume fraction: (a) nondimensional shear rate vs normal stress (b) nondimensional shear rate vs shear stress. The experimental data are indicated by various symbols. The dashed lines (upper panel) denote the normal stress while the solid lines (lower panel) for the shear stress.

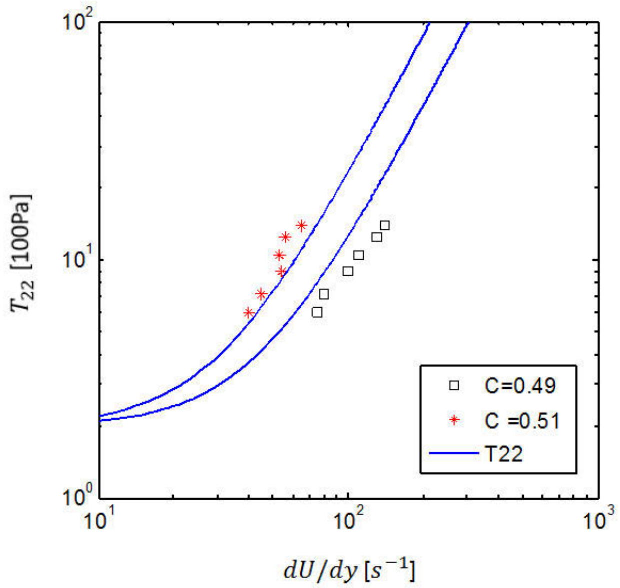

(a)

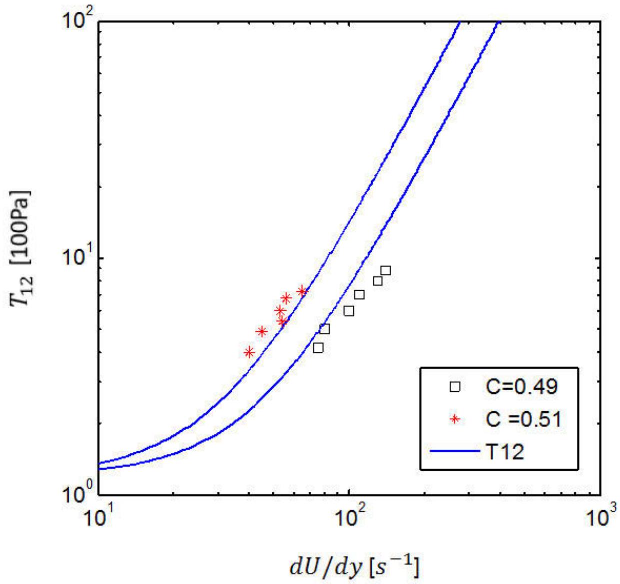

(b)

Figure 2.7: Element test results for the granular-water flow with different solid volume fraction: (a) normal stress (b) shear stress. The experimental data are indicated by various symbols. The solid lines denote the normal stress in the upper panel and the shear stress in the lower panel.

Chapter 3

Hypoplastic constitutive model for debirs flows

As pointed out in the previous chapter, the static portion of the model (2.47) cannot describe the shear softening (or liquefaction) of granular-fluid mixtures in the undrained simple shearing which is particularly relevant for the initiation of debris flows. More suitable constitutive theories are required to determine the residual stresses P_0 and T_0 exactly for debris materials. Now we try to study the applicability of a prospective theory, hypoplasticity, for the description of partial or full liquefaction of saturated granular materials and further determine a specific constitutive model which can capture the solid-like and fluid-like behaviors of debris materials.

3.1 Introduction of hypoplasticity

Hypoplasticity was developed for anelastic materials as an alternative to elastoplasticity. As well known, elastoplasticity is characterized by a series of additional notions, such as yield surface, flow rule and plastic potential ect., which hide the mathematical structure of the constitutive equation. The various elastoplastic constitutive models are difficult to be implemented in some common methods of numerical calculation and sensitive to parameters controlling the various involved numerical algorithms [50]. The outstanding feature of hypoplasticity is its simplicity since the additional notions introduced by elastoplasticity are not employed, and same formula is used for both loading and unloading. The distinguishing of loading and unloading is automatically accomplished by the hypoplastic equation itself. In addition, the anelastic deformation is recognized to set on from very beginning of the loading process in hypoplasticity. Thus, a prior distinguishing between elastic and plastic deformations is not required. These features make hypoplastic constitutive models easier to be implemented into numerical calculations.

The origin of hypoplasticity can be traced back to the work of Trusedell in the 1950s. A concept for constitutive equations entitled 'Hypoelasticity' was proposed by expressing the stress rate as a function of the stress and the strain rate [84]

$$\overset{\circ}{\mathbf{T}} = \mathbf{L}(\mathbf{T}, \mathbf{D}) \tag{3.1}$$

where $\overset{\circ}{\mathbf{T}}$ is the Jaumann stress rate tensor; $\mathbf{T}$ is the Cauchy stress tensor and $\mathbf{D}$ is the strain rate tensor; $\mathbf{L}$ is an isotropic tensorial function of its arguments and is linear in $\mathbf{D}$; Truesdell's work was primarily conceived as an elasticity theory in rate form. It turned out that the constitutive equations based on this concept are capable of describing the phenomenon of failure or rupture. However, Truesdell himself was unsure about the physical relevance of his theory at that time [97]. In the followed works [80, 30, 31], it was recognized that the behavior upon reversal of strain rate cannot be described with a single hypoelastic equation. Attempts for solving this problem, which yield a hybrid of hypoelasticity and plasticity, were regarded as a patchwork in which the vision of developing a plasticity theory without its additional notions was not realized. A renaissance of hypoelasticity appeared in modelling the behaviors of pressure sensitive media, such as concrete [19] and dense sand [78], about two decades later. However, the behavior upon unloading and reloading remained untouched [97]. In the application of hypoelasticity for metallic materials, the failure criterion was formulated as the vanishing determinant of the stiffness matrix by Tokuoka [81, 82, 83]. It is worth mentioning that some ideas about failure in hypoplasticity are inspired by his work. About the same time, Krawietz [51] devoted to a work on the theoretical foundation of hypoelasticity, which however had as good as no impact on the practical application. The pioneering work of hypoplasticity was the proposing of an incrementally nonlinear constitutive equation for soils, which was still termed generalised hypoelasticity, by Kolymbas in 1977 [47]. Although the model has the main ingredient of hypoplasticity, the daunting tensorial functions and the numerous coefficients make it too complex to be applied. This state was broken until a breakthrough was achieved by Kolymbas [48, 49]. A tensorial equation with only four terms, two linear terms and two nonlinear terms, was developed. The elegant formulation and the simple calibration procedure made the equation the subject of years of intensive research. Further investigation found some drawbacks of this model. And the fact that the constitutive equation possesses no bound surface force researchers to abandon this model. Based on a frantic search, some improved versions of hypoplastic constitutive equations were presented ([96, 94, 10, 92]). At the same time, the discovery of the bound surface [98] made it necessary to formulate a framework instead of working with specific versions. The formal definition of hypoplasticity was proposed by Wu and Kolymbas in 1990 [96] as the following form.

$$\overset{\circ}{\mathbf{T}} = \mathbf{H}(\mathbf{T}, \mathbf{D}) \tag{3.2}$$

where $\mathbf{H}$ is a tensorial function which is required to be continuously differentiable for all $\mathbf{D}$ except at $\mathbf{D} = 0$, the Jaumann stress rate $\mathring{\mathbf{T}}$ is determined by

$$\mathring{\mathbf{T}} = \dot{\mathbf{T}} + \mathbf{TW} - \mathbf{WT}. \tag{3.3}$$

Here, $\dot{\mathbf{T}}$ is the time derivative of the Cauchy stress $\mathbf{T}$, and $\mathbf{W}$ is the rotation rate (spin vector). Since the formulation (3.2) is too broad to determine a concrete constitutive equation, some restrictions, which are based on the general principles of continuum mechanics or experimental observations, are imposed on the function $\mathbf{H}$. They are described as following [97]:

1. The function $\mathbf{H}$ for describing rate-independent behavior must be positively homogeneous of the first order in the strain rate $\mathbf{D}$. Thus,

   $$\mathbf{H}(\mathbf{T}, \lambda\mathbf{D}) = \lambda\mathbf{H}(\mathbf{T}, \mathbf{D}) \tag{3.4}$$

   where λ is a positive but otherwise arbitrary scalar.

2. The function $\mathbf{H}$ should fulfill the following condition in order to be objective.

   $$\mathbf{H}(\mathbf{QTQ}^T, \mathbf{QDQ}^T) = \mathbf{QH}(\mathbf{T}, \mathbf{D})\mathbf{Q}^T \tag{3.5}$$

   where Q is an orthogonal tensor. The equation (3.5) can be met when the function $\mathbf{H}$ is generated according to the representation theorem for isotropic tensorial functions. For a tensorial function of two symmetric tensors, $\mathbf{T}$ and $\mathbf{D}$, the representation theorem can be written as [76, 87, 88]

   $$\begin{aligned} \mathring{\mathbf{T}} \;=\; & \alpha_0\mathbf{1} + \alpha_1\mathbf{T} + \alpha_2\mathbf{D} + \alpha_3\mathbf{T}^2 + \alpha_4\mathbf{D}^2 + \alpha_5(\mathbf{TD} + \mathbf{DT}) \\ & + \alpha_6(\mathbf{T}^2\mathbf{D} + \mathbf{DT}^2) + \alpha_7(\mathbf{TD}^2 + \mathbf{D}^2\mathbf{T}) + \alpha_8(\mathbf{T}^2\mathbf{D}^2 + \mathbf{D}^2\mathbf{T}^2) \end{aligned} \tag{3.6}$$

   where $\mathbf{1}$ is the unit tensor. The coefficient α_i(i = 0, ... , 8) are the function of the invariants and joint invariants of $\mathbf{T}$ and $\mathbf{D}$:

   $$\alpha_i = \alpha_i(\mathrm{tr}\mathbf{T}, \mathrm{tr}\mathbf{T}^2, \mathrm{tr}\mathbf{T}^3, \mathrm{tr}\mathbf{D}, \mathrm{tr}\mathbf{D}^2, \mathrm{tr}\mathbf{D}^3, \mathrm{tr}\mathbf{TD}, \mathrm{tr}\mathbf{T}^2\mathbf{D}, \mathrm{tr}\mathbf{TD}^2, \mathrm{tr}\mathbf{T}^2\mathbf{D}^2) \tag{3.7}$$

   where tr represents the trace of a tensor. Note that the isotropy of the tensorial function does not necessarily mean that the response is also isotropic.

3. In order to be applicable to the behavior of pressure sensitivity, the function $\mathbf{H}$ is required to be homogeneous in $\mathbf{T}$, which is formulated as

   $$\mathbf{H}(\lambda\mathbf{T}, \mathbf{D}) = \lambda^n\mathbf{H}(\mathbf{T}, \mathbf{D}) \tag{3.8}$$

   where n denotes the order of homogeneity. It implies that the tangential stiffness is proportional to the n-th power of the stress level $(\mathrm{tr}\mathbf{T})^n$, so that experiments conducted under different stress levels can be normalized by $(\mathrm{tr}\mathbf{T})^n$.

Without loss in generality, it is assumed that the constitutive equation (3.2) can be decomposed into two parts representing reversible and irreversible behavior of the material:

$$\overset{\circ}{\mathbf{T}} = \mathbf{L}(\mathbf{T}, \mathbf{D}) + \mathbf{N}(\mathbf{T}, \mathbf{D}) \tag{3.9}$$

where $\mathbf{L}$ and $\mathbf{N}$ are assumed linear and non-linear in the strain rate $\mathbf{D}$, respectively. $\mathbf{L}(\mathbf{T}, \mathbf{D})$ in equation (3.9) can be specified by invoking the representation theorem for isotropic tensorial functions. Since the non-linear dependence of $\mathbf{N}$ on $\mathbf{D}$ should also satisfy the restriction of rate-independence, we consider the following generalized form for hypoplastic constitutive equations [97]:

$$\overset{\circ}{\mathbf{T}} = \mathbf{L}(\mathbf{T}, \mathbf{D}) + \mathbf{N}(\mathbf{T})||\mathbf{D}|| \tag{3.10}$$

where $||\mathbf{D}|| = \sqrt{\mathrm{tr}\mathbf{D}^2}$ stands for the Euclidean norm. The same symbol $\mathbf{N}$ is retained in (3.10) to avoid confusion. It is clear that no predefined notions, such as yield surface, flow rule and plastic potential which are necessary for a elastoplastic constitutive equation, are used in the developing of hypoplastic constitutive equations.

Within the framework (3.10), a simple hypoplastic constitutive model is proposed by Wu and Bauer [94] for sand as

$$\overset{\circ}{\mathbf{T}} = c_1(tr\mathbf{T})\mathbf{D} + c_2\frac{tr(\mathbf{T}\mathbf{D})\mathbf{T}}{tr\mathbf{T}} + (c_3\frac{\mathbf{T}^2}{tr\mathbf{T}} + c_4\frac{\mathbf{T}^{*2}}{tr\mathbf{T}}) \parallel \mathbf{D} \parallel \tag{3.11}$$

where $c_i(i = 1, ..., 4)$ are dimensionless material parameters; $\mathbf{T}^*$ is the deviatoric stress tensor expressed by

$$\mathbf{T}^* = \mathbf{T} - \frac{1}{3}(tr\mathbf{T})\mathbf{1}. \tag{3.12}$$

The hypoplastic model (3.11) possesses simple mathematical formulation and contains only four material parameters, $c_1 \sim c_4$, which are related to some widely used parameters in soil mechanics, such as the initial tangent modulus E_i and the internal friction angle ϕ_0. The specific determination process of $c_1 \sim c_4$ can be obtained in the literatures [9, 94, 95]. Two stress states, the initial hydrostatic and the state at failure, are chosen for the identification of $c_1 \sim c_4$ based on a triaxial test with constant confining pressure, i. e. $\dot{\mathbf{T}}_h(2,2) = \dot{\mathbf{T}}_h(3,3) = 0$. And then, the following parameters are introduced:

the stress ratio, $R = \mathbf{T}_h(1,1)/\mathbf{T}_h(3,3)$;

the initial tangent modulus, $E_i = [(\dot{\mathbf{T}}_h(1,1) - \dot{\mathbf{T}}_h(3,3))/\mathbf{D}(1,1)]_{R=1}$;

the initial Poisson ratio, $\upsilon_i = [\mathbf{D}(3,3)/\mathbf{D}(1,1)]_{R=1}$;

the failure stress ratio, $R_f = [\mathbf{T}_h(1,1)/\mathbf{T}_h(3,3)]_{max}$;

the failure Poisson ratio, $\upsilon_f = [\mathbf{D}(3,3)/\mathbf{D}(1,1)]_{R=R_f}$.

The failure stress ratio R_f and the failure Poisson ratio υ_f are related to the internal friction angle ϕ_0 and the dilatancy angle ψ, respectively, through the following relations [94]:

$$R_f = \frac{1 + \sin\phi_0}{1 - \sin\phi_0} \tag{3.13}$$

and

$$\upsilon_f = \frac{1 + \tan\psi}{2}. \tag{3.14}$$

Taking the four material constants $c_1 \sim c_4$ as unknowns, a system of four linear equations can be obtained by substituting the corresponded stress and strain rate of the two stress states into the model (3.11). Therefore, the material constants are determined as functions of the well-established parameters in soil mechanics, the initial tangent modulus E_i, the initial Poisson ratio υ_i, the internal friction angle ϕ_0 and the dilatancy angle ψ. It should be pointed out that these parameters are related to a specific confining pressure, all the sets of material constants used in this thesis are obtained with a confining pressure $\mathbf{T}_h(3,3) = 100kPa$. In addition, the deviatoric loading in the initial hydrostatic state is considered to be zero, i. e. the initial Poisson ratio $\upsilon_i = 0$.

It is worth to mention that although the additional notions in elastoplasticity, such as failure surface and flow rule, are not employed in hypoplasticity, these notions can be derived from hypoplasticity based on the definition of failure that

$$\begin{cases} \mathring{\mathbf{T}} = \mathbf{0}, \\ \mathbf{D} \neq \mathbf{0}, \\ \mathrm{tr}\mathbf{D} = 0. \end{cases} \tag{3.15}$$

The failure surface derived from the hypoplastic model 3.11 is shown in Figure 3.1 (a) which indicate that the failure surface is a cone in three-dimensional principal stress space, similar with that of some widely used failure criteria, such as WillamWarnke criterion and Matsuoka-Nakai criterion. The plastic flow directions shown in Figure 3.1 (b) demonstrate a non-associative flow rule of the hypoplastic model 3.11.

3.2 The applicability of hypoplastic models for debris materials

Now we try to find a suitable hypoplastic model for the static portion of the constitutive model for debris materials and further study its capability for describing the shear softening occurred at the initiation stage of debris flows. Two hypoplastic models, the one developed by Wu et al. [95] and the one by Gudehus [32], are compared in the selection of the static portion for

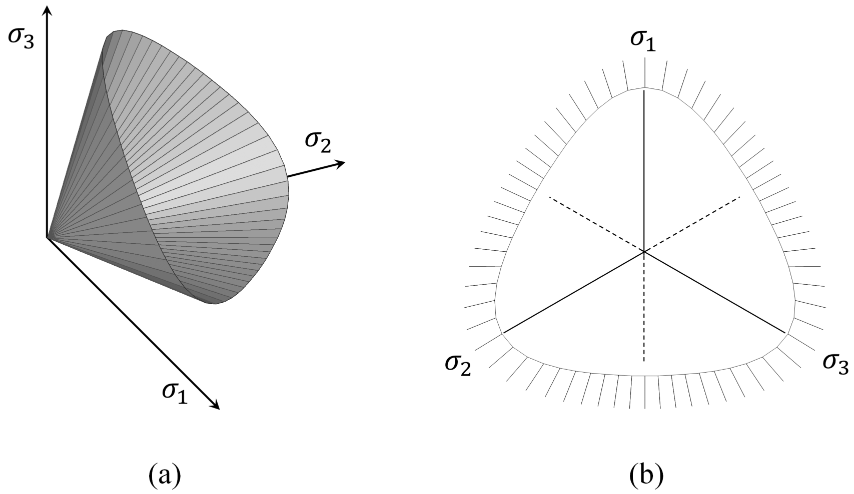

Figure 3.1: Failure surface and flow rule derived from the constitutive equation (3.11): (a) failure surface; (b) flow rule on the π-plane.

the framework (2.10). In the more recent models by Gudehus[32], mainly the stiffness is modified by the two factors, f_b and f_e, which take into account the influence of stress state and density, respectively. In modelling debris flow, however, the strength is very important and the stiffness is not important. Moreover, his model makes use of the exponential functions for the dependence of critical void ratio and minimum void ratio on pressure. For each function the parameters reduce from 3 to 2. However, there are only few data in the literature for the exponential functions. Therefore, in this chapter, we will embark on the model proposed by Wu et al. [95] which is the first hypoplastic model with critical state to verify that, by employing an appropriate hypoplastic model as the static portion, the combined model based on the framework (2.10) can fulfill an entire and quantitative description of stress state for debris materials from quasi-static stage to fast flow stage. The hypoplastic model with critical state has the form as

$$\mathring{\mathbf{T}}_h = c_1(tr\mathbf{T}_h)\mathbf{D} + c_2\frac{tr(\mathbf{T}_h\mathbf{D})\mathbf{T}_h}{tr\mathbf{T}_h} + (c_3\frac{{\mathbf{T}_h}^2}{tr\mathbf{T}_h} + c_4\frac{{\mathbf{T}_h}^{*2}}{tr\mathbf{T}_h}) \parallel \mathbf{D} \parallel I_e, \tag{3.16}$$

where the subscript h is used to distinguish the hypoplastic portion from the dynamic portion in the model which will be developed for debris materials; the introduced factor I_e is called density function and defined as

$$I_e = (a-1)D_c + 1 \tag{3.17}$$

where a is a material parameter related to the stress level and

$$D_c = \frac{e_{crt} - e}{e_{crt} - e_{min}} \tag{3.18}$$

is the modified relative density; e denotes the void ratio; e_{min} and e_{crt} are the minimum and the critical void ratio, respectively. The effect of void ratio and stress level on the behavior of granular materials is taken into account in the model (3.16) by using the following expressions,

$$e_{crt} = p_1 + p_2 \mathrm{exp}(p_3 \mid tr\mathbf{T}_h \mid), \tag{3.19}$$

and

$$a = q_1 + q_2 \mathrm{exp}(q_3 \mid tr\mathbf{T}_h \mid) \tag{3.20}$$

where $p_i(i = 1, ..., 3)$ and $q_i(i = 1, ..., 3)$ are material parameters and can be determined by fitting the experimental data of drained triaxial tests under different confining pressure. It is shown that the model (3.16) is applicable to both initially and fully developed plastic deformation of granular materials with drained or undrained conditions [94, 95]. It will reduce to the original model (3.11) when the void ratio e is equal to the critical value e_{crt} from (3.17) and (3.18). It means, for same material, same constants $c_1 \sim c_4$ will be obtained for the original and extended models in the case of $e = e_{ecrt}$. Thus, the material constants emerging in the model (3.16) can be determined by the same way for (3.11). The dilatancy angle ψ is equal to zero since there is no volume deformation in this case [97]. About the material parameters $p_i(i = 1, ..., 3)$ and $q_i(i = 1, ..., 3)$, some theoretical and experimental analysis are presented in [95]. p_1 is the critical void ratio when the confining pressure approaches infinity, since p_3 is negative. The value of p_1 should be close to the minimum void ratio under a high confining pressure. For the case of zero confining pressure, the critical void ratio is equal to $p_1 + p_2$ which may close to the maximum void ratio measured with very low confining pressure. q_1 is assumed to be always equal to 1 and q_3 is a negative value. For the case of $tr\mathbf{T}_h \to \infty$, the difference between dense and loose packing tends to disappear since the parameter $a \to 1$. Based on the numerical parametric study [95], q_2 is suggested to lie in the range (-0.3, 0.0). p_3 and q_3 for quartz sand are assumed to be -0.0001 kPa. In the case of very low confining pressure, such as the state of liquefaction, relatively higher values of q_2, p_3 and q_3 may be needed to keep the sensitivity of I_e to the stress level.

The hypoplastic model (3.16) may be the proper model to describe the shear softening (liquefaction) and to capture the residual strength in the beginning of a debris flow. It is worth to mention that the hypoplastic model with critical state is just one of the choices for describing the initiation of debris flows. Recently some improved models have been available e.g. [52, 77, 29], which are developed from some widely used versions of hypoplastic model [64, 86] and aim to improve the dependence of stiffness on pressure and density. However, the capability of these models for capturing the phenomenon of liquefaction and the stability in the cases of large deformation or low confining pressure still need to be verified. A more concise hypoplastic model with the former mentioned capability and stability can be employed to determine the stress state in the quasi-static stage of debris materials.

In a debris flow, the material is subjected to large shear deformation. For developing and evaluating constitutive models the planar simple shear motion is particularly relevant [33]. Therefore, we try to verify the applicability of the hypoplastic model (3.16) in the simulation of debris flow initiation by using this model to reproduce the typical experimental results of granular materials in undrained simple shear tests. As presented in the literatures [15, 101], saturated sand specimens with different initial void ratios demonstrate three types of stress-strain behavior in undrained simple shear tests as indicated in Figure 3.2: (i) the dense specimens have tendency of dilation and show shear hardening to reach a ultimate steady state (USS) finally; (ii) the very loose specimens demonstrate shear softening to obtain constant residual strength or complete liquefaction in the critical steady state (CSS); (iii) the specimens with medium void ratio first soften, then harden and reach also a ultimate steady state [100]. The shear softening is considered to be the main mechanism in the mobilization of debris flows.

Now we intend to reproduce these three types of stress-strain behavior in the element tests. We are more concerned with the qualitative than with the quantitative outcome since some important material parameters are not available in [101]. In order to obtain the material constants $c_1 \sim c_4$ for sand in the critical state with $I_e = 1$, the initial tangent modulus E_i is determined approximately by the following relation [42, 85]

$$\frac{E_i}{P_a} = 150 \left(\frac{\sigma_{33}}{P_a} \right)^{0.5}, \tag{3.21}$$

in which P_a is the atmospheric pressure (101.3 kPa) and σ_{33} is the effective confining stress, given as 100 kPa in the experiments. Thus the initial tangent modulus is obtained approximately 15 MPa. A relatively low friction angle ϕ_0 of 25° is assumed for saturated loose sand in the critical state with $e = e_{crt}$. Both the initial Poisson ratio υ_i and the dilatancy angle ψ are assumed to be 0 as stated before. The determined material constants for the model (3.16) are presented in Table 3.1.

Table 3.1: Material constants for the model (3.16) in the simulation of the undrained simple shear tests in [101]

c_1	c_2	c_3	c_4
[-]	[-]	[-]	[-]
-50.0	-629.6	-629.6	1220.8

The three types of stress-strain behavior are reproduced as shown in Figure 3.3, when the values in Table 3.2 are employed for p_i and q_i in the relations (3.19) and (3.20).

The following observations can be made. In the hardening regime, an increase of the stress level gives rise to a reduction of the critical void ratio e_{crt} and increases the parameter a,

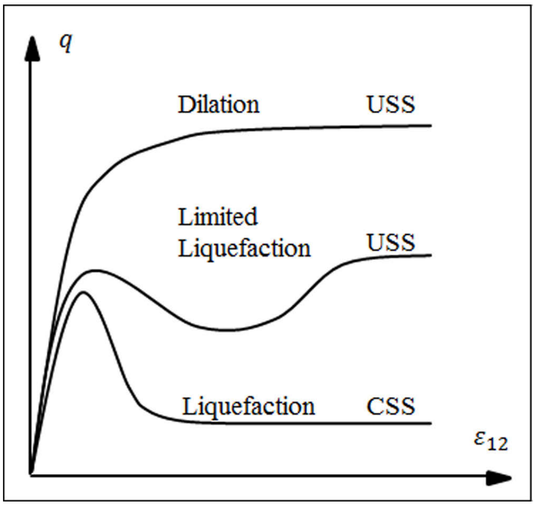

(a)

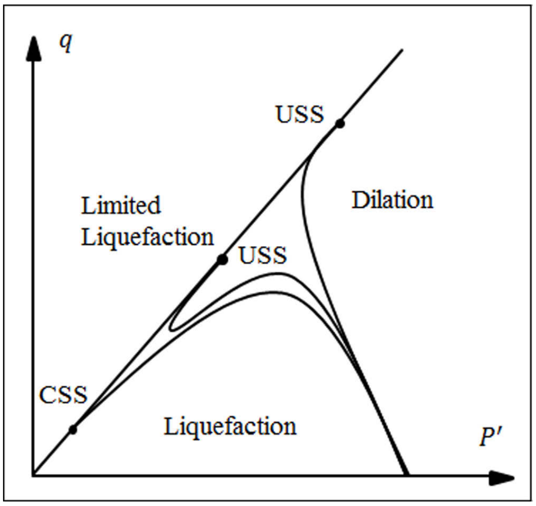

(b)

Figure 3.2: Three types of stress-strain behavior observed in undrained triaxial tests and undrained simple shear tests: (a) shear strain vs shear stress (b) mean principal stress vs shear stress. The shear stress q is equal to the difference between the first and the second principal stress. p' is the mean value of the first and the second principal stress.

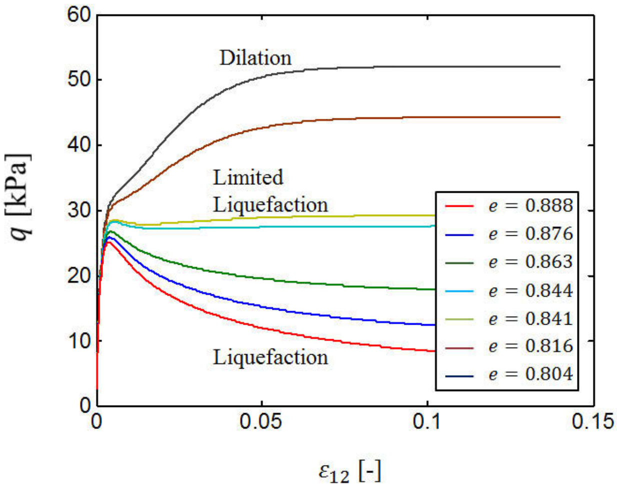

(a)

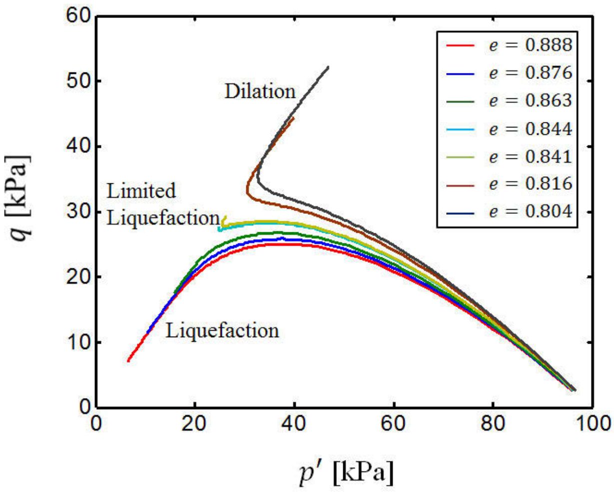

(b)

Figure 3.3: The simulation results of (3.16) for saturated sand with different initial void ratio in undrained simple shear tests: (a) shear strain vs shear stress (b) mean principal stress vs shear stress

Table 3.2: Parameters for e_{crt} and a in the simulation of the experiments in [101]

p_1	p_2	p_3	q_1	q_2	q_3
[-]	[-]	$[kPa^{-1}]$	[-]	[-]	$[kPa^{-1}]$
0.53	0.45	-0.0018	1.0	-0.4	-0.0001

which increase the density function I_e and limit the hardening. Conversely, in the softening regime, I_e will decrease to restrict softening and liquefaction. Due to the feedback of I_e, the model (3.16) can describe the shear softening and the residual strength of very loose granular materials. It can be used as the static portion of the new model for debris materials. As shown in Figure 3.4, the normal stresses $\sigma_{ii}(i = 1, 2, 3)$ of the very loose specimen with $e = 0.876$ tend to be isotropic when the shear strain is large enough, no matter what the initial stress state is. The isotropic normal stress at large deformation corresponds to the former mentioned thermodynamic pressure P_0.

3.3 The new constitutive model for debris materials

Based on the above analysis, the hypoplastic model (3.16) and the tensor form of the modified Bagnold's model are employed as the static and dynamic portions of the new constitutive model, respectively. The structure of the new model is proposed as

$$\mathbf{T} = \mathbf{T}_h + \mathbf{T}_d. \tag{3.22}$$

In Chapter 2, the three-dimensional form of the dynamic portion was developed as a part of the model (2.47). By eliminating the static portion from (2.47), the general 3-dimensional form of the dynamic portion is obtained as

$$\mathbf{T}_d = -\left(\frac{2K_1}{\tan\alpha_v}\sqrt{\mid II_D \mid} + \frac{4K_2}{\tan\alpha_i}\mid II_D \mid\right)\mathbf{1} + \left(2K_1 + 4K_2\sqrt{\mid II_D \mid}\right)\mathbf{D}^*. \tag{3.23}$$

It is shown that for a simple shear flow the dynamic stress (3.23) is reduced to the models (2.40) and (2.41).

From (3.22), the concrete model for debris materials is determined as

$$\begin{aligned}\mathbf{T} = \int \dot{\mathbf{T}}_h dt &- \left(\frac{2K_1}{\tan\alpha_v}\sqrt{\mid II_D \mid} + \frac{4K_2}{\tan\alpha_i}\mid II_D \mid\right)\mathbf{1} \\ &+ \left(2K_1 + 4K_2\sqrt{\mid II_D \mid}\right)\mathbf{D}^*\end{aligned} \tag{3.24}$$

where $\dot{\mathbf{T}}_h$ can be determined by (3.16).

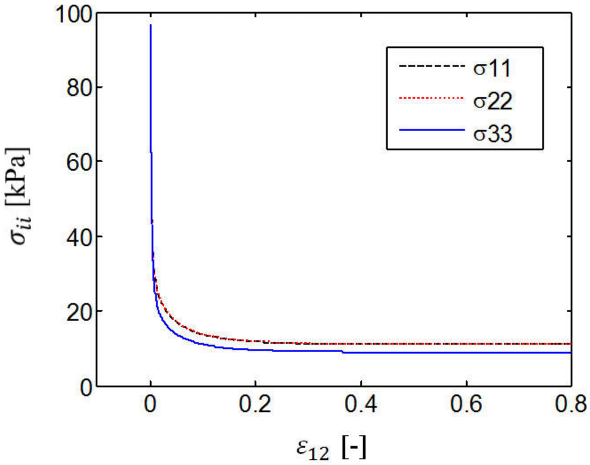

(a)

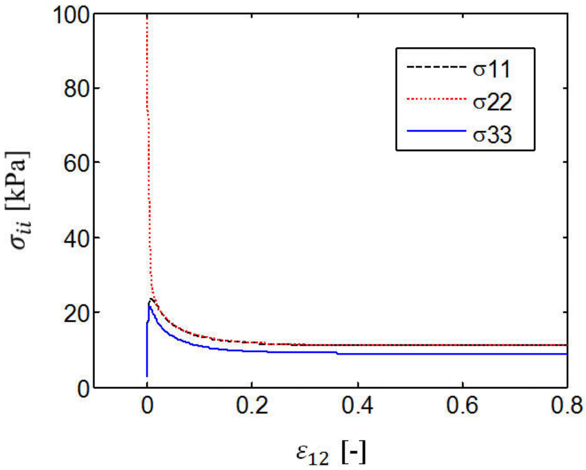

(b)

Figure 3.4: The normal stresses of the specimens with $e = 0.876$ in the undrained simple shear tests with different initial stress state: (a) $\sigma_{11} = \sigma_{22} = \sigma_{33} = 100kPa$, (b) $\sigma_{22} = 100kPa$ and $\sigma_{11} = \sigma_{33} = 1kPa$

The structure of the new model is demonstrated by simulating undrained simple shearing flow. As shown in Figure 3.5, the static portion obtained by the hypoplastic model (3.16) is combined with the dynamic portion to get the total effective stress.

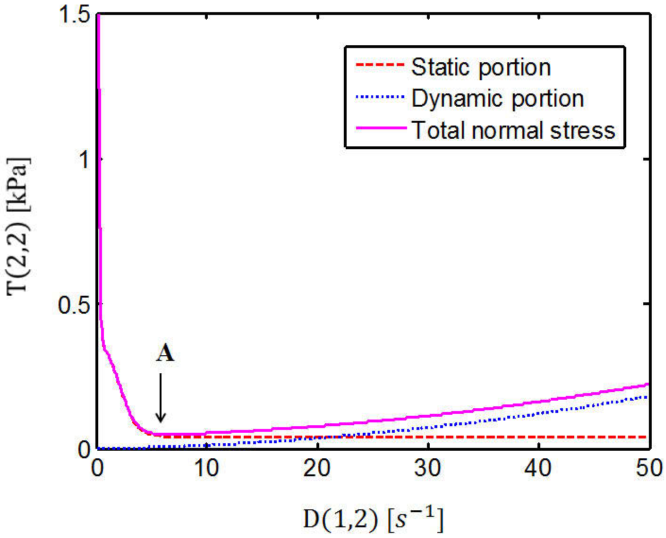

(a)

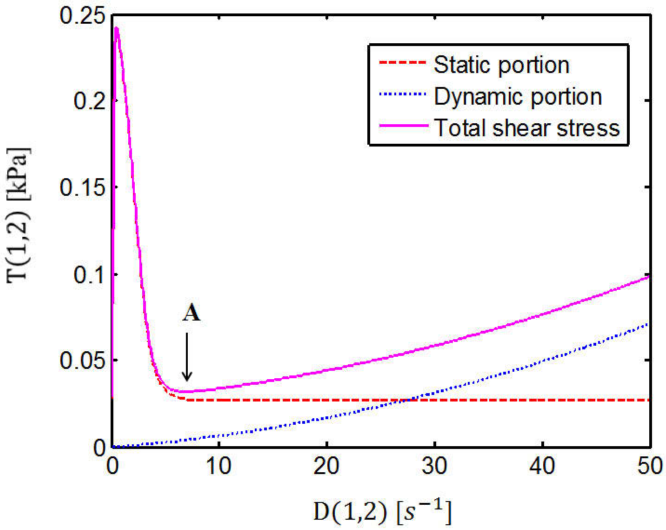

(b)

Figure 3.5: Schematics of the new model (3.24): (a) shear rate vs normal stress (b) shear rate vs shear stress

The proposed model bridges the solid-like and fluid-like behaviors of debris materials and describes the transition between solid and fluid state without any initiation criterion. The static and dynamic stress portions evolve concurrently depending on the flow state, the loading and boundary conditions. The assumptions in plasticity theory such as yield stress and strain decomposition are not required in the model. These features make the numerical implementation simplified.

What need to be mentioned is that the static portion, $\mathbf{T}_h$, is rate-independent. Stress is calculated due to the accumulation of the shear strain rather than the changing of the shear rate. By merging with the dynamic portion, the total effective stress (3.24) becomes rate-dependent. As shown in Figure 3.4, the normal stresses reach a residual constant when the shear strain is approximately 0.4. This quasi-static process takes place with very small shear velocity. Thus, in the simulation, the shear rate must be kept at a small value before the failure of the granular-fluid mixture to make sure that the static portion is the dominant part in the total effective stress. The static portion should be much greater than the dynamic portion at the point A in Figure 3.5. One approach to meet this requirement in numerical calculations is to use small shear strain acceleration for the stage before failure.

It is worth to mention that Wu [93] developed a rate form framework by combining a hypoplastic model and a rate-dependent dynamic model as

$$\overset{\circ}{\mathbf{T}} = \overset{\circ}{\mathbf{T}}_h(\mathbf{T}_h, \mathbf{D}) + \overset{\circ}{\mathbf{T}}_d(\mathbf{D}, \overset{\circ}{\mathbf{D}}). \tag{3.25}$$

where $\overset{\circ}{\mathbf{T}}$ is the total Jaumann stress rate tensor and $\overset{\circ}{\mathbf{T}}_d$ is the dynamic part of the Jaumann stress rate tensor. The models developed within this framework may have the capability to account for the different behaviors for loading and unloading. However, the Jaumann strain acceleration tensor, $\overset{\circ}{\mathbf{D}}$, makes the implementation of these models in some numerical methods more difficult. It will be an interesting exploration to solve this problem in our future work.

3.4 Performance of the proposed model

In this section, the new model, (3.24), will be used to predict the stress-strain behavior of granular-fluid flows with different materials and experimental apparatus in some element tests. The experimental data of two annular shear tests as undrained simple shear tests are employed to verify the applicability of the new model. In Chapter 2, these two experiments have been simulated by the model (2.47). The simulation results revealed that the contact stresses of the relatively loose granular materials decreased to residual stresses in the quasi-static stage and the normal stress P_0 cannot be treated as the weight component of the solid phase roughly in this case. The former simulation results are used as a control to highlight the capability of the hypoplastic portion in capturing shear softening.

3.4.1 Dry granular materials

The data for the spherical polystyrene beads with No. PS18 $\sim$ PS21 and diameter of 1.0 mm in [74] are selected for the element tests. The loads applied by the upper disk range from 100 to

1500 N/m^2 which is normal to the flow surface. By checking the measured normal stress for 1.0 mm beads, the initial confining pressure of an element at the upper surface of the specimen is assumed equal to 500 N/m^2. The value of C_∞ is equal to 0.64 which is a typical value for monosized spheres [34, 6]. Thus, the corresponding minimum void ratio

$$e_{min} = \frac{1 - C_\infty}{C_\infty} \tag{3.26}$$

is determined equal to 0.563. The critical volume fraction C_c is approximately 0.62 [75]. The internal friction angle ϕ_0 of 1.0 mm spherical beads is 23° and the initial tangent modulus E_i is assumed equal to 15 MPa as a typical value of loose granular materials with the confining pressure is 100 kPa. Based on the identification of parameters introduced before, the material constants $c_1 \sim c_4$ and the parameters for the density function I_e are determined and listed in Table 3.3.

Table 3.3: Parameters for the static portion in the simulation of dry granular flows

c_1 [-]	c_2 [-]	c_3 [-]	c_4 [-]	e_{min} [-]	p_1 [-]	p_2 [-]	p_3 [kPa^{-1}]	q_1 [-]	q_2 [-]	q_3 [kPa^{-1}]
-50	-746.55	-746.55	1855.13	0.563	0.65	0.55	-0.11	1.0	-0.24	-0.013

The stress ratios in the fast shearing stage, $\tan\alpha_i$, are chosen as a constant of 0.51 based on the experimental results for the four specimens, which correspond to a α_i of about 27°. The parameters for the dynamic portion are listed in Table 2.2 and Table 3.4.

Table 3.4: Parameters for the dynamic portion in the simulation of dry granular flows

d [mm]	C_∞ [-]	C_c [-]	ρ_s [kg/m^3]	μ [$Pa \cdot s$]	α_i [°]
1.0	0.64	0.62	1095	1.83×10^{-5}	27

As shown in Figure 3.6, the predicted results are in good agreement with the experimental data even though typical values rather than fitted values are employed for some parameters unstated in [74]. Following Savage and Sayed [74], the non-dimensional shear rate and stress are employed in the figures. The non-quadratic dependence between the stresses and strain rate in the slow shear stage for the samples with $C = 0.524$ is captured by the new model. As introduced in Chapter 2, the shear velocity of this experiment was adjusted to keep the height constant, thereby keeping the volume of the samples unchanged. It is equivalent to the undrained condition in the tests of saturated granular materials. The mean effective stress would decrease from the initial confining pressure to a residual value or zero to stop the tendency of volume compression in the quasi-static stage of very loose granular-fluid mixture. The residual normal and shear stresses, corresponding to the stresses P_0 and T_0 in the framework (2.10), are determined by the hypoplastic portion and presented in Table 3.5. Only the test with $C = 0.524$ demonstrates residual strength. In this case, the frictional contacts and collisions contribute to the stress development simultaneously. At low shear rate, frictional contact is significant, resulting in non-zero residual stress. As the shear rate increases, the stress from collision becomes larger. At high shear rate, although the magnitude of the frictional stress is unchanged, its proportion in the total stress declines. For the looser specimens with $C = 0.504$, 0.483 and 0.461, the frictional contacts vanish at large shear strain. This is consistent with the experimental observation [101] that granular materials will be fully liquefied when the initial void ratio exceeds a threshold. As a consequence, only particle collisions contribute to the stress in the flow stage. The stress-strain rate curves in the flow stage show a slope of 2 in the logarithmic coordinates. It implies that the linear terms T_v and P_v which characterize the effect of the interstitial fluid are insignificant in the dry granular case, which is consistent with the analysis in Section 2.2. It confirms that the proposed model (3.24) can describe the shear softening of dry granular materials in the quasi-static stage. The stress-shear rate relation throughout the shear process from quasi-static stage to fast shearing stage also can be exactly described by the new model.

Table 3.5: The residual stresses of the four samples of dry granular flow determined by the hypoplastic model

Solid volume fraction, C [-]	0.461	0.483	0.504	0.524
Initial void ratio, e [-]	1.17	1.07	0.98	0.91
P_0 $[Pa]$	0	0	0	81
T_0 $[Pa]$	0	0	0	36

3.4.2 Granular-water mixture

For the case of a granular-fluid mixture, Hanes & Inman's experiments [34] about spherical particles sheared in water are taken as an example again. The data for particles with diameter 1.85 mm are chosen to verify the new model. The maximum measured volume fraction for 1.85 mm particles was reported to be 0.55. Thus the asymptotic limit C_∞ is presumed to be approximately 0.61 and the corresponding minimum void ratio is 0.64. The load from the upper disk is about 500 N/m^2. The internal friction angle ϕ_0 is stated to be 28° and the initial

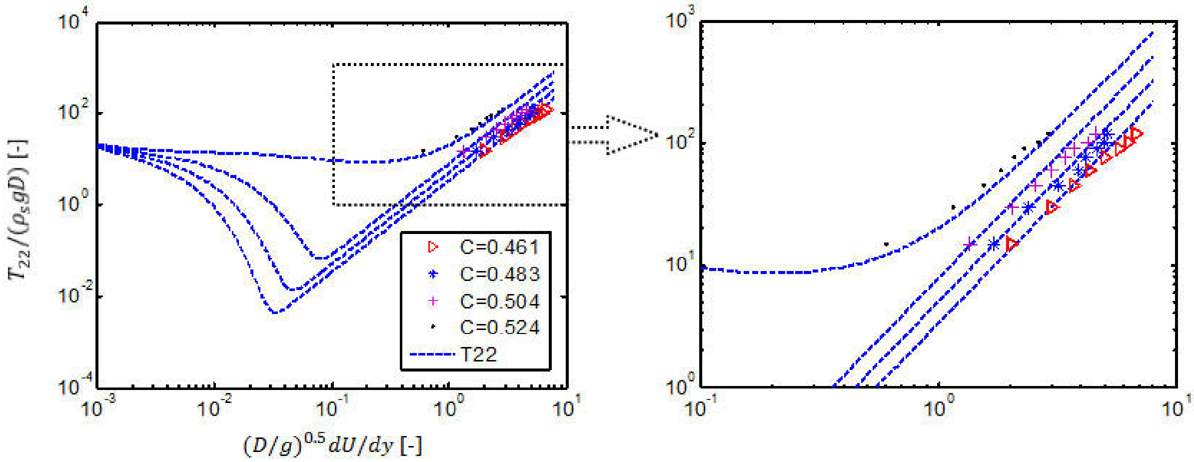

(a)

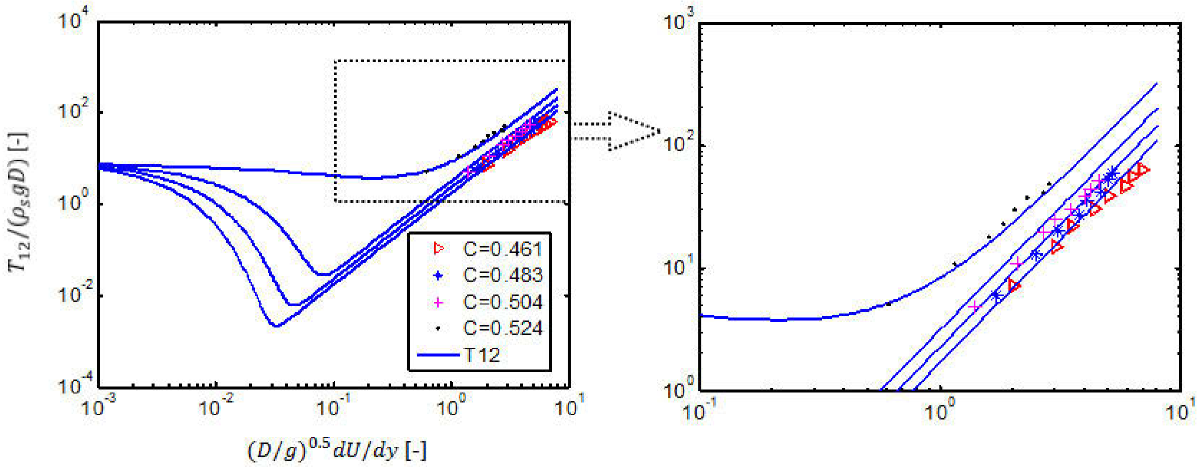

(b)

Figure 3.6: Element test results for the dry granular flow with different grain linear concentration: (a) shear rate vs normal stress (b) shear rate vs shear stress. The experimental data are indicated by various symbols. The dashed lines denote the normal stresses while the solid lines for the shear stresses.

tangent modulus E_i is 15 MPa. The determined material constants $c_1 \sim c_4$ and the parameters for the density function I_e are presented in Table 3.6.

Table 3.6: Parameters for the static portion in the simulation of granular-fluid flows

c_1	c_2	c_3	c_4	e_{min}	p_1	p_2	p_3	q_1	q_2	q_3
[-]	[-]	[-]	[-]	[-]	[-]	[-]	$[kPa^{-1}]$	[-]	[-]	$[kPa^{-1}]$
-50	-511.31	-511.31	680.53	0.64	0.65	0.55	-0.11	1.0	-0.12	-0.013

The stress ratios $\tan\alpha_i$ for all the specimens are equal to 0.59, corresponding to a α_i of about 30.5°.The parameters of the dynamic portion are listed in Table 2.4 and Table 3.7.

Table 3.7: Parameters for the dynamic portion in the simulation of granular-fluid flows

d	C_∞	C_c	ρ_s	μ	α_i
$[mm]$	[-]	[-]	$[kg/m^3]$	$[Pa \cdot s]$	[°]
1.85	0.61	0.52	2780	1.0×10^{-3}	30.5

The simulation results are shown in Figure 3.7. The stress states of the two specimens are reproduced based on the residual stresses as presented in Table 3.8. The sample with $C = 0.51$ shows a residual strength after failure in the undrained simple shearing and the looser sample shows full liquefaction. The stress-shear rate curves of $C = 0.49$ have a slope less than 2 in the stage with shear rate between 1 to 10 s^{-1} in the logarithmic coordinates. Comparing to the dry granular flows, the effect of the interstitial fluid in a granular-fluid flow is non-negligible. In the rapid shear stage, there is slight difference between the slopes of predicted curves and the experimental data of $C = 0.49$ which implies that the residual strength of this specimen is non-zero. The underestimate of the residual stresses may be attributed to that inaccurate parameters are employed for the hypoplastic model.

Table 3.8: The residual stresses of the two samples of ganular-fluid flow determined by the hypoplastic model

Solid volume fraction, C [-]	0.49	0.51
Initial void ratio, e [-]	1.04	0.96
P_0 $[Pa]$	0	173
T_0 $[Pa]$	0	102

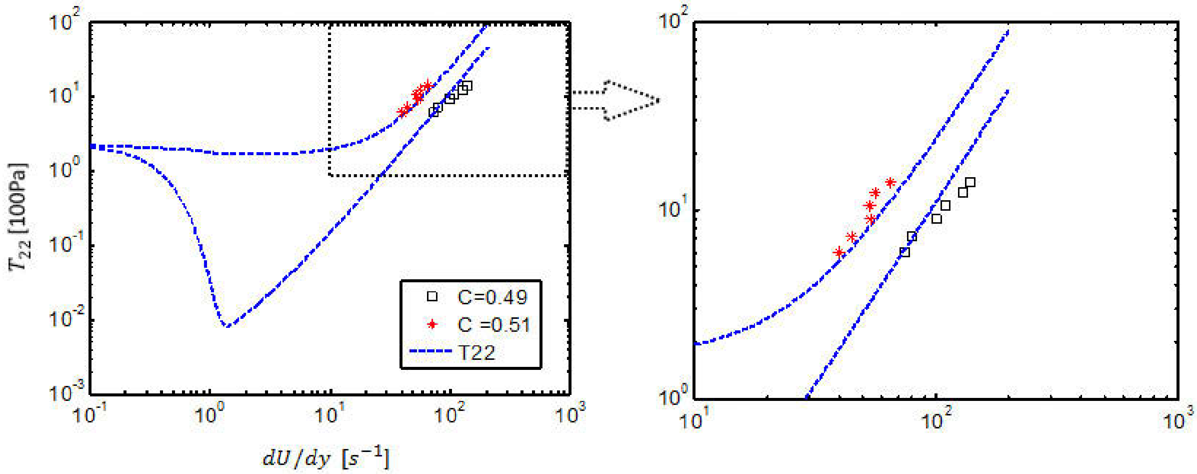

(a)

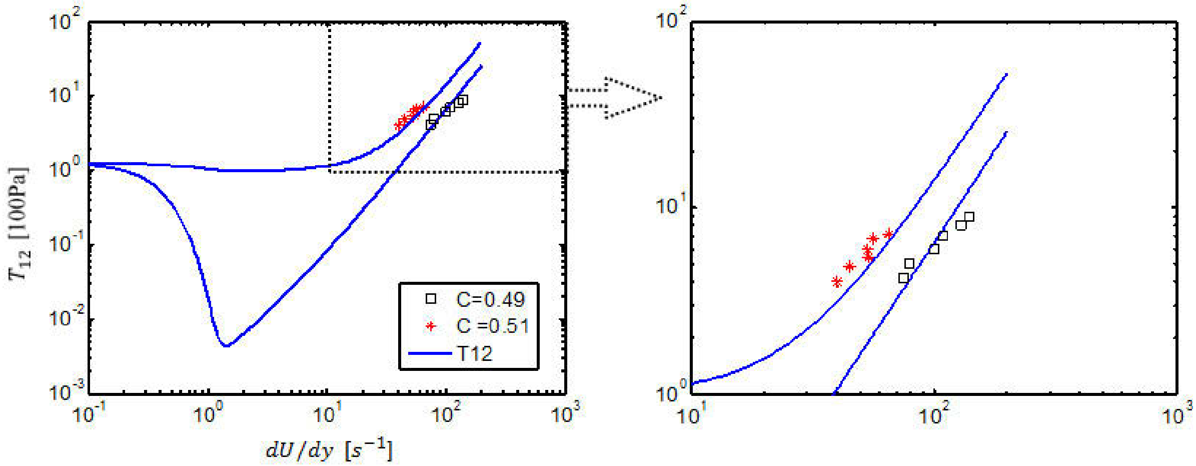

(b)

Figure 3.7: Element test results for the granular-water flows with different solid volume fraction: (a) shear rate vs normal stress (b) shear rate vs shear stress. The experimental data are indicated by various symbols. The solid lines denote the shear stresses and the dashed lines are the normal stresses.

Chapter 4

Verification of the new model by smoothed particle hydrodynamics method

The new constitutive model for debris materials, (3.24), needs to be implemented in numerical methods and further verified in the simulations of some boundary value problems. Smoothed particle hydrodynamics (SPH) method which is ideal for modelling both solid-like and fluid-like behaviors within a consistent numerical scheme is used for the numerical simulations in this chapter.

4.1 Introduction of SPH method

With the development of computer technology, computer simulation has become one of the most important tools for solving complicated and practical problems in engineering and science. Numerical methods are usually classified into two categories, the traditional grid-based methods and the mesh-free methods, based on the different treatments of the problem domains. The grid or mesh based numerical methods such as the finite element method (FEM), the finite differential method (FDM) and the finite volume methods (FVM) are widely applied to solve problems in the areas of computational solid mechanics (CSM) and computational fluid dynamics (CFD) [56]. The common feature of grid-based numerical methods is that a continuum problem domain will be divided into discrete small subdomains in the simulation by the process termed as discretization or meshing. Despite the great success of the grid based methods, the existence of the grid or mesh limits the application in the problems with free surface, deformable boundary, moving interface, and extremely large deformation and so on [56]. Moreover, for the problem domain with complicated geometry, it is very difficult to generate a quality mesh. The Lagrangian grid-based methods, such as FEM, need special techniques like rezoning to deal with large deformation problem, which is tedious and time-consuming, and may result in inaccurate solution [54, 56, 103]. In addition, the grid-based methods are also considered to be unsuitable for the simulation of discrete systems [1, 35], such as granular materials.

For solving the former mentioned complicated problems, the mesh-free methods have become the research focus during the past decades. Numerous mesh-free methods have been proposed, which bear advantages compared to the traditional grid-based methods in the simulation of large deformation, free surface etc., due to the abandonment of mesh [66]. SPH can be regarded as the oldest modern mesh-free particle method which was first developed to solve astrophysical problems in three-dimensional space [27, 56]. It is a Lagrangian mesh-free method, where the continuum is represented by a set of particles possessing field variables (e.g., position, density, velocity, stress and strain) and moving with the material velocity [14, 66]. In the simulation using SPH, a method termed as function approximation is applied to the partial differential equations (PDEs) of the continuum to produce a set of ordinary differential equations (ODE) in a discretized form with respect only to time [55]. The ODE can be solved by one of the standard integration routines of the conventional finite difference method. For finishing the these processes, the following key ideas should be employed in the SPH method [55].

1. The problem domain is represented by a set of particles between which no connectivity is needed.

2. The field function approximation is finished by using the integral representation method, which is termed as kernel approximation in SPH.

3. The integration in the integral representation of the field function and its derivatives are replaced by the summations over all the corresponding values at the particles in a local domain called the support domain. This process is termed as particle approximation in SPH.

4. In the process of particle approximation at every time step, the number and location of the particles in the support domain are changing since the current local distribution of the particles is changing with time.

5. All terms related to field functions in the PDEs are approximated using particles to produce a set of ODEs.

6. The ODEs are then solved using an explicit integration algorithm to achieve fast time stepping, and to obtain the time history of all the field variables for all the particles.

As summarized by Liu [56], SHP has the following advantages compared to the traditional grid-based methods. 1) The advection and transport of the system can be calculated since the inside algorithm of SPH is Galilean invariant, and thus the time history of the material particles can be obtained. 2) The free surface, material interfacial and moving boundaries can all be traced naturally in the simulation by SPH when the particles at specific position are deployed properly in the pretreatment stage. 3) As a traditional and mature mesh-free method, SPH allows a direct handling of large deformation problems, since the connectivity between particles are generated as part of the computation and changing with time. 4) SPH can be used for small and multiple scale problems, such as that in biophysics and biochemistry, since it is similar to the molecular dynamics (MD) method and the dissipative particle dynamics (DPD) method which are traditional methods for small scales.5) SPH is suitable for the problems with micro scale or astronomic scale, where the research object cannot be treated as a continuum. 6) SPH is more natural to develop three-dimensional simulation than grid-based methods.

Based on these advantages, SPH has been applied extensively to a vast range of problems in either computational fluid or solid mechanics. Beside the application in astrophysics, SPH is also applied to solid problems such as dynamic analysis [53], impact [44] and explosion simulations [57], which verified the applicability of SPH for the multiscale problems. Granular materials show solid-like behavior before failure and fluid-like behavior after failure which lead to a typical multiscale problem.

4.2 SPH modelling of granular material

Now we try to implement the new model (3.24) in SPH to simulate some granular flows. Since the hydro-mechanical coupling still needs further investigation to be considered in the numerical model, all the following simulations by SPH are focused on dry granular flows. In this case, for simplifying the numerical calculations, the new model (3.24) is reduced to

$$\mathbf{T} = \int \dot{\mathbf{T}}_h dt - \frac{4K_2}{\tan \alpha_i} \mid II_D \mid \mathbf{1} + 4K_2 \sqrt{\mid II_D \mid}\mathbf{D}^* \tag{4.1}$$

by eliminating the negligible viscous terms. Nevertheless, the structure of the unified model where a hypoplastic model is combined with a rheological model is well retained in (4.1), which is the primary objective of the simulations of granular flows. In addition, the applicability and stability of hypoplasticity in the simulations of multiscale deformation problems, which is the main content of this thesis, can be tested by employing either (3.24) or (4.1). As introduced in Section 3.3, the following elements are not required in our unified model, i.e. initiation criterion, yield stress and strain decomposition, which simplify the numerical implementation. The parameter K_2 is related to the particle density, particle diameter and solid volume fraction. It is a constant when the volume remains unchanged. In this chapter, K_2 is given directly as a measured parameter for the element tests by SPH.

As stated before, SPH is a Lagrangian mesh-free method where the whole computational domain Ω is discretized with a set of particles. By tracking the movement of the particles and the evolution of the carried variables, the considered problem can be solved numerically. Because the SPH uses an updated Lagrangian formulation, large deformation problems in solid mechanics as well as free surface tracking in fluid dynamics are treated naturally. Debris flow is simplified to granular flow in the constitutive modelling and typically involving large deformation and free surface problems. The mesh-free and Lagrangian properties of SPH make it an appealing method for granular flow modelling [14, 16, 18, 66].

4.2.1 The governing equations

In the case of dry granular flows, the interstitial fluid, air, is ignored and the granular materil is modelled as single phase medium. The governing equations for granular flows in the Lagrangian description take the form

$$\frac{\mathrm{d}\rho}{\mathrm{d}t} = -\rho\nabla\cdot\boldsymbol{v} \tag{4.2}$$

$$\frac{\mathrm{d}\boldsymbol{v}}{\mathrm{d}t} = \frac{1}{\rho}\nabla\mathbf{T} + \boldsymbol{g} \tag{4.3}$$

where $\mathrm{d}(\cdot)/\mathrm{d}t$ is the material derivative, ρ is the density of the continuous medium, and $\boldsymbol{g}$ is the body force. The governing equations consist of conservation of mass (4.2) and momentum (4.3).

4.2.2 The SPH formulations

Based on the former mentioned key ideas employed in SPH, the formulation of SPH contains two key steps, the integral representation (or the kernel approximation) of field functions and the particle approximation.

(a) The integral representation

The concept of integral representation of an arbitrary function $F(\boldsymbol{x})$ in SPH is inspired from the following formula where the function $F(\boldsymbol{x})$ is represented in an integral form as

$$F(\boldsymbol{x}) = \int_\Omega F(\boldsymbol{x}')\delta(\boldsymbol{x}-\boldsymbol{x}')\mathrm{d}\boldsymbol{x}' \tag{4.4}$$

where $\boldsymbol{x} = (x, y, z)$ is a spatial point in the volume of the integral Ω, and $\delta(\boldsymbol{x} - \boldsymbol{x}')$ is the Dirac delta function defined by

$$\delta(\boldsymbol{x} - \boldsymbol{x}') = \begin{cases} 1 & \boldsymbol{x} = \boldsymbol{x}' \\ 0 & \boldsymbol{x} \neq \boldsymbol{x}'. \end{cases} \tag{4.5}$$

In the integral representation in SPH, the Dirac delta function is replaced by a smoothing function $W(\boldsymbol{x} - \boldsymbol{x}', h)$ which is termed as kernel function (or smoothing kernel function). Thus, the kernel approximation of the field function $f(\boldsymbol{x})$ is expressed as

$$f(\boldsymbol{x}) \doteq \int_{\Omega} f(\boldsymbol{x}') W(\boldsymbol{x} - \boldsymbol{x}', h) \mathrm{d}\boldsymbol{x}', \tag{4.6}$$

where h is the smoothing length determining the influence area, i.e. the support domain of the function W. The kernel function W is normally an even function which satisfies the following conditions.

The first one is stated as

$$\int_{\Omega} W(\boldsymbol{x} - \boldsymbol{x}', h) \mathrm{d}\boldsymbol{x}' = 1, \tag{4.7}$$

which is termed as the normalization condition or unity condition.

The second condition is formulated as

$$\lim_{h \to 0} W(\boldsymbol{x} - \boldsymbol{x}', h) = \delta(\boldsymbol{x} - \boldsymbol{x}') \tag{4.8}$$

and termed the Delta function property.

The third condition is the so-called compact condition formulated as

$$W(\boldsymbol{x} - \boldsymbol{x}', h) = 0 \quad \text{when } |\ \boldsymbol{x} - \boldsymbol{x}'\ | > kh \tag{4.9}$$

where k is a constant which determines the support domain of the kernel function of point $\boldsymbol{x}$ together with the smoothing length h.

These three conditions imply that the integral representation in equation (4.6) can only be an approximation unless the kernel function W is the Dirac delta function δ. In SPH, the angle bracket $<>$ is conventionally used to mark the kernel approximation operator. Therefore, equation (4.6) can be rewritten as

$$< f(\boldsymbol{x}) >= \int_{\Omega} f(\boldsymbol{x}') W(\boldsymbol{x} - \boldsymbol{x}', h) \mathrm{d}\boldsymbol{x}'. \tag{4.10}$$

The kernel function W used through this paper is a Wendland C^6 function [22, 90] for which the support domain has a radius of $2h$.

The approximation for field function's spatial derivative is obtained by substituting $\nabla f(\boldsymbol{x})$ into Eq. (4.10), which gives

$$< \nabla f(\boldsymbol{x}) >= \int_{\Omega} [\nabla f(\boldsymbol{x}')] W(\boldsymbol{x} - \boldsymbol{x}', h) \mathrm{d}\boldsymbol{x}'. \tag{4.11}$$

Since

$$[\nabla f(\boldsymbol{x}')] W(\boldsymbol{x} - \boldsymbol{x}', h) = \nabla [f(\boldsymbol{x}') W(\boldsymbol{x} - \boldsymbol{x}', h)] - f(\boldsymbol{x}') \nabla W(\boldsymbol{x} - \boldsymbol{x}', h), \tag{4.12}$$

equation (4.11) is changed into

$$< \nabla f(\boldsymbol{x}) >= \int_{\Omega} \nabla [f(\boldsymbol{x}') W(\boldsymbol{x} - \boldsymbol{x}', h)] \mathrm{d}\boldsymbol{x}' - \int_{\Omega} f(\boldsymbol{x}') \nabla W(\boldsymbol{x} - \boldsymbol{x}', h) \mathrm{d}\boldsymbol{x}'. \tag{4.13}$$

Based on the divergence theorem, the first term on the right-hand side of (4.13) can be converted into an integral over the surface S of the domain, Ω. Thus, equation (4.13) is further converted into

$$< \nabla f(\boldsymbol{x}) >= \int_{S} f(\boldsymbol{x}') W(\boldsymbol{x} - \boldsymbol{x}', h) \cdot \boldsymbol{n} \mathrm{d}S - \int_{\Omega} f(\boldsymbol{x}') \nabla W(\boldsymbol{x} - \boldsymbol{x}', h) \mathrm{d}\boldsymbol{x}' \tag{4.14}$$

where $\boldsymbol{n}$ is the unit normal vector of the surface S. Since the function W is defined to have compact support, the integral over the surface S is identically zero when the support domain is located within the probelm domain. Therefore, the approximation for $\nabla f(\boldsymbol{x})$ is expressed as

$$< \nabla f(\boldsymbol{x}) >= - \int_{\Omega} f(\boldsymbol{x}') \nabla W(\boldsymbol{x} - \boldsymbol{x}', h) \mathrm{d}\boldsymbol{x}'. \tag{4.15}$$

It can be seen that the differential operation of the field function $f(\boldsymbol{x})$ is turned into the differential operation of the kernel function W by equation (4.15).

(b) The particle approximation

In the SPH method, the studied continuum is represented by a set of particles possessing specific mass and volume. It is fulfilled by the second key step, the particle approximation. In this step, the continuous integral representations of the filed functions and their derivatives can be converted into discretized forms of summation over all the particles in the support domain. Let's consider a specifc particle i which has an associated kernel function W_i centred at $\boldsymbol{x}_i$. The continuous integrations in Eq. (4.10) and (4.15) are written as

$$< f(\boldsymbol{x}_i) >= \sum_{j=1}^{n} f(\boldsymbol{x}_j) W_{ij} \frac{m_j}{\rho_j} \tag{4.16}$$

$$< \nabla f(\boldsymbol{x}_i) >= \sum_{j=1}^{n} f(\boldsymbol{x}_j) \nabla_i W_{ij} \frac{m_j}{\rho_j} \tag{4.17}$$

where n is the number of particles within the support domain of particle i; m_j and ρ_j are the mass and density of particle j, respectively; thus, m_j/ρ_j denotes the volume occupied by particle j; the kernel function concerning the location $\boldsymbol{x}_i$ is expressed as

$$W_{ij} = W(\boldsymbol{x}_i - \boldsymbol{x}_j, h); \tag{4.18}$$

$\nabla_i W_{ij}$ is the gradient of kernel function W_{ij} and expressed as

$$\nabla_i W_{ij} = \frac{\boldsymbol{x}_i - \boldsymbol{x}_j}{r_{ij}} \frac{\partial W_{ij}}{\partial r_{ij}} \tag{4.19}$$

in which r_{ij} is the distance between particle i and particle j. Through SPH simulations the mass of a particle is usually constant but its density can evolve according to the varying of inter-particle spacing, resulting to constantly changing particle volume.

Many particle discretization forms of the governing equations are available in the SPH literature. By numerical experiments, we find that the following expressions give rise to better results

$$\frac{\mathrm{d}\rho_i}{\mathrm{d}t} = \sum_{j=1}^{n} m_j(\boldsymbol{v}_i - \boldsymbol{v}_j) \cdot \nabla_i W_{ij} \tag{4.20}$$

$$\frac{\mathrm{d}\boldsymbol{v}_i}{\mathrm{d}t} = \sum_{j=1}^{n} \left(\frac{\mathbf{T}_i}{\rho_i^2} + \frac{\mathbf{T}_j}{\rho_j^2} \right) \nabla_i W_{ij} m_j + \boldsymbol{g}_i \tag{4.21}$$

where $\mathbf{T}$ is the total effective stress tensor, consisting of the hypoplastic stress portion and the dynamic stress portion.

The calculation of stress rate in the proposed constitutive relation requires the velocity gradient, which can be computed in the SPH as

$$\nabla \boldsymbol{v}_i = \sum_{j=1}^{n} (\boldsymbol{v}_j - \boldsymbol{v}_i) \otimes \nabla_i W_{ij} \frac{m_j}{\rho_j} \tag{4.22}$$

4.2.3 The correction of kernel gradient

The continuous SPH kernel interpolation in Eq. (4.10) theoretically ensures second order accuracy for interior regions. That is, constant and linear functions can be reproduced exactly. However, this C^0 and C^1 consistency are not always satisfied in the SPH particle approximation, especially when particle distributions are irregular, or the particle support domain is truncated by boundaries [56]. This deficiency, termed particle inconsistency, is the direct cause of the relatively low accuracy and slow convergence rate in the original SPH method. Usually the lack of C^1 consistency is more hazardous, because the discrete forms of the governing equations Eq. (4.20) and (4.21) all make use of the kernel gradient ∇W. Many corrections have been proposed to improve the accuracy of kernel gradient approximation. In the present study, we use the renormalization technique [12, 65] to enforce the C^1 consistency, which is briefly given as follows.

The gradient of the field function $f(\boldsymbol{x})$ can be rewritten as

$$\nabla f(\boldsymbol{x}) = \nabla f(\boldsymbol{x}) - f(\boldsymbol{x})\nabla 1 \tag{4.23}$$

The continuous kernel approximation of the above equation reads

$$< \nabla f(\boldsymbol{x}) >= \int_\Omega f(\boldsymbol{x}')\nabla W \mathrm{d}\boldsymbol{x}' - f(\boldsymbol{x})\int_\Omega \nabla W \mathrm{d}\boldsymbol{x}' \tag{4.24}$$

Performing the second order Taylor expansion to the first term on the right-hand side of Eq. (4.24), we have

$$\int_\Omega f(\boldsymbol{x}')\nabla W \mathrm{d}\boldsymbol{x}' = f(\boldsymbol{x})\int_\Omega \nabla W \mathrm{d}\boldsymbol{x}' + \left(\int_\Omega (\boldsymbol{x}' - \boldsymbol{x}) \otimes \nabla W \mathrm{d}\boldsymbol{x}'\right)\nabla f(\boldsymbol{x}) + O(h^2) \tag{4.25}$$

Substituting the above equation into Eq. (4.24) gives

$$< \nabla f(\boldsymbol{x}) >= \left(\int_\Omega (\boldsymbol{x}' - \boldsymbol{x}) \otimes \nabla W \mathrm{d}\boldsymbol{x}'\right)\nabla f(\boldsymbol{x}) + O(h^2) \tag{4.26}$$

From Eq. (4.26) we can see that the kernel approximations of function gradient have second order accuracy when the following requirement is satisfied:

$$\int_\Omega (\boldsymbol{x}' - \boldsymbol{x}) \otimes \nabla W \mathrm{d}\boldsymbol{x}' = \begin{pmatrix} 1 & 0 \\ 0 & 1 \end{pmatrix} \tag{4.27}$$

In order to ensure the C^1 consistency in the SPH method, the above requirement needs to be satisfied in discrete particle approximation. This is achieved using the renormalization technique, which employs the corrected kernel gradient $\nabla^C W$ such that at particle i

$$\sum_{j=1}^{n} (\boldsymbol{x}_j - \boldsymbol{x}_i) \otimes \nabla_i^C W_{ij} \frac{m_j}{\rho_j} = \begin{pmatrix} 1 & 0 \\ 0 & 1 \end{pmatrix} \tag{4.28}$$

where $\nabla_i^C W_{ij} = \boldsymbol{L}(\boldsymbol{x}_i)\nabla_i W_{ij}$ denotes the corrected kernel gradient at particle i. $\boldsymbol{L}$ is the renormalization matrix in the following form

$$\boldsymbol{L}(\boldsymbol{x}_i) = \begin{pmatrix} \sum_{j=1}^{n}(x_j - x_i)\frac{\partial W_{ij}}{\partial x_i}\frac{m_j}{\rho_j} & \sum_{j=1}^{n}(x_j - x_i)\frac{\partial W_{ij}}{\partial y_i}\frac{m_j}{\rho_j} \\ \sum_{j=1}^{n}(y_j - y_i)\frac{\partial W_{ij}}{\partial x_i}\frac{m_j}{\rho_j} & \sum_{j=1}^{n}(y_j - y_i)\frac{\partial W_{ij}}{\partial y_i}\frac{m_j}{\rho_j} \end{pmatrix}^{-1} \tag{4.29}$$

The corrected kernel gradient ∇W^C is applied to the Eqs. (4.20), (4.21) and (4.22), replacing the original kernel gradient ∇W. The employment of the corrected gradient kernel ensures the C^1 consistency in the SPH method.

4.2.4 Numerical implementation and boundary conditions

In the SPH method, the solution of granular flow problems is obtained by marching Eq. (4.20) and (4.21) forward in time starting from initial conditions. Many explicit integration methods are available for this task. In this thesis, we employ a Predictor-Corrector scheme [28]. The time step of the explicit solver is controlled by a combination of the Courant condition and the maximum acceleration [66]

$$\Delta t = \chi_{CFL} \min \left(\frac{h}{\max \parallel \boldsymbol{a}_i \parallel}, \frac{h}{c} \right) \tag{4.30}$$

where $\boldsymbol{a}_i = \mathrm{d}\boldsymbol{v}_i/\mathrm{d}t$ is the particle acceleration, c is the artificial speed of sound used to control the size of the time step, and χ_{CFL} is the Courant condition coefficient. In this thesis c and χ_{CFL} are taken as 80 m/s and 0.05, respectively.

In the unified model, the hypoplastic stress part is history-dependent. Therefore, the hypoplastic stress tensor $\mathbf{T}_h$ is calculated by integrating hypoplastic stress rate $\dot{\mathbf{T}}_h$ using the same Predictor-Corrector scheme. As long as the time step is small enough, the direct stress integration of the hypoplastic stress is accurate sufficiently [66]. Since there is no explicit failure in hypoplasticity, complex stress integration and return-mapping algorithms in elastoplasticity are unnecessary.

Two kinds of boundary conditions are considered in this chapter, i.e. periodic boundary and non-slip solid boundary. The periodic boundary condition in SPH is straightforward, as shown in [16, 28]. The treatment of solid boundary condition is still a challenge in SPH computations. In the following simulations, a boundary particle method developed for geomechanical applications [67] is employed. In this method, the solid boundary is discretized with boundary particles, which take part in the SPH approximation like real particles but keep fixed or move with prescribed motions. The velocity and stress tensor at boundary particles are extrapolated from the real granular particles. It is found that this boundary treatment method works properly in our simulations.

4.3 SPH element tests

In this section, the implementation of the unified constitutive model in SPH is validated using two element tests. Their analytical solutions have been presented in Section 3.2 and Section 3.4, respectively. By comparing the analytical and numerical results, we can show whether the model is well implemented in the SPH code. For simplicity, velocity restrictions are imposed on SPH particles to reproduce a uniform deformation condition in the test, analogous to an element test in the FEM.

4.3.1 Quasi-static undrained simple shear test

The static portion of the unified model as well as the SPH method are tested at first by simulating the undrained simple shear test in Section 3.2 which is within the quasi-static deformation range. In real applications, the accurate modelling of the former mentioned three types of stress-strain behavior is crucial because it determines whether a subsequent material flow occurs. The computational setup is shown in Figure 4.1, with a size of 0.1×0.1 m. Periodic boundary conditions are applied to reproduce a uniform shear deformation, where arbitrary large shear strain can be modelled. The undrained condition is simulated by keeping the volume fixed. Pore water is not considered, so all stresses presented in the analysis are effective stress. The constitutive parameters given in Table 3.1 and Table 3.2 are employed. The parameters K_2 and α_i for the flow range are assumed, because the experiments are only performed with quasi-static loading. Although K_2 depends on the initial void ratio, it assumed as an constant of 0.01 since the dynamic part is insignificant when shear rate is low. α_i is assumed equal to $35.0°$.

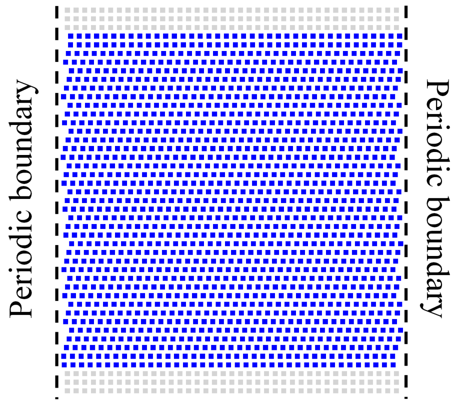

Figure 4.1: Computational setup for the undrained simple shear test. Granular particles and boundary particles are marked blue and gray.

A velocity field of $v_x = 0.01z$ m/s and $v_z = 0$ m/s is imposed on the particles as boundary condition for the element test, which corresponds to a constant shear rate of $\dot{\varepsilon}_{xz} = 0.5$ %/s, larger than that in the experiments. However, with the applied shear rate the dynamic stress part is sufficiently small ($\sim 10^{-7}$ Pa), so that the simulation lies in the quasi-static range. Five simulations with different initial void ratios are performed with a confining pressure $p_0 = 100$ kPa. The numerical results are given in Figure 4.2. The simulation successfully captures the sand behaviors in the quasi-static simple shear tests. The three types of stress-strain relations are well reproduced. Comparing to the analytical solutions shown in Figure 3.3 where the dynamic portion is not taken into account, almost the same results are obtained in the SPH simulations since the dynamic stress is negligibly small in the low shear rate condition. It confirms that the unified model is well implemented in the SPH numerical model and can be used to simulate the static behaviors of granular materials.

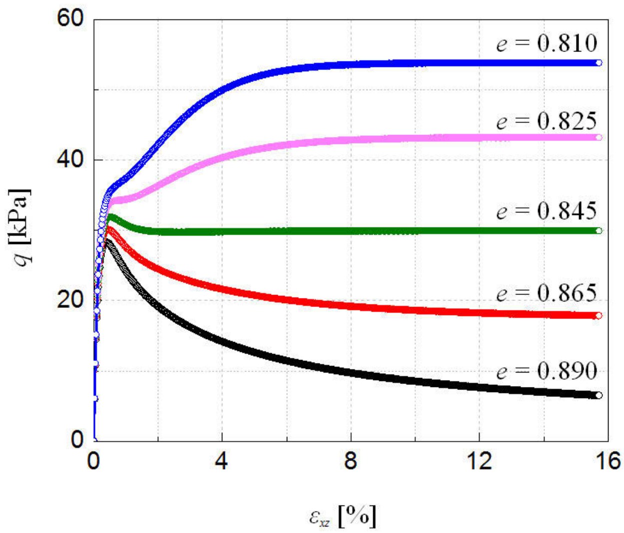

(a)

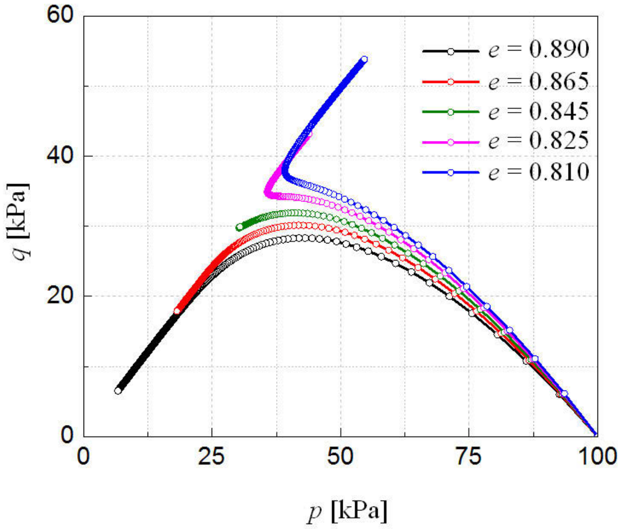

(b)

Figure 4.2: Simple shear tests with different initial void ratios:(a) shear strain vs shear stress, (b) mean principal stress vs shear stress.

4.3.2 Granular sheared in an annular shear cell

In this section, the experiments by Savage and Sayed [74] with a cohesionless dry granular material sheared in an annular shear cell are modelled by the SPH method. The experiments aim to investigate the stress developed in rapid shearing dry granular material with a constant volume. As stated in Section 3.4, the initial normal stress ranges from 100 to 1500 Pa due to gravity; $p_0 = 500$ Pa is chosen as the initial confining pressure in the numerical simulations; the first group of experiments in [74], No. PS18 $\sim$ PS21 with small polystyrene beads, are simulated by the SPH method. The physical properties of the beads are: particle density $\rho_s = 1095$ kg/m^3, diameter $d = 1.0$ mm. According to the geometry of the experimental apparatus, the experiments can be modelled as an infinite simple shear test with fixed volume. Therefore, the computational setup displayed in Figure 4.1 is employed again. The material parameters for the hypoplastic portion used in the numerical modelling is same with that in Table 3.3. The angle α_i which correspond to the stress ratio in fast shearing stage is assumed equal to a constant of 27° for all the specimens. Following the experiments, four simulations with different solid volume fraction (hence different void ratio) are performed. The solid volume fraction, the corresponding void ratio and K_2 are given in Table 4.1.

In the numerical simulations a velocity field of $v_x = 2\kappa z$ m/s and $v_z = 0$ m/s is imposed, where κ is the desired shear rate. In this work the range of shear rate κ is 10 $\sim$ 500. At the beginning the model is given a shear rate of $\kappa = 10$ for 0.5 s, to make sure that the granular flow fully develops and the critical state is reached. Then κ is linearly increased to 500 in 20 seconds. Due to the extremely large shear strain, any stress part from the hypoplastic model is the residual stress after critical state being reached.

Table 4.1: List of solid volume fraction C, void ratio e, residual stresses and viscous coefficient K_2 in the four simulations.

Solid volume fraction, C [-]	0.461	0.483	0.504	0.524
Void ratio, e [-]	1.169	1.070	0.984	0.908
T_{xz} [Pa]	0.0	0.0	0.0	36.5
T_{zz} [Pa]	0.0	0.0	0.0	83.2
K_2 [kg/m]	0.0022	0.0033	0.0050	0.0080

The residual stress from simulations with different solid volume fraction after the first 0.5 second of shearing are listed in Table 4.1, presenting almost the same values of the analytical results as shown in Table 3.5. Full liquefaction (or gasification since the interstitial fluid is air) for the specimens with $C = 0.461$, $C = 0.483$ and $C = 0.504$ are well captured in the numerical simulations. For the dense case $C = 0.524$, a non-zero residual stress is obtained regardless of the magnitude of shear strain. According to the equation (2.38), the coefficient K_2 for the four simulations is calculated and listed in Table 4.1. Since ρ_s and d are constants for a given granular material, the solid volume fraction (void ratio) is significant to the granular flowing property as it has great influence on K_2.

The shear and normal stresses developed in rapid shearing are shown in Figure 4.3 and 4.4. By

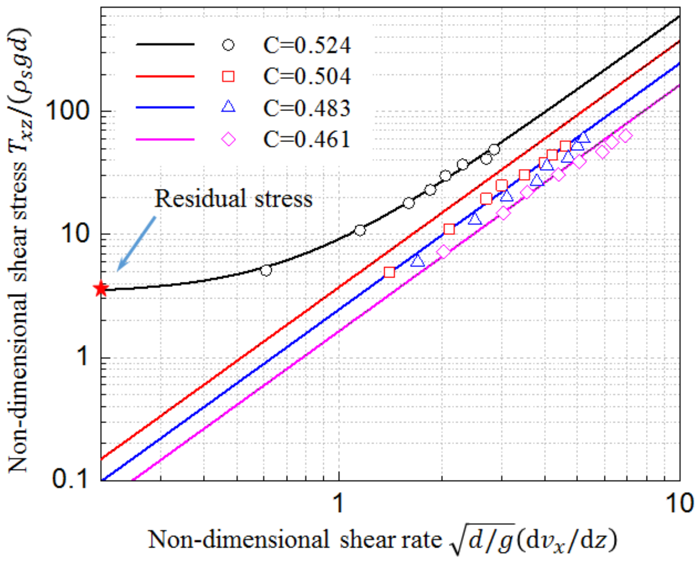

Figure 4.3: Dry granular flow with different solid volume fraction: shear rate vs. shear stress. The markers denote experimental data from [74].

comparing with the analytical results in Section 3.4, it can be seen that the evolution of stress from the quasi-static state to rapid shear flow is correctly modelled by the SPH method.

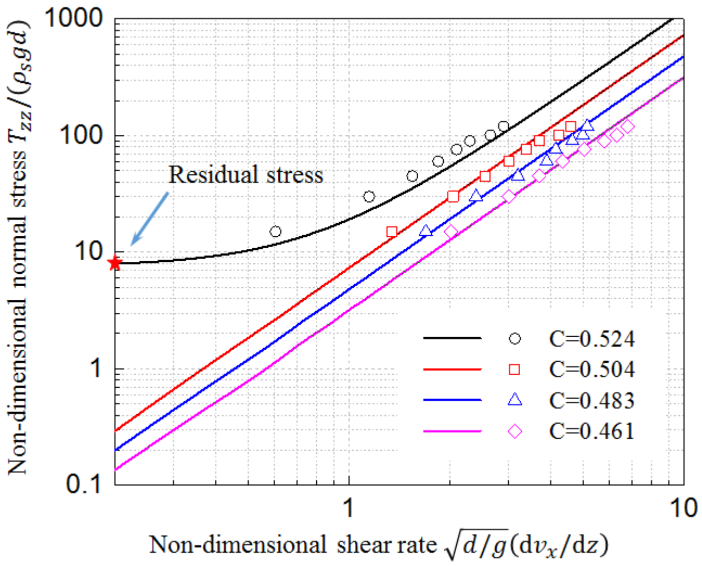

Figure 4.4: Dry granular flow with different solid volume fraction: shear rate vs. normal stress. The markers denote experimental data from [74].

4.4 Application to boundary value problems

Two element tests are performed in Section 4.3, where the velocity fields are prescribed to reproduce uniform deformation conditions. The tests give preliminary validation of our unified approach. In this section, the proposed unified model and the SPH method are applied to real granular flow problems.

4.4.1 Granular flow on an incline

The problem of a granular mass on an incline is considered, as shown in Figure 4.5. The inclination is θ, the granular mass has a free surface and is subjected to gravity. The total height of the granular is H. In this section, the characteristics of granular flows with different inclinations are studied.

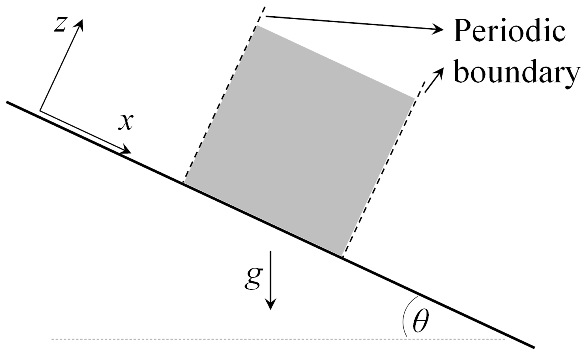

Figure 4.5: Sketch-up of a granular flow on an inclined plate.

Analysis based on the unified model

For a static granular mass or a steady flow, the stress components at arbitrary height z should be hydrostatic

$$T_{zz} = \rho g(H - z)\cos\theta, \;\; T_{xz} = \rho g(H - z)\sin\theta \tag{4.31}$$

where ρ is the bulk density. Now we proceed to calculate the actual shear stress provided by the frictional contact in the plane parallel to the incline. The failure criterion in the hypoplastic model Eq. (3.16) is of the rounded Mohr-Coulomb type. Therefore, the failure of the material approximately follows the Mohr-Coulomb friction law. For an infinite steady granular flow on the incline, we assume that the failure slip lines are parallel to the plane. Therefore, the maximum shear stress provided by the hypoplastic model can be estimated as $T^h_{xz} = T^h_{zz}\tan\phi$, where ϕ is the internal friction angle at failure, termed as residual fiction angle or critical friction angle. For the static state, the dynamic stress part can be neglected. Therefore, the balance in the z direction requires $T_{zz} = T^h_{zz} = \rho g(H - z)\cos\theta$. As a result, the condition for static state is $T_{xz} = T^h_{xz} \geq \rho g(H - z)\sin\theta$, which means $\theta \leq \phi$.

When $\theta > \phi$, the granular starts to flow, generating a dynamic stress part. Under steady flow condition, by examining the force balance we have

$$T_{zz} = \rho g(H - z)\cos\theta = T^h_{zz} + T^v_{zz}, \;\; T^v_{zz} = 4k_v\dot{\varepsilon}^2_{xz}/\tan\alpha_i, \;\; T^h_{zz} = T_{zz} - T^v_{zz} \tag{4.32}$$

$$T_{xz} = \rho g(H - z)\sin\theta = T^h_{xz} + T^v_{xz} = T^h_{zz}\tan\phi + 4k_v\dot{\varepsilon}^2_{xz} \tag{4.33}$$

In the steady granular flow, the stress consists of the contributions from a frictional contact part and a collision part, described by the hypoplastic model and the Bagnold-type rheology, respectively. Owing to the steady flow assumption, the strain rate tensor has only one non-zero component $\dot{\varepsilon}_{xz} = 0.5\partial v_x/\partial z$.

Based on Eq. (4.32) and (4.33), we obtain the velocity profile by solving a differential equation

$$A\left(\frac{\partial v_x}{\partial z}\right)^2 - B(H-z) = 0, \;\; A = (1-\tan\phi/\tan\alpha_i)k_v, \;\; B = \rho g(\sin\theta - \cos\theta\tan\phi) \tag{4.34}$$

Solving the above equation, we have the velocity profile

$$v_x(z) = \frac{2}{3}\sqrt{B/A}(H^{3/2} - (H - z)^{3/2}) \tag{4.35}$$

and its derivative

$$\frac{\partial v_x}{\partial z} = \sqrt{B/A}(H - z)^{1/2} \tag{4.36}$$

The velocity profile, evolving as $(H - z)^{3/2}$, corresponds to a Bagnold profile [16]. Once the velocity profile is obtained, the hypoplastic and dynamic stress parts can be calculated from Eq. (4.32) and (4.33). The Eq. (4.35) and (4.36) show that the velocity and shear rate increase with the inclination θ. Therefore, with increasing θ, the normal and shear stresses caused by collision become more significant. The increase in normal stress gives rise to dilation, tending to reduce the possibility of frictional contact thus resulting in a decrease in the frictional (hypoplastic) stress part.

If we define a phenomenological frictional coefficient $\mu = T_{xz}/T_{zz}$, in steady shearing flow we can observe that the coefficient μ increases with θ because the force balance requires that $\mu = \tan\theta$. This increase of the phenomenological frictional coefficient is found in many tests, as well as described by the $\mu(I)$ model by Jop et al [45]. According to classical explanations, this increase is the result of granular dilation [2]. In the present work this dilation can be properly described by the combination of the hypoplastic model and Bagnold-type rheology. As stated in Section 2.2, the maximum inclination for a steady shearing flow is equal to the angle α_i, i.e.

$$\phi \leq \theta \leq \alpha_i \tag{4.37}$$

Only in this range steady dense granular flows can be observed. When $\theta > \alpha_i$, frictional (hypoplastic) stress part disappears. The shear stress provided by granular collisions is insufficient to balance the driving force, so the granular accelerates continuously and reaches a gasified state. It is noteworthy that the obtained results are quite similar to that from the $\mu(I)$ model [16], where the coefficients μ_s and μ_l corresponds to $\tan\phi$ and $\tan\alpha_i$, respectively.

One important assumption in the above analysis is $T^h_{xz}/T^h_{zz} = \tan\phi$ at failure and subsequent flow state. When describing granular flows in the framework of depth-averaged equations, Savage and Hutter employ the same assumption [72]. However, some discrete simulations suggest that $T^h_{xz}/T^h_{zz} = \sin\phi$ [3, 21], indicating a different failure slip line. Besides, the actual failure surface of the hypoplastic model is slightly different from that of Mohr-Coulomb model, which may result to minor violation of the frictional law. Nevertheless, the above analysis is valid in principal, though the exact ratio between T^h_{xz} and T^h_{zz} may be subject to further discussion. Considering separately the friction and collision in granular flow gives rise to interesting findings.

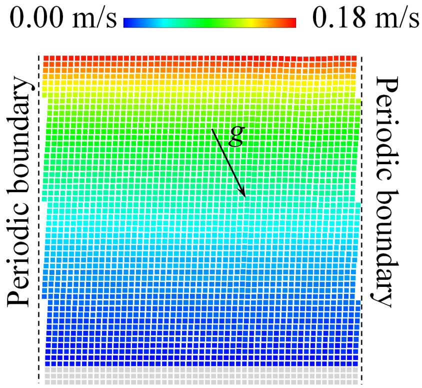

Figure 4.6: Numerical setups for the simulation of steady granular flow. The color scale represents the velocity field in $\theta = 26°$.

Numerical modelling

The numerical setups for the simulation of the steady granular flow is shown in Figure 4.6. The height of the granular is $H = 0.03$ m. A square granular body is modelled with periodic boundary condition. The material constitutive parameters are given in Table 4.2. The hypoplastic parameters $c_1 \sim c_4$ correspond to an internal friction angle $\phi_0 = 25°$. The critical state parameters and initial void ratio are chosen such that the residual friction angle $\phi = \phi_0$, i.e. no softening or hardening occurs at the critical state. Other physical constants are: granular diameter $d = 1.1$ mm, particle density $\rho_s = 1095$ kg/m^3. Three simulations with varied slope angle $\theta = 26.0°$, $27.5°$ and $30.0°$, are performed. These angles lie in the range of $\phi < \theta < \alpha_i$, steady granular flows are therefore expected (see Section 4.4.1). All particles are at rest at the beginning of simulation. As $\theta > \phi$, the shear force provided by particle friction cannot balance the driving force. The granular starts to flow while the dynamic stress part begins to develop. The two stress parts evolve simultaneously and adjust continuously according to the flowing state, loading conditions and boundary conditions. Eventually the flow reaches a steady shearing state.

Table 4.2: Material parameters for the granular on a inclined plate.

c_1	c_2	c_3	c_4	$e_{\min}$	p_1	p_2	p_3	q_1	q_2	q_3	K_2	α_i
[-]	[-]	[-]	[-]	[-]	[-]	[-]	$[kPa^{-1}]$	[-]	[-]	$[kPa^{-1}]$	[-]	[°]
-66.7	-832.9	-832.9	1594.5	0.597	0.53	0.45	-0.0011	1.0	-0.4	-0.0001	0.1	33.0

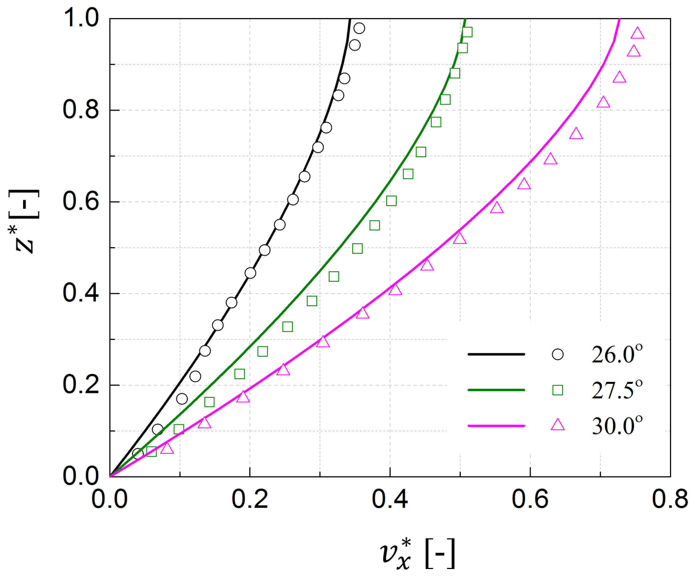

Figure 4.7: Velocity profiles: lines indicate reference solutions calculated from Eq. (4.35) and markers are numerical results.

To compare flows with different inclinations, the following dimensionless variables are used in the analysis: $z^* = z/H$; $v_x^* = (v_x/\sqrt{gH})(d/H)$; $T^* = T/(\rho g H)$. Steady granular flows are observed in all the tested inclinations in numerical simulation. The velocity profiles are given in Figure 4.7. The analytical solutions in Section 4.4.1 are used as the reference. The velocity changes in height show clearly Bagnold profile. For all three inclinations, the numerical results are in good agreement with the analytical solutions. Figure 4.8 and 4.9 give the frictional contact (hypoplastic) and collisional stresses, respectively. A systematic agreement between

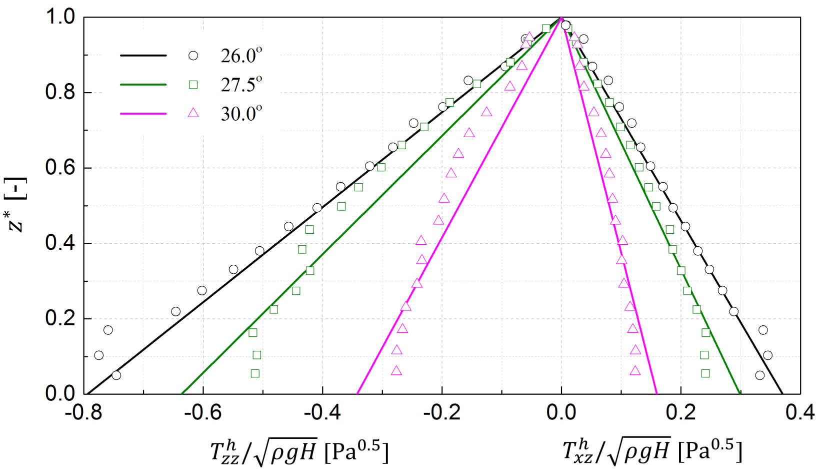

Figure 4.8: Normalized analytical and numerical frictional contact (hypoplastic) stress. Normal stress is in the left (negative part) and shear stress in the right (positive part).

the analytical and numerical results is observed. The discrepancy is pronounced close to the bottom, particularly on the profiles of frictional contact stress. It can be found that as the inclination increases, the frictional contact becomes less significant, and collisional stress turns into the dominant one. The two stress parts evolve simultaneously, automatically balancing the external loading. The presented results can be regarded as a validation of the numerical implementation of the unified model within the SPH method.

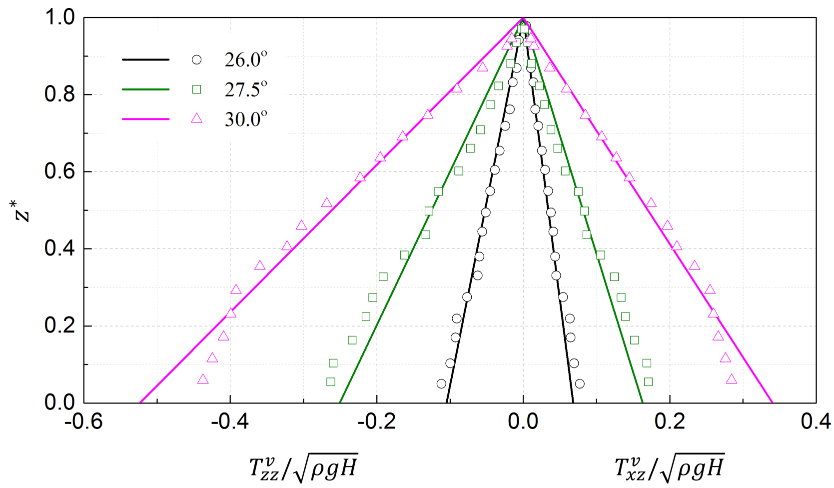

Figure 4.9: Normalized analytical and numerical collisional stress. Normal stress is in the left (negative part) and shear stress in the right (positive part).

4.4.2 Collapse of a granular pile

The collapse of a granular pile on a flat surface is studied in this section. This problem has well defined initial and boundary conditions and has been studied experimentally and numerically [58, 14, 66]. Previous numerical simulations often apply rate-independent constitutive models, thus do not consider the dynamic effect in granular flows.

The simulation is performed under plain strain condition. The initial geometry and boundary conditions are shown in Figure 4.10. A pile of granular material with 10 cm height and 20 cm width is initially under static state. Similar to a dam-break problem in fluid dynamics, after suddenly releasing the confining gate, the granular pile starts to collapse. The material properties are the same as those used in the Section 4.4.1 except $c_1 \sim c_4$. The parameters $c_1 \sim c_4$ are taken as $c_1 = -50$, $c_2 = -832.1$, $c_3 = -832.1$ and $c_4 = 2369.9$, which correspond to a friction angle of $22°$. The initial particle spacing is taken as 0.002 m, giving rise to approximately 5000 particles.

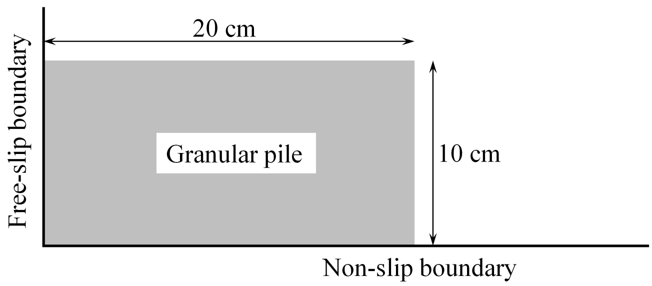

Figure 4.10: Initial geometry and boundary conditions.

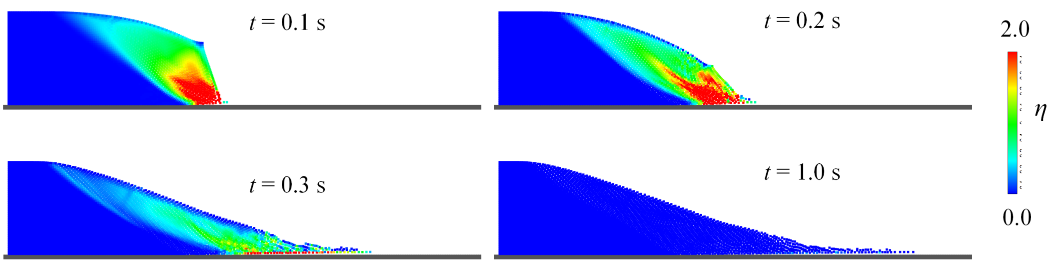

Figure 4.11: The collapse process of the granular pile. The figures are coloured by equivalent viscosity η.

As pointed out in Section 1.1, a granular flow can be treated as a viscous fluid with an equivalent viscosity which depends on the shear rate. From Eq. (4.1), the equivalent viscosity can be defined as $\eta = 2K_2\sqrt{|\,II_D\,|}$. The equivalent viscosity is not only dependent on material properties, but also on the granular kinematics. It is related to both viscous shear stress and dispersive pressure. In quasi-static region, the equivalent viscosity is negligibly small, thus it can be used to distinguish the solid-like and fluid-like regions. Figure 4.11 shows the process of the collapse together with the evolution of the equivalent viscosity η. The flowing area propagates from right to left. There exists a slip plane above which the particle moves and below which particles are generally at rest. The equivalent viscosity helps us easily identify the flowing state. In the flow regions, significant parts of stress components are developed by particle collisions. To demonstrate the evolution of dynamic stress in the collapse, in Figure 4.12, we show the percentage of the dynamic part of stress in the total vertical stress component $(T^v_{zz}/(T^v_{zz} + T^h_{zz}) \times 100\%)$ at three different particles throughout the simulation. From the initial locations of the three particles, we can see particle A and B are in the potential flow area with A closer to the surface, particle C is deep inside the granular body, subjected to less deformation in the collapse. In the collapse, dynamic stresses at particle A and B are significant, indicating partial fluid-like behaviors. For a short period, the dynamic stress accounts for the whole stress (percentage reaches 100%), which means the granular material behaves like a pure Bagnold-type fluid. With collapse coming to its end, the significance of dynamic part reduces, the granular material behaves more and more like solid. Once granular mass finally reaches static packing, the dynamic stress part disappears and stress components are all developed by frictional contacts. Comparison between particles A and B shows that dynamic stress is usually larger at particle A, indicating particles near the right surface are more fluid-like in the collapse. At particle C deep in the granular body, the dynamic stress components are very close to zero. The material is solid-like and does not undergo fluid-like flow.

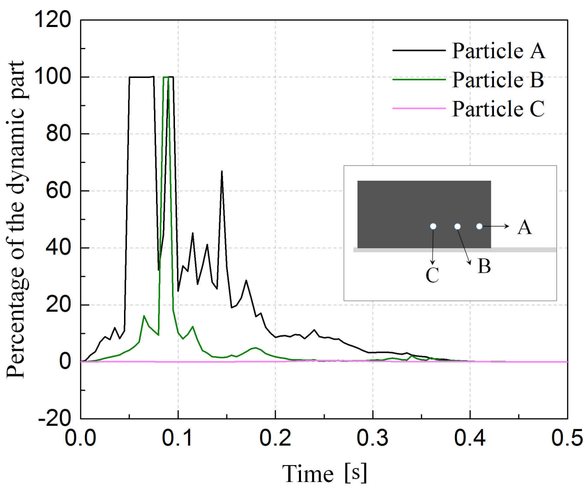

Figure 4.12: Change in percentage of dynamic stress part in the total stress at three particles.

The proposed unified model differs substantially from Bingham model or pure Bagnold-type model. It can account for the rate-independent solid state accurately with its hypoplastic component. Material behaviors inside the yield surface are well-defined. In simulations with the Bingham model or pure Bagnold-type models, materials will never reach the final static state, creeping is usually observed. However, in simulations with the unified model, material can reach the final static state because the final solid-state is described with the hypoplastic model. Figure 4.13 gives the evolution of runout distance in time. It is observed that the granular pile reaches the final state in about 0.5 second. From then on the granular material is at rest, and no creep is observed.

It is well-known that SPH suffers the so-called short-length-scale-noise, which leads to stress fluctuations in areas with large deformation [63]. Several methods are proposed to mitigate this deficiency, e.g. artificial viscosity and stress regularisation. In this thesis only artificial viscosity is used. The stress results at the final state are shown in Figure 4.14. In areas without particle rearrangement, very smooth stress distributions are obtained. However, in regions with large deformation, stress oscillations are observed. Fortunately, it is reported that the kinematics obtained through SPH are generally satisfactory even with stress oscillation [63]. This finding is also confirmed by our simulations. Nevertheless, the stress accuracy is a challenge for SPH and is subject of further study.

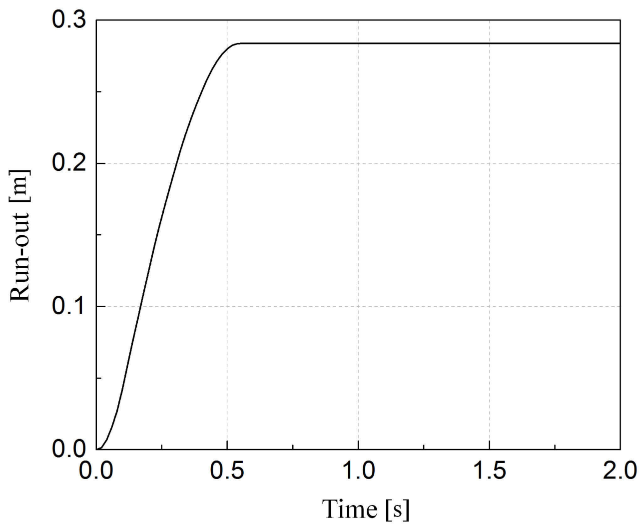

Figure 4.13: Evolution of runout distance.

4.4.3 Granular flow in a rotating drum

A granular mass rotating in a drum is modelled in this section. The material properties are the same as those used in Section 4.4.1. The numerical setup is shown in Figure 4.15. The

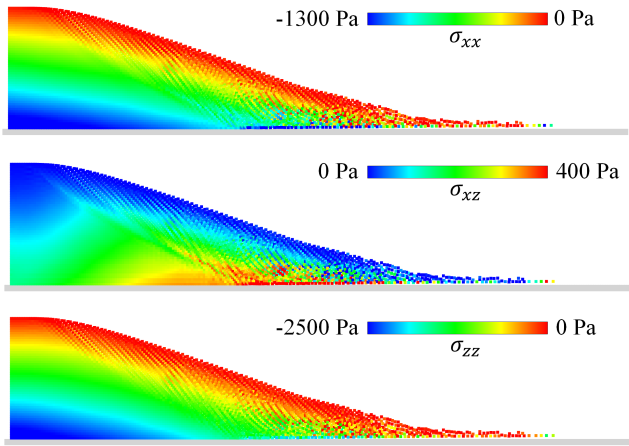

Figure 4.14: Stress distributions in the final state.

granular flows in the rotating drums are surface flows over the static grains. The granular quasi-static and dynamic flowing states coexist in this configuration. The flows in rotating drums are inhomogeneous in flow depth and inclination. Therefore, analytical solutions are usually unavailable.

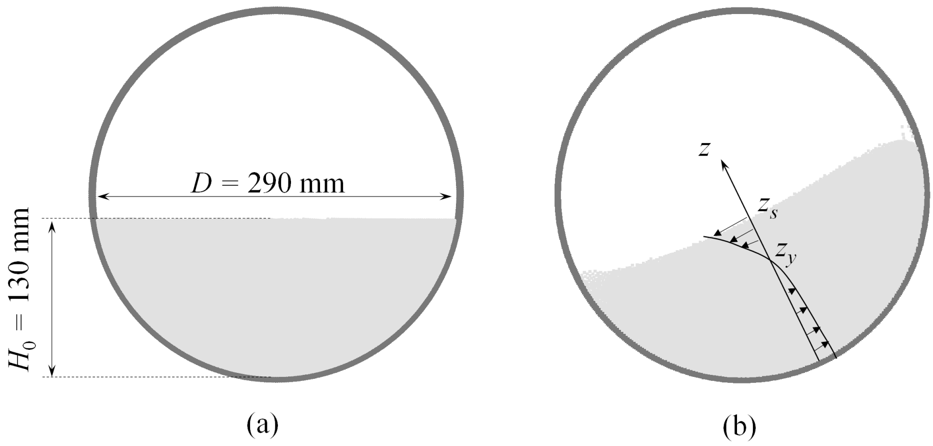

Figure 4.15: Numerical setups for the simulation of granular in a rotating drum: (a) initial state; (b) steady flow state.

Three simulations with different angular velocities $\omega = 0.5$, 1.0 and 2.0 s^{-1} are performed. The rotating process of $\omega = 1.0$ s^{-1} is shown in Figure 4.16. At first the granular mass moves with the drum like a solid block without any deformation. As the surface slope angle grows, failure occurs in the granular body. As a consequence, shear band develops, and the first avalanche takes place. This first avalanche is followed by several small avalanches, and eventually a steady surface granular flow is observed. Below the surface flow the granular remains quasi-static and moves with the drum as a solid block. This process is further confirmed by the

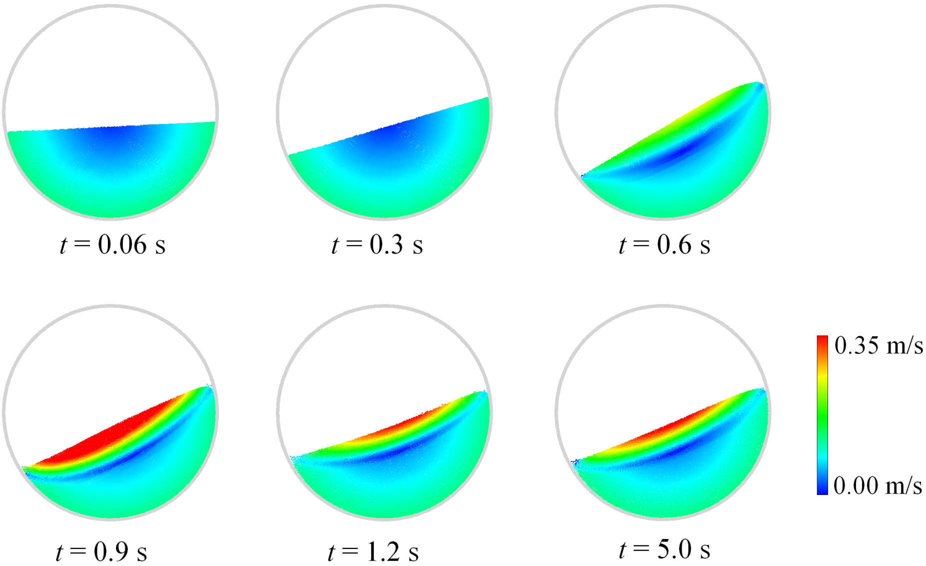

Figure 4.16: The developing process of steady surface flow in the rotating drum, $\omega = 1.0\ \mathrm{s}^{-1}$.

evolution of the maximum surface speed, as shown in Figure 4.17. The velocity evolutions under different rotating angular speeds are similar. The peaks in Figure 4.17 mark the first avalanche. As expected, the appearance of this critical event is delayed with the decrease of the rotating velocity of the drum. In each simulation, a steady flow state is achieved after several seconds of rotating.

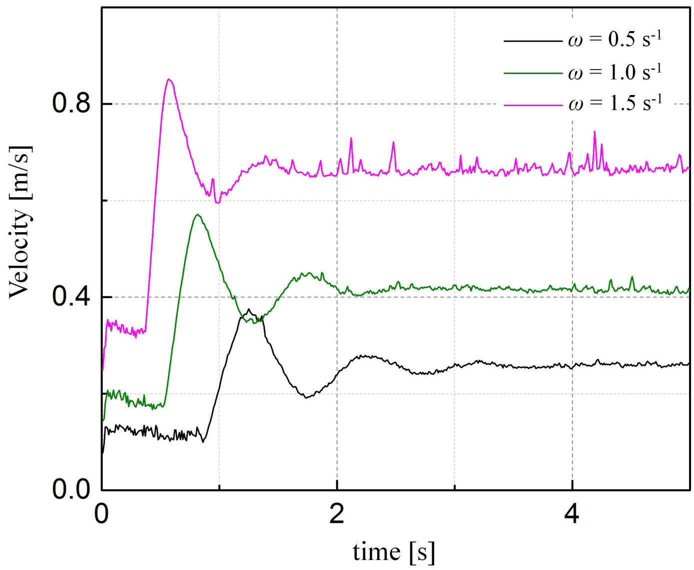

Figure 4.17: Evolution of maximum surface velocity.

A local coordinate as shown in Figure 4.15(b) is used, and the flow characteristics along direction z are studied. z_y is the height where flow state changes and z_s is the height of the flow surface; $h = z_s - z_y$ is the flow depth. In the range of $z < z_y$ the granular mass behaves solid-like, so the velocity profile is linear. The steady velocity profiles in the dynamic flowing layer are given in Figure 4.18. On a middle cross-section, the velocity direction pointing down the slope is defined as positive. The velocity profiles for different rotating speeds are similar in shape but with different magnitudes. In experiments [26], similar velocity profiles are observed. The simulated flow rates, flow depths and average inclinations are summarised in Table 4.3. In our flow configuration, the flow rate is calculated by $Q = 0.5\omega[R^2 - (R - H_0)^2]$, where $R = D/2$ is the drum radius. It is found that the flow depth h and average inclination θ changes almost linearly with respect to the flow rate Q. This observation is also well collaborated with the experimental results [26].

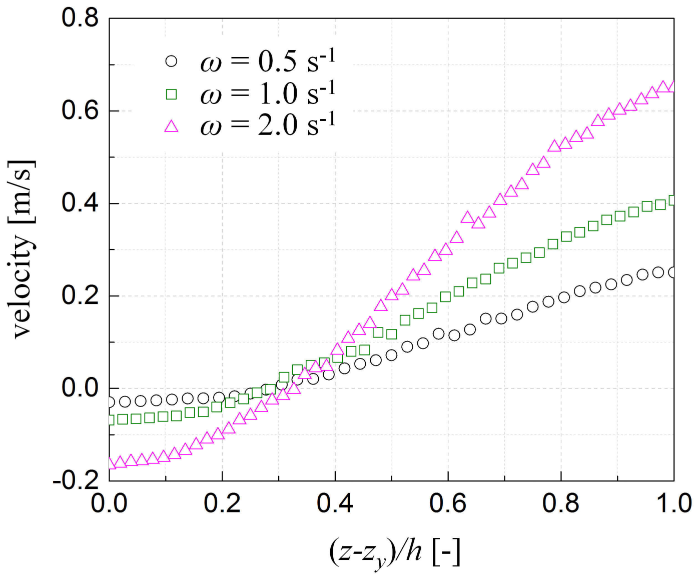

Figure 4.18: Velocity profiles in the flowing layer.

Table 4.3: Summary of the numerical modelling of rotating drum.

Rotating speed ω (s^{-1})	0.5	1.0	2.0
Flow rate Q (m^2/s)	0.0052	0.0104	0.0208
Flowing depth h (m)	0.046	0.054	0.065
Average inclination θ (°)	21.48	22.43	24.81

In the drum the surface flow moves over the solid-like granular body, so that both static and flow states coexist in the computational domain. In the simulations the dynamic part is always taken into account. However in the quasi-static zone the calculated collisional stress is negligible that the dynamic part has no realistic effect on the mechanical response of the material.

In the beginning, there is no flow and the granular behaves like solid. Phenomena observed in solids, such as non-isotropic stress tensor and shear band, are reproduced in the simulations. As shown in Figure 4.19, in the steady flow state the flowing zone, where dynamic stress part takes effect, can be marked by an apparent viscosity $\eta = 2K_2\sqrt{\mid II_D \mid}$. In the blue zones the apparent viscosity is almost zero. Therefore, the dynamic part of the constitutive model has no realistic effect. As a result, only the solid-like behaviors are described by the hypoplastic model. From the simulations, we can see that the solid-like and flow behaviors of granular material are successfully modelled by the unified constitutive model. The explicit determination of the solid/flow states is unnecessary. The solid/fluid transition is achieved naturally in the computation. We do not make use of concepts such as yield stress or flow initiation criterion. Therefore, the numerical implementation is greatly simplified.

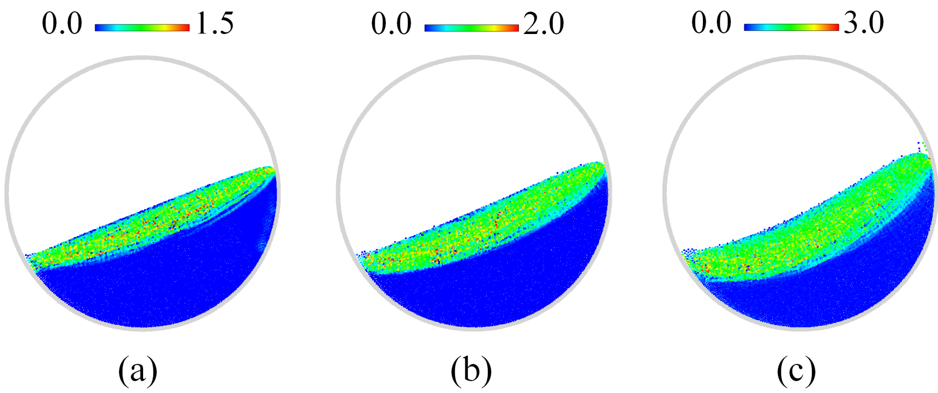

Figure 4.19: Quasi-static and flowing regions in the drum: (a) $\omega = 0.5\ \mathrm{s}^{-1}$; (b) $\omega = 1.0\ \mathrm{s}^{-1}$; (c) $\omega = 2.0\ \mathrm{s}^{-1}$. The figures are coloured by the apparent viscosity η.

Chapter 5

Conclusions and outlook

5.1 Conclusion

In Bagnold's pioneering work [5], a gravity-free dispersion of solid spheres is sheared in Newtonian liquids, where the solid particles with same density of the liquids are used. The stresses in the 'macro-viscous' regime where the effect of fluid viscosity is the dominant mechanism show linear dependence on the shear rate. The stresses in fast flow stage which termed 'grain-inertia' region present quadratic dependence on the shear rate. In this stage, the bulk behavior and dissipation of the flow kinetic energy are dominated by the inelastic and frictional particle collisions. In both regimes, the ratios between shear and normal stresses are almost constants. However, no constitutive relation is available for the transition region between the 'macro-viscous' and 'grain-inertia' regimes. By fitting the experimental data in [5], the addition of the shear stresses in the viscous case and inertia case, equation (2.7), is found to be a competent model to describe the shear stress in the entire flow stage, including the stress in the transition region. Since two constant stress ratios is observed in the experiments, the combined model is also obtained for the normal stress as equation (2.8). As stated before, the density of solid particles is equal to that of the interstitial fluids in Bagnold's experiments, which is similar to the state of full liquefaction. It is an imaginative arrangement which highlights the effect of the fluid viscosity and particle collisions, eliminates the effect of gravity and further facilitates the analysis of the experimental data. However, this setting eliminates the yield stress in the experiments. It means no yield stress was considered in Bagnold's models since they are developed based on the experimental data. For a general case where the gravity is not eliminated by the pore fluid pressure completely, the stresses due to prolonged contact before yielding should be taken into account in a complete model which can describe the stress state throughout the shear process from quasi-static state to high-speed shearing stage. The stresses in the quasi-static state, T_0 and P_0, are considered to meet Mohr-Coulomb criterion. By adding T_0

and P_0 to equation (2.7) and (2.8) respectively, the framework for constitutive modelling of granular-fluid flows is obtained as (2.10). T_0 and P_0 are termed the static portion while T_r and P_r are the dynamic portion. For dry granular flow on an inclined plane, the framework can predict the experimental observation that the steady state flow is obtained over a slope range. A concrete simple-shearing model for grain-fluid flows is developed within this framework. The critical solid volume fraction for a full shearing to occur is taken into account in the dynamic portion. The existence of the stagnant zone is considered to be the main reason for the dramatic increasing of dynamic viscosity when the solid volume fraction is greater than the critical value. Inspired by a common structure of some former models, the simple-shearing model is extended to a three-dimensional form as (2.47). The new model was used in the element tests to simulate the stress-strain relationship of two annular shear tests with dry granular material and granular-water mixture. The predicted stress-shear rate curves in both tests show well agreement with the experimental data in the high shear rate stage. However, when the residual normal stress in the beginning of the flow is determined as the gravity component of the solid phase which is perpendicular to the flow plane, the total shear and normal stresses in the low speed stage is overestimated by the model (2.47). Actually, the residual normal stress doesn't equal to the gravity component in the cases of saturated granular materials with undrained boundary condition or dry granular materials with constant volume. Shear softening is normally observed in these cases where the normal stress in the quasi-static stage will decrease from the gravity component of the solid phase to a residual value. Therefore, more sophisticated theory is required for the static portion of (2.47) to capture this process in the initiation of a granular-fluid flow.

Debris flow is normally simplified as granular-fluid flow in constitutive modelling. The increasing of excess pore water pressure which corresponds to the former mentioned process of shear softening is considered as the most significant triggering factor in the initiation of debris flows. Therefore, a constitutive model for debris materials should be capable to capture the shear softening before flow and to determine the residual strength exactly. The applicability of a hypoplastic model in describing the solid-like behaviors of debris materials is studied by simulating the undrained simple shear tests of saturated granular material. Undrained simple shear test is believed to be particularly relevant to the initiation mechanism of debris flows. Three types of stress-strain behavior in which the 'liquefaction' is regarded as the main cause of debris flow mobilization are reproduced by the hypoplastic model. It is shown that the hypoplastic model has the capability to describe the tendency of volume deformation and further capture the phenomenons of shear softening and hardening of granular-fluid mixtures. Therefore, it is chosen as the static portion of the new model for debris flows. On the other hand, the fluid-like behavior of debris materials in the flowing stage is related to some material parameters, such as solid volume fraction, fluid viscosity and particle density which have be taken into account in the dynamic portion of the model (2.47). The hypoplastic model is combined with the dynamic portion of the model (2.47) to obtain a new complete model for debris materials as equation (3.24). Thus, statics and dynamics are unified in the new model. No explicit critical point between the solid and fluid state is determined by the unified model which covers the whole spectrum of granular state from quasi-static motion to rapid granular flow. The conversion of motion state is achieved by the coupled evolution of the frictional contact and collision stress parts and finished automatically. The new model is employed to simulate the same annular shear tests used in Chapter 2 for comparison. In the case of dry granular flow with constant volume, the residual stresses of the specimens with different compactness are predicted by the hypoplastic portion, which indicate partial and full liquefaction. Based on the accurate prediction of the residual stresses, the overestimation of the total shear and normal stresses in the low speed stage is eliminated and all the predicted stress-strain curves agree well with the experimental data. The non-quadratic dependence of the stresses on the shear rate in the experimental data of the relatively dense specimen is captured by the new model. Similar conclusions are obtained in the simulation of water-saturated granular flow. Comparing to the dry granular flow, the linear terms T_v and P_v, which characterize the effect of the fluid viscosity, are non-negligible in granular-fluid flows. The element test results show that the new model is applicable to model granular-fluid mixtures with different interstitial fluid.

In Chapter 4, the unified model for debris materials is implemented in numerical methods and further verified in the simulations of some boundary value problems. Smoothed particle hydrodynamics (SPH) method which is proved ideal for modelling both solid-like and fluid-like behaviors within a consistent numerical scheme is used for the numerical simulations. The simulation results of two element tests show that the unified approach captures the salient feature of the quasi-static and flowing states of granular materials. In the study of two boundary value problems that dry granular materials flow down an inclined plane and in a rotating drum, the following observations are made: (1) In the case of granular flow down an inclined plane, steady dense granular flow is observed over a range of inclinations, which is consistent with the theoretical analysis in Section 2.2. Moreover, the solutions to this problem in the present model are well collaborated with those from the $\mu(I)$ model [45, 16]. (2) For the granular pile collapse and the granular flow in the rotating drum, the numerical results show wealth of various behaviors, i.e. quasi-static motion, shear band, flow initiation, fully developed granular flow and granular deposition. The implementation of the unified model in SPH is promising to handle the complex behavior of granular flow in a consistent numerical model. It should be noted that all the numerical simulations by SPH in this thesis are focus on dry granular flows. Since some aspects, such as hydro-mechanical coupling and particle segregation, still need further investigation to be considered in the numerical and constitutive model, applying the unified approach to the numerical simulation of debris flow in nature is an interesting challenge in our future work.

5.2 Outlook

As concluded above, a new constitutive model for debris materials is developed by unifying statics and dynamics stresses in a framework. This new model is implemented in SPH and verified by applying to some element tests and boundary value problems. It is demonstrated that the mechanical behavior and motion of granular-fluid flows are well described by the unified model. Based on the work in this thesis, some aspects can be further studied.

The unified model should be used to simulate boundary value problems of granular-fluid flows by fulfilling hydro-mechanical coupling. The simulation results can be compared with that of the $\mu(I_v)$ model developed by Boyer et al. [13].

The dynamic portion of the new model is developed for monodispersed granular materials. It may be extended to more general case that polydispersed particles are contained by using an equivalent particle diameter $\hat{d}$ to replace d in the expression of K_2. Since particle size distribution mainly affects stresses in the 'grain-inertia' regime, the equivalent particle diameter can be determined by the following equation

$$T_i(\hat{d}) = T_i^m \tag{5.1}$$

where T_i^m is the measured shear stress in the high-speed shear stage of multi-size particle-fluid flow with a specific solid volume fraction. Based on a large number of laboratory tests or numerical experiments, the relation between particle size distribution and equivalent particle diameter may be determined.

In this thesis, the hypoplastic model developed by Wu et al. [95] is employed as the static portion of the complete model. As stated before, finding more suitable and concise hypoplastic models for the static portion will be an interesting exploration to refine the new model. On the other hand, developing a complete rate-form model for granular materials within the framework of hypoplasticity is the main target of our future work. Based on the framework (3.25), the developed model may have the capability to distinguish between loading and unloading.

Bibliography

[1] M. P. Allen and D. J. Tildesley. *Mathematics of computation*, chapter Computer simulation of liquids. Oxford University Press, 1987.

[2] J. E. Andrade, Q. S. Chen, P. H. Le, C. F. Avila, and T. M. Evans. On the rheology of dilative granular media: Bridging solid-and fluid-like behavior. *Journal of the Mechanics and Physics of Solids*, 60(6):1122–1136, 2012.

[3] B. Andreotti, Y. Forterre, and O. Pouliquen. *Granular media: between fluid and solid*. Cambridge University Press, 2013.

[4] A. S. Avelar, A. L. C. Netto, W. A. Lacerda, L. B. Becker, and M. B. Mendonça. Mechanisms of the recent catastrophic landslides in the mountainous range of rio de janeiro, brazil. In *Proceedings of the Second World Landslide Forum*, Rome, 2011.

[5] R. A. Bagnold. Experiments on a gravity-free dispersion of large solid spheres in a newtonian fluid under shear. *Proc. R. Soc. Lond. A Math. Phys. Sci.*, 225:49–63, 1954.

[6] R. A. Bagnold. The flow of cohesionless grains in fluids. *Proc. R. Soc. Lond. A*, 249:235–297, 1956.

[7] J. A. Bailard. *An experimental study of granular fluid flow*. Ph.d. thesis, Univ. of Calif., San Diego, 1978.

[8] J. A. Bailard and D. L. Inman. A reexamination of bagnold's granular-fluid model and bed load transport equation. *J. Geophys Res.*, 84:7827–7833, 1979.

[9] E. Bauer. Mechanical behavior of granular materials with special reference to oedometric loading. In *Publication Series of the Institute of Soil Mechanics and Rock Mechanics*. Kaflsruhe University, 1992.

[10] E. Bauer. Calibration of a comprehensive hypoplastic model for granular materials. *Soils and Foundations*, 36(1):13–26, 1996.

[11] E. C. Bingham. *Fluidity and plasticity*. McGraw-Hill, New York, 1922.

[12] J. Bonet and T. Lok. Variational and momentum preservation aspects of Smooth Particle Hydrodynamic formulations. *Computer Methods in applied mechanics and engineering*, 180(1):97–115, 1999.

[13] F. Boyer, É. Guazzelli, and O. Pouliquen. Unifying suspension and granular rheology. *Physical Review Letters*, 107(18):188301, 2011.

[14] H. H. Bui, R. Fukagawa, K. Sako, and S. Ohno. Lagrangian meshfree particles method (SPH) for large deformation and failure flows of geomaterial using elastic–plastic soil constitutive model. *International Journal for Numerical and Analytical Methods in Geomechanics*, 32(12):1537–1570, 2008.

[15] G. Castro. *Liquefaction of Sands*. Ph.d. thesis, Harvard University, Cambridge, Massachusetts, 1969.

[16] G. Chambon, R. Bouvarel, D. Laigle, and M. Naaim. Numerical simulations of granular free-surface flows using Smoothed Particle Hydrodynamics. *Journal of Non-Newtonian Fluid Mechanics*, 166(12):698–712, 2011.

[17] C. S. Chang and P. Y. Hicher. An elasto-plastic model for granular materials with microstructural consideration. *International Journal of Solids and Structures*, 42:4258–4277, 2005.

[18] W. Chen and T. Qiu. Numerical simulations for large deformation of granular materials using Smoothed Particle Hydrodynamics method. *International Journal of Geomechanics*, 12(2):127–135, 2011.

[19] M. D. Coon and R. J. Evans. Incremental constitutive laws and their associated failure criterion with application to plain concrete. *Int. J. Solids Structures*, 8:1169–1183, 1972.

[20] S. C. Cowin. Constitutive relations that imply a generalized mohr-coulomb criterion. *Acta Mech.*, 20:41–46, 1974.

[21] F. da Cruz, S. Emam, M. Prochnow, J. Roux, and F. Chevoir. Rheophysics of dense granular materials: discrete simulation of plane shear flows. *Physical Review E*, 72(2):021309, 2005.

[22] W. Dehnen and H. Aly. Improving convergence in Smoothed Particle Hydrodynamics simulations without pairing instability. *Monthly Notices of the Royal Astronomical Society*, 425(2):1068–1082, 2012.

[23] H. Eyring, D. Henderson, B. J. Stover, and E. M. Eyring. *Statistical Mechanics and Dynamics*. Wiley, 1964.

[24] C. Fang and W. Wu. On the weak turbulent motions of an isothermal dry granular dense flow with incompressible grains: part i. equilibrium turbulent closure models. *Acta Geotechnica*, 9:725–737, 2014.

[25] C. Fang and W. Wu. On the weak turbulent motions of an isothermal dry granular dense flow with incompressible grains: part ii. complete closure models and numerical simulations. *Acta Geotechnica*, 9:739–752, 2014.

[26] MiDi GDR. On dense granular flows. *The European Physical Journal E*, 14(4):341–365, 2004.

[27] R. A. Gingold and J. J. Monagham. Smoothed particle hydrodynamics: theory and application to non-spherical stars. *Manual Notebook of Royal Astronomical Society*, 181:375–389, 1977.

[28] M. Gomez-Gesteira, B. D. Rogers, A. J. C. Crespo, R. A. Dalrymple, M. Narayanaswamy, and J. M. Dominguez. SPHysics–development of a free-surface fluid solver–part 1: Theory and formulations. *Computers & Geosciences*, 48:289–299, 2012.

[29] J. Grabe and E. Heins. Coupled deformation-seepage analysis of dynamic capacity tests on open-ended piles in saturated sand. *Acta Geotechnica*, 2016.

[30] A. E. Green. Hypoelasticity and plasticity i. *Proc. Royal Soc.*, 234:46–59, 1956.

[31] A. E. Green. Hypoelasticity and plasticity ii. *J. Rat. Mech. Anal.*, 5:725–734, 1956.

[32] G. Gudehus. A comprehensive constitutive equation for granular materials. *Soils and Foundations*, 36:1–12, 1996.

[33] X. Guo and W. Wu. Some ideas on constitutive modeling of debris materials. In W. Wu, editor, *Recent advances in modeling landslides and debris flows*, pages 1–9, Vienna, 2015. Springer.

[34] D. M. Hanes and D. L. Inman. Observations of rapidly flowing granular-fluid materials. *Journal of Fluid Mechanics*, 150:357–380, 1985.

[35] R. W. Hockney and J. W. Eastwood. *Computer simulation using particles*. Adam Hilger, Bristol and New York, 1988.

[36] M. L. Hunt, R. Zenit, C. S. Campbell, and C. E. Brennen. Revisiting the 1954 suspension experiments of r. a. bagnold. *Journal of Fluid Mechanics*, 452:1–24, 2002.

[37] K. Hutter, B. Svendsen, and D. Rickenmann. Debris flow modeling: A review. *Continuum Mech. Thermodyn.*, 8:1–35, 1996.

[38] R. M. Iverson. The physics of debris flows. *Reviews of Geophysics*, 35:245–296, 1997.

[39] R. M. Iverson. The debris-flow rheology myth. In *3rd International Conference on Debris-Flow Hazards Mitigation: Mechanics, Prediction, and Assessment*, volume 1, pages 303–314, Davos, 2003.

[40] R. M. Iverson and R. P. Denlinger. Flow of variably fluidized granular masses across three-dimensional terrain 1. coulomb mixture theory. *Journal of Geophysical Research*, 106(B1):537–552, 2001.

[41] R. M. Iverson, M. E. Reid, and R. G. LaHusen. Debris-flow mobilization from landslides. *Annu. Rev. Earth Planet. Sci.*, 25:85–138, 1997.

[42] N. Janbu. Soil compressibility as determined by oedometer and triaxial test. In *Proceedings of the European conference on soil mechanics and foundation engineering*, volume 1, pages 19–25, Wiesbaden, Germany, 1963.

[43] S. T. Jenkins and S. B. Savage. A theory for the rapid flow of identical, smooth, nearly elastic spherical particles. *J. Fluid Mech.*, 130:187–202, 1983.

[44] G. R. Johnson, R. A. Stryk, and S. R. Beissel. SPH for high velocity impact computations. *Comput. Methods Appl. Mech. Eng.*, 139(1):347–373, 1996.

[45] P. Jop, Y. Forterre, and O. Pouliquen. A constitutive law for dense granular flows. *Nature*, 441(7094):727–730, 2006.

[46] G. Klubertanz, L. Laloui, and L. Vulliet. Identification of mechanisms for landslide type initiation of debris flows. *Engineering Geology*, 109:114–123, 2009.

[47] D. Kolymbas. A rate-dependent constitutive equation for soils. *Mechanics Research Communications*, 4(6):367–372, 1977.

[48] D. Kolymbas. A generalized hypoelastic constitutive law. In *Proc. XI Int. Conf. Soil Mechanics and Foundation Engineering, Vol.5, p2626*, 1985.

[49] D. Kolymbas. A novel constitutive law for soils. In Desai, editor, *Proc. 2nd Int. Conf. on Constitutive Laws for Engineering Materials*, pages 319–326, Amsterdam, 1987. Elsevier.

[50] D. Kolymbas. *Introduction to hypoplasticity*. A. A. Balkema, Rorrerdam, 1999.

[51] A. Krawietz. *Stability and plastic yield of hypo-elastic materials*. PhD thesis, Technical University of Berlin, Germany, 1979.

[52] Z. Li, P. Kotronis, S. Escoffier, and C. Tamagnini. A hypoplastic macroelement for single vertical piles in sand subject to three-dimensional loading conditions. *Acta Geotechnica*, 11:373–390, 2016.

[53] L. D. Libersky, A. G. Petschek, T. C. Carney, J. R. Hipp, and F. A. Allahdadi. High strain lagrangian hydrodynamics: a three-dimensional SPH code for dynamic material response. *J. Comput. Phys.*, 109(1):67–75, 1993.

[54] G. R. Liu and Y. T. Gu. *An introduction to meshfree methods and their programming*. Springer, Dordrecht, 2005.

[55] G. R. Liu and M. B. Liu. *Smoothed Particle Hydrodynamics: a meshfree particle method*. World Scientific Publishing Co. Pte. Ltd., 2003.

[56] M. B. Liu and G. R. Liu. Smoothed Particle Hydrodynamics (SPH): an overview and recent developments. *Archives of computational methods in engineering*, 17(1):25–76, 2010.

[57] M. B. Liu, G. R. Liu, Z. Zong, and K. Y. Lam. Computer simulation of high explosive explosion using smoothed particle hydrodynamics methodology. *Comput. Fluids*, 32(3):305–322, 2003.

[58] G Lube, H E Huppert, R S J Sparks, and A Freundt. Collapses of two-dimensional granular columns. *Physical Review E*, 72(4):041301, 2005.

[59] J. J. Major and T. C. Pierson. Debris flow rheology: experimental analysis of fine-grained slurries. *Water Resources Research*, 28(3):841–857, 1992.

[60] D. F. McTigue. *A nonlinear continuum model for flowing granular materials*. Ph.d. thesis, Stanford Univ., Stanford, Calif., 1979.

[61] D. F. Mctigue and S. B. Savage. Comment on a reexamination of bagnolds granular-fluid model and bed load transport equation by j. a. bailard and d. l. inman. *J. Geophys. Res.*, 86:4311–4313, 1981.

[62] S. Nemat-Nasser. A micromechanically-based constitutive model for frictional deformation of granular materials. *Journal of the Mechanics and Physics of Solids*, 48:1541–1563, 2000.

[63] C. T. Nguyen, C. T. Nguyen, H. H. Bui, G. D. Nguyen, and R. Fukagawa. A new sph-based approach to simulation of granular flows using viscous damping and stress regularisation. *Landslides*, pages 1–13, 2016.

[64] A. Niemunis and I. Herle. Hypoplastic model for cohesionless soils with elastic strain range. *Mech. Cohes. Frict. Mater.*, 2:279–299, 1997.

[65] G. Oger, M. Doring, B. Alessandrini, and P. Ferrant. An improved SPH method: Towards higher order convergence. *Journal of Computational Physics*, 225(2):1472–1492, 2007.

[66] C. Peng, W. Wu, H. Yu, and C. Wang. A sph approach for large deformation analysis with hypoplastic constitutive model. *Acta Geotechnica*, 10:703717, 2015.

[67] C. Peng, W. Wu, H. S. Yu, and C. Wang. An improved wall boundary treatment for Smoothed Particle Hydrodynamics with applications in geomechanics. *Journal of Computational Physics*, Under review.

[68] O. Pouliquen and Y. Forterre. Friction law for dense granular flows: application to the motion of a mass down a rough inclined plane. *J. Fluid Mech.*, 453:133–151, 2002.

[69] D. Rickenmann. Empirical relationships for debris flows. *Natural Hazards*, 19:47–77, 1999.

[70] S. B. Savage. Gravity flow of cohesionless granular materials in chutes and channels. *J. Fluid Mech.*, 92:53–96, 1979.

[71] S. B. Savage, M. H. Babaei, and T. Dabros. Modeling gravitational collapse of rectangular granular piles in air and water. *Mech. Res. Commun.*, 56:1–10, 2014.

[72] S. B. Savage and K. Hutter. The motion of a finite mass of granular material down a rough incline. *Journal of fluid mechanics*, 199:177–215, 1989.

[73] S. B. Savage and R. M. Iverson. Surge dynamics coupled to pore-pressure evolution in debris flows. In D. Rickenmann and C-L. Chen, editors, *Debris-flow Hazards Mitigation: Mechanics, Prediction, and Assessment, v. 1*. Millpress, Rotterdam, 2003.

[74] S. B. Savage and M. Sayed. Stresses developed by dry cohesionless granular materials sheared in an annular shear cell. *J. Fluid Mech.*, 142:391–430, 1984.

[75] M. Shibata and C. C. Mei. Slow parallel flows of a water-granular mixture under gravity, part i:continuum modeling. *Acta Mech.*, 63:179–193, 1986.

[76] G.F. Smith. On isotropic functions of symmetric tensors, skew-symmetric tensors and vectors. *International Journal of Engineering Science*, 9(10):899–916, 1971.

[77] H. Stutz, D. Ma$\check{s}\acute{i}$n, and F. Wuttke. Enhancement of a hypoplastic model for granular soilstructure interface behaviour. *Acta Geotechnica*, 2016.

[78] P. Stutz. Comportement $\acute{e}$lasto-plastique des milieux granulaires. In A. Sawczuk, editor, *Foundations of Plasticity*, volume 1, pages 37–49. Noordhoff Int. Pub., 2000.

[79] D. G Thomas. Transport characteristics of suspension: Viii. a note on the viscosity of newtonian suspensions of uniform spherical particles. *J. Colloid Sci.*, 20:267–277, 1965.

[80] T. Y. Thomas. Combined elastic and prandtl-reuss stress-strain relations. *Proc. N. A. S.*, 41(10):720–726, 1955.

[81] T. Tokuoka. Yield conditions and flow rules derived from hypoelasticity. *Arch. Rat. Mech. Anal.*, 42:239–252, 1971.

[82] T. Tokuoka. Rate type plastic material with kinematic hardening. *Acta Mechanica*, 27:145–154, 1977.

[83] T. Tokuoka. Simple shear deformation of rate type plastic materials with combined work-hardening. *Int. J. Engng. Sci.*, 20:791–801, 1982.

[84] C. Truesdell. Hypoelasticity. *J. Rat. Mech. Anal.*, 4:83–133, 1955.

[85] P. von Soos. Properties of soil and rock. In *Grundbau taschenbuch part 4*. Ernst & Sohn, Berlin, 1990.

[86] P. A. von Wolffersdorf. Hypoplastic relation for granular materials with a predefined limit state surface. *Mech. Cohes. Frict. Mater.*, 1(3):251–271, 1996.

[87] C.-C. Wang. A new representation theorem for isotropic functions: An answer to Professor G. F. Smith's criticism of my papers on representations for isotropic functions - Part 1. Scalar-valued isotropic functions. *Archive for Rational Mechanics and Analysis*, 36(3):166–197, 1970.

[88] C.-C. Wang. A new representation theorem for isotropic functions: An answer to Professor G. F. Smith's criticism of my papers on representations for isotropic functions - Part 2. Vector-valued isotropic functions, symmetric tensor-valued isotropic functions, and skew-symmetric tensor-valued isotropic functions. *Archive for Rational Mechanics and Analysis*, 36(3):198–223, 1970.

[89] Y. Wang and K. Hutter. Granular material theories revisited. In N. J. Balmforth and A. Provenzale, editors, *Geomorphological Fluid Mechanics*, chapter I, pages 79–107. Springer, 2001.

[90] H. Wendland. Piecewise polynomial, positive definite and compactly supported radial functions of minimal degree. *Advances in computational Mathematics*, 4(1):389–396, 1995.

[91] G. F. Wieczorek. Effect of rainfall intensity and duration on debris flows in the central santa cruz mountains, california. In J. E. Costa and G. F. Wieczorek, editors, *Debris Flows/Avalanches: Process, Recognition, and Mitigation*. Geol. Soc. of Am., 1987.

[92] W. Wu. On simple critical state model for sand. In *Proc. of the seventh Int. Symp. on Numerical Models in Geomechanics-NUMOG, Graz, Austria, Balkeman, 47-52*, 1999.

[93] W. Wu. On high-order hypoplastic models for granular materials. *Journal of Engineering Mathematics*, 56:23–34, 2006.

[94] W. Wu and E. Bauer. A simple hypoplastic constitutive model for sand. *International Journal for Numerical and Analytical Methods in Geomechanics*, 18:833–862, 1994.

[95] W. Wu, E. Bauer, and D. Kolymbas. Hypoplastic constitutive model with critical state for granular materials. *Mechanics of Materials*, 23:45–69, 1996.

[96] W. Wu and D. Kolymbas. Numerical testing of the stability criterion for hypoplastic constitutive equations. *Mechanics of Materials*, 9(3):245–253, 1990.

[97] W. Wu and D. Kolymbas. Hypoplastic then and now. In D. Kolymbas, editor, *Constitutive Modelling of Granular Material*, pages 57–105. Springer, 2000.

[98] W. Wu and A. Niemunis. Beyond failure in granular materials. *Int. J. Numer. Anal. Methods Geomech.*, 21:153–174, 1997.

[99] F. L. Yang and M. L. Hunt. Dynamics of particle-particle collisions in a viscous liquid. *Phys. Fluids*, 18:121506, 2006.

[100] M. Yoshimine and K. Ishihara. Flow potential of sand during liquefaction. *Soils and Foundations*, 38:189–198, 1998.

[101] M. Yoshimine, K. Ishihara, and W. Vargas. Effects of principal stress direction and intermediate principal stress on undrained shear behavior of sand. *Soils and Foundations*, 38:179–188, 1998.

[102] B. Yu, Y. Yang, Y. Su, W. Huang, and G. Wang. Research on the giant debris flow hazards in zhouqu county, gansu province on august 7, 2010. *Journal of Engineering Geology*, 4:437–444, 2010.

[103] O. C. Zienkiewicz and R. L. Taylor. *The finite element method*. Butterworth-Heinemann, Stonham, 2000.